Electronic and Vibrational Properties of Colloidal Nanocrystals

by

Albert Liu

A dissertation submitted in partial fulfillment
of the requirements for the degree of
Doctor of Philosophy
(Applied Physics)
in The University of Michigan
2020

Doctoral Committee:

Professor Steven T. Cundiff, Chair
Professor Mackillo Kira
Professor Theodore B. Norris
Professor Jennifer P. Ogilvie
Professor Duncan G. Steel

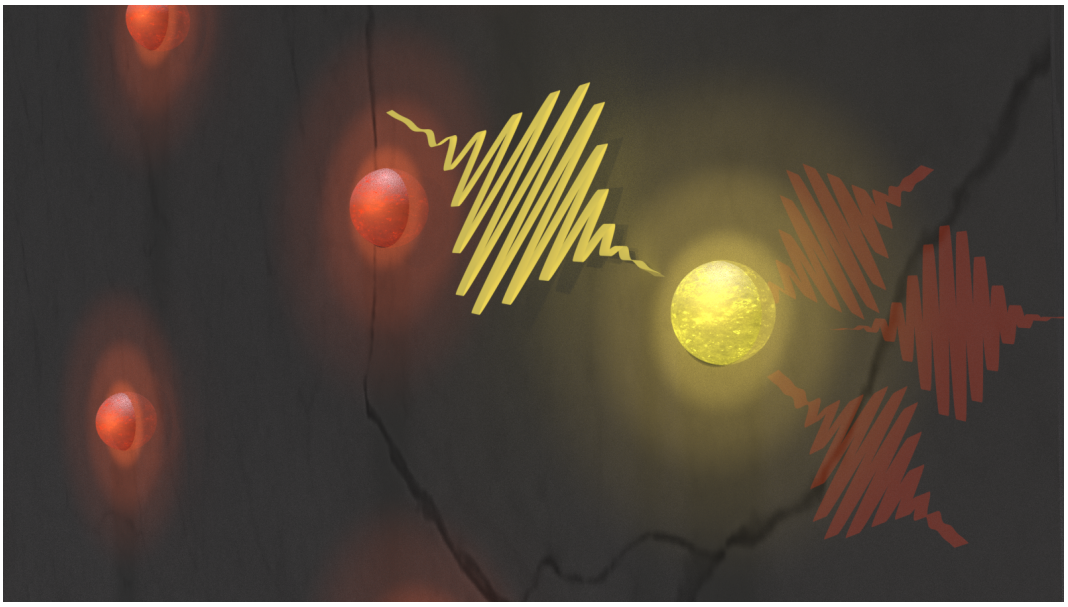

Albert Liu

alberliu@umich.edu

ORCID iD: 0000-0001-6718-3719

ACKNOWLEDGEMENTS

Both I and the work presented in this thesis are a product of my environment. Present and past members of the group have contributed tremendously to my development as an aspiring scientist, and I am deeply grateful for that. As a new student in the lab, I greatly benefited from the vast knowledge of the now-departed members of the group - Rohan, Chris, Takeshi, Kai, and Bacha - which they were more than happy to share. Eric, who remains in the group but is forging his own entrepreneurial path, has been an invaluable source of experimental knowledge and was always available to provide sharp and reasoned feedback for my ideas, no matter how nonsensical they may have been. Among all however, I am most grateful to Diogo, who taught me the ways of the MONSTR and with whom I spent many long nights in lab.

I am also tremendously thankful for the improbable chain of events that led to Steve being my advisor. While I was afforded the freedom to pursue any research directions I found interesting, Steve was always there to steer me away from rabbit holes and dead ends. I've strove to emulate his careful and insightful approach to every problem, with varying degrees of success. I must also thank Duncan, my undergraduate research advisor, for starting me down this path that brings me such joy. He has always been there to guide me, no matter how lost I have been.

Lastly I am thankful to my family. My partner, Janice, has shown unending patience as I spent long nights in lab and supported me throughout my graduate school journey. And nothing I've done or ever will do could be possible without the love and support from Mom, Dad, and my brother Havel.

TABLE OF CONTENTS

LIST OF FIGURES

Figure

LIST OF APPENDICES

Appendix

ABSTRACT

Semiconductors of reduced dimensionality have continued to attract intense interest for both fundamental research and practical applications. Semiconducting colloidal nanocrystals (CNCs) are prime examples of such semiconductors, in which nanometer-scale quantum confinement in all three spatial dimensions gives rise to morphology-, surface-, and composition-tunable opto-electronic properties. CNCs have been implemented in numerous devices such as photovoltaic cells and displays, with many nearing or even having reached commercial maturity. However, rational design of CNC devices and synthesis methodologies continues to be hindered by our limited understanding of their fundamental physics.

This dissertation presents among the first applications of multi-dimensional coherent spectroscopy (MDCS), a third-order nonlinear spectroscopic technique, to CNCs at cryogenic temperatures. MDCS is capable of circumventing inhomogeneous spectral broadening, the main obstacle that has impeded spectroscopic studies of CNCs, and is thus uniquely qualified to study such systems with intricate underlying dynamics obscured by ensemble inhomogeneity.

We first discuss our results on CdSe CNCs, the most mature colloidal material platform, which reveal a strong interplay between electronic dynamics and lattice vibrations (phonons). We directly characterize the spectral density of electronic coupling to low-energy vibrations, which reveals the simultaneous existence of confined and delocalized vibrational modes for the case of nanocrystals embedded in a glass matrix. We also observe the onset of highly non-Markovian dephasing dynamics upon coupling to optical vibrational modes, which may indicate anharmonic coupling or

breakdown of other common approximations.

We also discuss our results on $CsPbI_3$ perovskite nanocrystals, which are an exciting new class of CNCs first synthesized in 2015. We present a systematic study of $CsPbI_3$ nanoplatelets which, despite drastically reduced inhomogeneous broadening, challenges the assertion of homogeneously broadened light-emission at room-temperature. Polarization-resolved multi-dimensional spectra of $CsPbI_3$ nanocubes is performed, which probes quantum pathways traversing their unique non-degenerate triplet exciton fine-structure. We present evidence for a mixed bright-dark level-ordering that renders the triplet states $|\psi_x\rangle$, $|\psi_y\rangle$, and $|\psi_z\rangle$ only partially bright. We also extract crucial figures of merit for quantum information processing, the ensemble-averaged coherence times of both optical triplet coherences ($T_2^x = 5.68$ ps, $T_2^y = 5.32$ ps, $T_2^z = 0.76$ ps) and terahertz inter-triplet coherences ($T_2^{yz} = 1.36$ ps), to position perovskite nanocrystals as a potential material platform for quantum information applications via bottom-up assembly.

CHAPTER I

Introduction

1.1 History of Colloidal Nanocrystals (CNCs)

Nanocrystals have a history that extends even before the tenth century AD. However, it was not until the end of the 20th century that semiconductor nanocrystals began to be systematically synthesized and studied. Specifically, early efforts during the 1980s consisted primarily of two groups in the Soviet Union and United States respectively. In the USSR, Alexei Ekimov began synthesis and characterization of Cu(Cl,Br) and Cd(S,Se) nanocrystals *embedded* in glass matrices [1], with pioneering theoretical studies performed in parallel by Alexei and Alexander Efros [2]. Around the same time at Bell Laboratories in the USA, Louis Brus began reporting the first studies on *colloidal* nanocrystals (CNCs) [3–6].

In the following decade new titans of the field emerged to spur advances at unprecedented speed. Most notably Bawendi's group synthesized CNCs with <5% size dispersion [7] and CNC superlattices [8] while Alivisatos's group was the first to implement CNCs in light-emitting diodes (LEDs) [9] and as biological markers [10]. Meanwhile, Guyot-Sionnest Philippe at the University of Chicago synthesized the first "core-shell" [11] and U-V luminescent [12] CNCs.

1.2 Applications of CNCs

Today, the field of CNC research has grown beyond synthesis and characterization. Their attractive properties, examples of which include their free-standing nature (allowing for straightforward integration onto various surfaces and in matrices) as well as unparalleled size/shape/composition tunability (which change the electro-optical properties of the CNCs themselves), have positioned CNCs as a potential material platform for a broad range of applications. Here we list two of their most well-known uses and direct the reader to recent reviews [13–19] for a more exhaustive discussion of CNCs and the current state of the field.

One of the most striking properties of CNCs is their narrow, tunable emission spectrum that depends on nanocrystal size. It was thus anticipated early on, that CNCs possessed great potential for display technologies. Today the first commercial televisions containing CNCs have been released, albeit without true CNC LED displays. Instead, current "qLED TVs" span the color gamut via blue LEDs placed behind layers of CNCs that down-convert blue light into red and green photoluminescence. Televisions with true quantum dot LED displays have proven feasible in laboratories [20, 21], and are expected to reach consumers within the next decade.

Another prominent application of CNCs that has generated much excitement is their use in photovoltaics. In contrast to bulk semiconductor photovoltaics, in which absorbed high photon energy portions of the solar spectrum are partially converted into thermal waste due to acoustic phonon-assisted intraband transitions, CNCs should experience a "phonon bottleneck" effect due to their discrete energy levels [22]. The longer thermalization times of hot carriers also suggests an increased importance of impact ionization as an alternative channel for their excess energy. Following the first experimental observations of impact ionization in CNCs by Klimov's group in Los Alamos [23], the phenomenon was dubbed "multiple exciton generation" or "carrier multiplication" [24, 25].

Spurred by more than thirty years of research in CNC synthesis, which have resulted in bright and stable nanocrystals exhibiting high size/morphology uniformity, the numerous proposed applications of CNCs are finally beginning to be realized. However, widespread commercialization CNCs will rely on synthesis of heavy-metal free nanocrystals via less expensive synthesis methods than currently available.

1.3 Optical Spectroscopy of CNCs

Due to the numerous opto-electronic applications of CNCs, understanding their optical properties is of primary importance. We outline here the main experimental spectroscopic techniques used in studying CNCs.

1.3.1 Linear Spectroscopies

The most basic types of optical spectroscopies are linear, which involve either a single absorbed or single emitted field. In absorption spectroscopy the sample's optical attenuation is measured while in luminescence (called fluorescence for molecular systems) spectroscopy the sample is prepared in an excited state and the emitted light is measured. These measurements are usually spectrally resolved to reveal information such as energy level structure. In CNCs however, linear techniques are of limited utility due to **inhomogeneous broadening** of spectral lineshapes. Size/shape dispersion and environmental fluctuations will cause every nanocrystal in an ensemble to have varying electronic resonance energies, which "smears" absorption and fluorescence lineshapes into Gaussian peaks reflecting the sample inhomogeneity. Although fluorescence [26], and sometimes absorption [27] (with painstaking effort) may be performed on single nanocrystals to circumvent inhomogeneous broadening, the ensemble-averaged homogeneous properties of CNCs that are relevant to their practical applications must be studied via more sophisticated spectroscopic techniques.

1.3.2 Nonlinear Spectroscopies

Nonlinear spectroscopies, as their name suggests, are characterized by measurement of an optical response that depends nonlinearly on excitation field. While the order of a measured nonlinear response is determined by its excitation intensity dependence, most nonlinear spectroscopic techniques integrate over one or more dimensions of the nonlinear response due to ease of experimental implementation. Examples of such experiments include spectral hole burning [28] and transient absorption spectroscopy [29], which are third-order nonlinear spectroscopies that probe saturation of transitions in the spectral and temporal domains respectively. In the study of CNCs, spectral hole burning has been successfully used to resolve homogeneous lineshapes of CNC ensembles [30, 31] and transient absorption spectroscopy has become an increasingly standard characterization technique of excited state dynamics [32]. However, the most obvious drawback of the above 1-D techniques is the loss of entire dimensions of information for a given system's response. The topic of this thesis is to resolve the nonlinear response of CNCs in all dimensions via so-called **multi-dimensional coherent spectroscopy**. In doing so, we recover rich physics contained in otherwise forfeited dimensions.

1.4 Outline of Thesis

This thesis is organized as follows. Chapter II provides a broad introduction to the synthesis and optical properties of CNCs. The electronic energy structure is first derived for a bulk semiconductor, and the potential barrier of the nanocrystal surface is then included to demonstrate the effects of finite size confinement.

Chapter III then introduces multi-dimensional coherent spectroscopy (MDCS), which is a general technique that describes most of the experiments performed in this thesis. The theory describing multi-dimensional spectra is derived, and double-sided

Feynman diagrams are introduced to facilitate the intuitive interpretation of spectra.

Chapters IV and V discuss our results on CdSe CNCs, which are grown by Wan Ki Bae's synthesis group at Sungkyunkwan University in South Korea. Chapter IV presents one-quantum spectra, which correlate their absorption and emission dynamics. We examine the most prominent feature, which is a broad pedestal arising from coupling to low-energy acoustic vibrations. By comparison to simulations, we argue the simultaneous existence of both acoustic modes discretized by the nanocrystal geometry and continuum acoustic modes that propagate into the surrounding glass lattice. Chapter V subsequently focuses on signatures of coupling to longitudinal optical (LO) modes of CdSe. Zero-quantum spectra, which correlate intraband coherences with their resultant emission spectra, are used to isolate the dynamics of vibrationally-coupled interband coherences. Coupling to LO phonon modes is then shown to induce highly non-Markovian dephasing dynamics.

Chapters VI and VII then present results on MDCS of $CsPbI_3$ perovskite nanocrystals grown by Ana Nogueira's group at University of Campinas in Brazil. Chapter VI discusses $CsPbI_3$ nanocubes, which possess a bright, non-degenerate triplet fine-structure with orthogonally-polarized dipole moments. From the multi-dimensional spectra, we extract the ensemble-averaged triplet coherence times, crucial figures of merit for quantum information processing, and reveal coherence times of both optical triplet coherences and terahertz inter-triplet coherences. We also find evidence for a mixed bright-dark level-ordering that renders the triplet state excitons only partially bright. Chapter VII then discusses $CsPbI_3$ nanoplatelets, which possess unique properties of their own such as drastically reduced inhomogeneous broadening due to precise control of nanoplatelet thickness. To investigate claims of homogeneously broadened emission at room-temperature, we apply MDCS to simultaneously determine the homogeneous and inhomogeneous linewidths of platelets with varying thickness and lateral size. Temperature- and power-dependent measurements reveal

the dominant linewidth broadening mechanisms to be acoustic phonon coupling and excitation induced dephasing. By extrapolating the linear linewidth temperature dependence for 4-layer nanoplatelets, we expect inhomogeneous broadening to remain dominant at room-temperature.

Finally, results on MDCS of nitrogen-vacancy centers in diamond provided by Ronald Ulbricht at the Max Planck Institute for Polymer Research in Mainz, Germany are presented in Appendix E. Though not colloidal, vacancy centers exhibit much physics similar to that of CNCs due to their common characterization as "artificial atoms". The multi-dimensional spectra presented reveal thermal dephasing due to quasi-localized vibrational modes as well as ultrafast spectral diffusion on the picosecond timescale. Additional findings include direct measurement of crucial figures of merit for the spin-polarization cycle, the inter-system crossing time and branching ratio into the spin singlet shelving state, as well as evidence of two lattice orientation families whose resonance energies shift in opposite directions with changing temperature.

References

(1) Ekimov, A.; Efros, A.; Onushchenko, A. *Solid State Communications* **1985**, *56*, 921–924.

(2) L. Efros, A.; L. Efros, A. *Soviet physics. Semiconductors* **1982**, *16*, 772–775.

(3) Brus, L. E. *The Journal of Chemical Physics* **1983**, *79*, 5566–5571.

(4) Rossetti, R.; Nakahara, S.; Brus, L. E. *The Journal of Chemical Physics* **1983**, *79*, 1086–1088.

(5) Brus, L. E. *The Journal of Chemical Physics* **1984**, *80*, 4403–4409.

(6) Rossetti, R.; Ellison, J. L.; Gibson, J. M.; Brus, L. E. *The Journal of Chemical Physics* **1984**, *80*, 4464–4469.

(7) Murray, C. B.; Norris, D. J.; Bawendi, M. G. *Journal of the American Chemical Society* **1993**, *115*, 8706–8715.

(8) Murray, C. B.; Kagan, C. R.; Bawendi, M. G. *Science* **1995**, *270*, 1335–1338.

(9) Colvin, V. L.; Schlamp, M. C.; Alivisatos, A. P. *Nature* **1994**, *370*, 354–357.

(10) Bruchez, M.; Moronne, M.; Gin, P.; Weiss, S.; Alivisatos, A. P. *Science* **1998**, *281*, 2013–2016.

(11) Hines, M. A.; Guyot-Sionnest, P. *The Journal of Physical Chemistry* **1996**, *100*, 468–471.

(12) Hines, M. A.; Guyot-Sionnest, P. *The Journal of Physical Chemistry B* **1998**, *102*, 3655–3657.

(13) Kovalenko, M. V. et al. *ACS Nano* **2015**, *9*, PMID: 25608730, 1012–1057.

(14) Carey, G. H.; Abdelhady, A. L.; Ning, Z.; Thon, S. M.; Bakr, O. M.; Sargent, E. H. *Chemical Reviews* **2015**, *115*, PMID: 26106908, 12732–12763.

(15) Kagan, C. R.; Murray, C. B. *Nature Nanotechnology* **2015**, *10*, Review Article, 1013–1026.

(16) Pietryga, J. M.; Park, Y.-S.; Lim, J.; Fidler, A. F.; Bae, W. K.; Brovelli, S.; Klimov, V. I. *Chemical Reviews* **2016**, *116*, PMID: 27677521, 10513–10622.

(17) Wilhelm, S.; Tavares, A. J.; Dai, Q.; Ohta, S.; Audet, J.; Dvorak, H. F.; Chan, W. C. W. *Nature Reviews Materials* **2016**, *1*, Perspective.

(18) Owen, J.; Brus, L. *Journal of the American Chemical Society* **2017**, *139*, PMID: 28657307, 10939–10943.

(19) Kagan, C. R. *Chemical Society Reviews* **2019**, DOI: 10.1039/C8CS00629F.

(20) Cho, K.-S.; Lee, E. K.; Joo, W.-J.; Jang, E.; Kim, T.-H.; Lee, S. J.; Kwon, S.-J.; Han, J. Y.; Kim, B.-K.; Choi, B. L.; Kim, J. M. *Nature Photonics* **2009**, *3*, Article.

(21) Kim, T.-H.; Cho, K.-S.; Lee, E. K.; Lee, S. J.; Chae, J.; Kim, J. W.; Kim, D. H.; Kwon, J.-Y.; Amaratunga, G.; Lee, S. Y.; Choi, B. L.; Kuk, Y.; Kim, J. M.; Kim, K. *Nature Photonics* **2011**, *5*, Article.

(22) Nozik, A. *Physica E: Low-dimensional Systems and Nanostructures* **2002**, *14*, 115–120.

(23) Schaller, R. D.; Klimov, V. I. *Phys. Rev. Lett.* **2004**, *92*, 186601.

(24) Beard, M. C. *The Journal of Physical Chemistry Letters* **2011**, *2*, PMID: 26295422, 1282–1288.

(25) C., B. M.; C., J. J.; M., L. J.; J., N. A. *Philosophical Transactions of the Royal Society A: Mathematical, Physical and Engineering Sciences* **2015**, *373*, 20140412.

(26) Fernée, M. J.; Tamarat, P.; Lounis, B. *Chem. Soc. Rev.* **2014**, *43*, 1311–1337.

(27) Berciaud, S.; Cognet, L.; Lounis, B. *Nano Letters* **2005**, *5*, PMID: 16277445, 2160–2163.

(28) Völker, S. *Annual Review of Physical Chemistry* **1989**, *40*, 499–530.

(29) Berera, R.; van Grondelle, R.; Kennis, J. T. M. *Photosynthesis Research* **2009**, *101*, 105–118.

(30) Palinginis, P.; Tavenner, S.; Lonergan, M.; Wang, H. *Phys. Rev. B* **2003**, *67*, 201307.

(31) Tavenner-Kruger, S.; Park, Y.-S.; Lonergan, M.; Woggon, U.; Wang, H. *Nano Letters* **2006**, *6*, PMID: 16968043, 2154–2157.

(32) Zhang, Q.; Luo, Y. *High Power Laser Science and Engineering* **2016**, *4*, e22.

CHAPTER II

Fundamentals of Colloidal Nanocrystals (CNCs)

Colloidal nanocrystals (CNCs), which are nanometer sized pieces of material synthesized in solution, are most commonly grown from metals, dielectrics, or semiconductors. In this thesis we primarily discuss those grown from semiconductors and any mention of CNCs are understood to refer to the semiconductor variety unless otherwise indicated.

2.1 Synthesis of CNCs

We now outline a general synthesis scheme that applies to most types of CNCs, and use traditional CdSe core CNCs as an example.

2.1.1 Seed Nucleation and Growth

The first step in colloidal synthesis is to introduce the relevant atoms necessary for nanocrystal growth into a solvent environment. This is done by injecting **precursor** chemicals into the solvent (not necessarily at the same time) at hundreds of degrees Celsius, during which the active atomic or molecular components break off of their original precursors. For CdSe nanocrystals, precursors such as Cadmium Myristate ($C_{28}H_{54}CdO_4$) and Selenium Dioxide (SeO_2) may be used. As the active components (usually called **monomers**) supersaturate the solvent [1], nucleation of nanocrystals

will begin spontaneously. Shells of different material may be subsequently grown by redispersing these seed nanocrystals in new solvents to resume growth in the presence of different precursors.

2.1.2 Growth Termination and Ligand Capping

After the nanocrystals reach a desired size, the growth process is terminated by cooling the solution back to room temperature. However, precipitation at this point will result in unstable nanocrystals that are susceptible to aggregation and continued growth. Therefore it was realized by Murray et al. [2] that they must be coated in a **surfactant** layer, usually in the form of long organic molecules (**ligands**), that stabilize the nanocrystal surface. Common surfactants for CdSe CNCs include alkyl phosphines, fatty acids, etc. [3].

2.1.3 Future Directions in CNC Synthesis

Since its inception, research in CNC synthesis has pushed towards CNCs that satisfy four main criteria:

1. High nanocrystal size/shape uniformity
2. High luminescence quantum yields
3. Narrow emission linewidths
4. Minimized luminescence blinking [4]

Particularly as CNCs begin to mature in a broad range of practical applications, these four criteria must be satisfied simultaneously. Although this has largely been achieved in traditional CdSe-based quantum dots [5], non-toxic CNCs desired for consumer applications have yet to meet these requirements [6].

2.2 Electronic Properties of CNCs

Today, our exquisite control over CNC synthesis enables growth of a variety of nanocrystal shapes (spheres, cubes, rods, etc.) and sizes. While different types of CNCs will exhibit their own unique properties, a common characteristic shared among all of them is quantum confinement of electronic excitations. To demonstrate the effect of confinement on electronic dynamics, we will first examine the general behavior of electrons in a bulk semiconductor and then include boundary conditions imposed by the finite CNC size.

2.2.1 Electrons in a Semiconductor

A typical crystal consists of on the order of 10^{22} atoms/cm^3, with each atom composed of a nucleus and their associated core and valence electrons. Unfortunately, attempting to solve the total many-body Hamiltonian, which consists of the electronic and nuclear kinetic energies as well as all electron-electron, electron-nucleus, and nucleus-nucleus interactions for 10^{22} atoms, is clearly a computational challenge. When dealing with intractable physical systems, our goal is always to simplify the problem via models that preserve key phenomena necessary for explaining experimental observations while simultaneously approximating away unnecessary complexity.

Three common approximations applied are as follows:

1. **Born-Oppenheimer Approximation**: Because atomic nuclei are much heavier than electrons, the nuclear lattice is considered to be stationary on the timescales of electronic motion. In other words, the electronic dynamics depend adiabatically on nuclear motion. The system wavefunction may then be factorized into electronic and nuclear portions with their own equations of motion.

2. **Ionic Nuclei Approximation**: The core electrons of each nucleus are so

tightly bound to their parent nuclei that we consider only interactions between valence electrons and **ionic nuclei** (nucleus + core electrons).

3. **Hartree-Fock Approximation**: Interactions between each valence electron and the ionic nuclei are described in terms of an effective periodic potential. Electronic correlation effects are neglected. However, phenomena such as excitation-induced shift [7] and excitation-induced dephasing (see Chapter VII) cannot be explained within the framework of this approximation.

The original many-body Schrodinger equation thus simplifies to that of a single valence electron in a periodic potential $U(\mathbf{r})$:

$$\left[-\frac{\hbar^2}{2m_0}\nabla^2 + U(\mathbf{r})\right]\psi = E\psi \tag{2.1}$$

which has solutions taking the form of a plane wave $e^{i\mathbf{k}\cdot\mathbf{r}}$ modulated at the same periodicity of the potential, or the so-called **Bloch states** [8, 9]. Because these Bloch states are delocalized in position space $\mathbf{r}$ and indexed by the quasi-momentum wavevector $\mathbf{k}$, it is useful to consider their dispersion relation (eigenenergy E as a function of $\mathbf{k}$). Consider that of CdSe for example, plotted in Fig. 2.1:

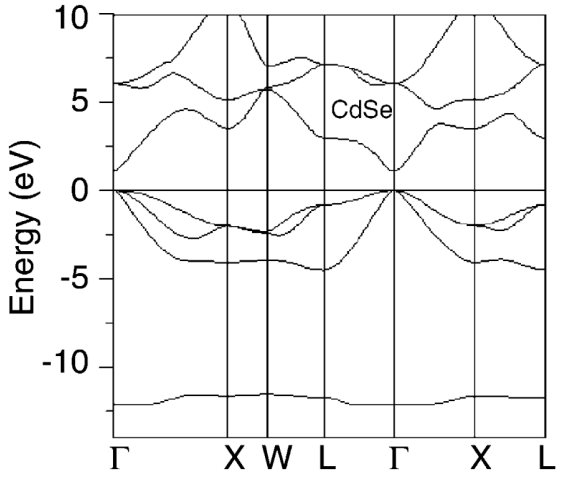

Figure 2.1: Bandstructure of CdSe (adapted from [10]). The high-symmetry points Γ/X/W/L are as labeled.

One of the most important features shown in Figure 2.1 is a range of energies, approximately between 0 and 1.7 eV, that are forbidden. This is the **bandgap** of CdSe, and such energy gaps are a universal feature of insulators and semiconductors. The existence of energy bands is also the reason why the electronic dispersion relation of a material is called its **bandstructure**. In semiconductors, the states directly below the bandgap (valence band) are mostly full and the states directly above (conduction band) are mostly empty. The interaction of a semiconductor with light thus involves exciting electrons from valence band states into conduction band states.

2.2.2 Electron, Hole, and Exciton Quasi-Particles

Recall the free-particle dispersion relation for an electron of mass m_0 [8, 9]:

$$E = \frac{\hbar^2 k^2}{2m_0}\,. \tag{2.2}$$

When exciting with light of photon energy near the bandgap of a semiconductor, transitions occur between the valence band maximum (at wavevector k_v and energy E_v^0) and conduction band minimum (at wavevector k_c and energy E_c^0). In these regions, the energy dispersion is approximately parabolic:

$$\begin{aligned} E_{c/v}(k) &= E_{c/v}^0 + (k - k_{c/v})\left.\frac{dE_{c/v}}{dk}\right|_{k=k_{c/v}} + \frac{1}{2}(k-k_{c/v})^2\left.\frac{d^2E_{c/v}}{dk^2}\right|_{k=k_{c/v}} + \ldots \\ &\approx E_{c/v}^0 + \frac{1}{2}(k-k_{c/v})^2\left.\frac{d^2E_{c/v}}{dk^2}\right|_{k=k_{c/v}} \\ &= E_{c/v}^0 + \frac{\hbar^2(k-k_{c/v})^2}{2m_{c/v}^*} \end{aligned} \tag{2.3}$$

where in the last line we have defined the **effective mass** $m_{c/v}^*$:

$$\frac{1}{m_{c/v}^*} = \frac{1}{\hbar^2}\left.\frac{d^2E_{c/v}}{dk^2}\right|_{k=k_{c/v}}\,. \tag{2.4}$$

Comparing equation (2.3) to the free-particle dispersion relation (2.2), we find that an electron in the valence or conduction band will behave as if it were free but with an effective mass $m^*_{c/v}$. This is the concept of an **electron quasi-particle**. Because our experiments all take place within condensed systems, we will refer to electron quasi-particles simply as electrons for simplicity.

The above description of electron quasi-particles was derived for a generic band-structure found by solving the effective potential Schrodinger equation (2.1). It does not, however, account for Pauli blocking due to occupation of an energy band. In the mostly unoccupied conduction band electrons may be considered electron quasi-particles, but in the mostly occupied valence band a different picture is necessary. There, the collective response of all valence band electrons is determined by the *un-occupied* valence band states. We treat each vacant valence band state as an effective particle with effective mass m^*_v and positive charge $+e$, called a **hole quasi-particle**.

From our discussion of electron and hole quasi-particles, it is clear that above-bandgap excitation of a semiconductor necessarily creates both an electron and hole simultaneously. These oppositely charged quasi-particles may then experience an attractive Coulomb potential, and their bound-state is called an **exciton quasi-particle**. The exciton equation of motion is described by the following hydrogenic Hamiltonian:

$$H = -\frac{\hbar^2}{2m^*_e}\nabla^2_e - \frac{\hbar^2}{2m^*_h}\nabla^2_h - \frac{e^2}{\epsilon|\mathbf{r}_e - \mathbf{r}_h|} \tag{2.5}$$

where ϵ is the dielectric constant of the semiconductor and $\mathbf{r}_e$ and $\mathbf{r}_h$ are the electron and hole coordinates respectively. Defining the electron-hole separation $\mathbf{r}$ and center of mass coordinate $\mathbf{R}$:

$$\mathbf{r} = \mathbf{r}_h - \mathbf{r}_e \qquad \mathbf{R} = \frac{m^*_e\mathbf{r}_e - m^*_h\mathbf{r}_h}{m^*_e + m^*_h} \tag{2.6}$$

and the reduced and combined masses:

$$\mu = \frac{m_e^* m_h^*}{m_e^* + m_h^*} \qquad M = m_e^* + m_h^* \tag{2.7}$$

The Hamiltonian (2.5) may then be recast and separated by its center of mass and internal degrees of freedom:

$$H = -\frac{\hbar^2}{2M}\nabla_R^2 - \left[\frac{\hbar^2}{2\mu}\nabla_r^2 + \frac{e^2}{\epsilon r}\right] \tag{2.8}$$

The first term describes the exciton center of mass motion while the second bracketed term describes internal states arising from the electron-hole Coulomb interaction. It is then straightforward to factorize the exciton wavefunction into a plane wave due to center of mass motion and hydrogenic bound states [9], resulting in the eigenenergies:

$$E_n(k) = -\frac{\hbar^2 k^2}{2M} - \frac{Ry}{n^2} \tag{2.9}$$

where we have defined the exciton Rydberg energy Ry and exciton Bohr radius a_B:

$$Ry = \frac{e^2}{2\epsilon a_B} \qquad a_B = \frac{\epsilon \hbar^2}{\mu e^2} \tag{2.10}$$

In direct correspondence to hydrogenic bound states, the exciton Bohr radius may be thought of as an exciton bound state's spatial extent (1/e radius for the ground state wavefunction). The total exciton wavefunction is then delocalized according to its center of mass motion.

2.2.3 Weak Confinement Regime

We now include the finite size of a CNC, taking a spherical nanocrystal as an example. In an ideal spherical CNC, the confinement potential $U(r)$ is clearly spherically symmetric. The most natural way to solve such problems is in a spherical

coordinate system:

$$x = r\sin(\theta)\cos(\phi) \qquad y = r\sin(\theta)\sin(\phi) \qquad z = r\cos(\theta) \tag{2.11}$$

or conversely:

$$r = \sqrt{x^2 + y^2 + z^2} \qquad \phi = tan^{-1}\left(\frac{y}{x}\right) \qquad \theta = cos^{-1}\left(\frac{z}{\sqrt{x^2 + y^2 + z^2}}\right) \tag{2.12}$$

which recasts the Hamiltonian as:

$$H = -\frac{\hbar^2}{2Mr^2}\frac{\partial}{\partial r}\left(r^2\frac{\partial}{\partial r}\right) - \frac{\hbar^2}{2M\sin(\theta)r^2}\left[\frac{\partial}{\partial\theta}\left(\sin(\theta)\frac{\partial}{\partial\theta}\right) + \frac{1}{\sin(\theta)}\frac{\partial^2}{\partial\phi^2}\right] + U(r) \tag{2.13}$$

Here, by using the total exciton mass M in the Hamiltonian we assume that only the exciton center of mass motion is confined. This assumption is valid if the CNC radius a is at least a few times larger than the exciton Bohr radius, which is called the **weak confinement regime**. The procedure for solving the above Hamiltonian by separation of variables is well-known [9], and we present only the results here. The eigenstates will assume the form:

$$\psi_{n\ell m}(r,\theta,\phi) = \frac{u_{n\ell}(r)}{r}Y_{\ell m}(\theta,\phi) \tag{2.14}$$

where $Y_{\ell m}$ are the spherical harmonics and the radial portion $u_{n\ell}(r)$ is determined by the equation:

$$-\frac{\hbar^2}{2M}\frac{d^2u}{dr^2} + \left[U(r) + \frac{\hbar^2}{2Mr^2}\ell(\ell+1)\right]u = Eu \tag{2.15}$$

The simplest way to model a confinement potential for a CNC is an infinite spherical potential well:

$$U(r) = \begin{cases} 0 & \text{for } r \leq a \\ \infty & \text{for } r > a \end{cases} \tag{2.16}$$

which gives the eigenenergies:

$$E_{n\ell} = \frac{\hbar^2 \chi_{n\ell}^2}{2Ma^2} \tag{2.17}$$

where $\chi_{n\ell}$ are the roots of the spherical Bessel functions. The exciton eigenenergies thus have contributions from both its internal states (indexed by quantum number n') and size confinement (indexed by quantum numbers n and ℓ):

$$E_{n'n\ell} = E_g - \frac{Ry}{n'^2} + \frac{\hbar^2 \chi_{n\ell}^2}{2Ma^2} \tag{2.18}$$

Note that in the weak confinement limit ($a \gg a_B$), the confinement energy is small compared to the Rydberg energy, which means the electron and hole dynamics are primarily determined by their Coulomb interaction. The exciton states are commonly labeled in spectroscopic notation (1S, 2S, 2P, ...), but the internal states arising from Coulomb interaction and external states due to nanocrystal size confinement must be distinguished. The usual procedure is thus to label the internal states indexed by n' by capital letters (1S, 2S, 2P, ...) and the external states indexed by n and ℓ by lowercase letters (1s, 2s, 2p, ...).

2.2.4 Strong Confinement Regime

We now consider the situation in which the nanocrystal radius is much smaller than the exciton Bohr radius ($a \ll a_B$). In this limit the Coulomb potential becomes

unimportant in comparison to the individual electron and hole confinement energies, giving the eigenenergies:

$$\begin{aligned} E_{n\ell} &= E_g + \frac{\hbar^2 \chi_{n\ell}^2}{2m_e a^2} + \frac{\hbar^2 \chi_{n\ell}^2}{2m_h a^2} \\ &= E_g + \frac{\hbar^2 \chi_{n\ell}^2}{2\mu a^2} \end{aligned} \tag{2.19}$$

Because the energy spectrum is now determined by the nanocrystal size, CNCs in the strong confinement regime are sometimes termed **artificial atoms**.

2.3 Optical Properties of CNCs

Because most applications of CNCs involve their interaction with light via absorption, emission, or both, the optical properties of CNCs are of utmost importance. The discrete energy levels of CNCs described in the previous section would suggest atomic-like spectra, but their absorption and emission dynamics are more complicated in many ways.

2.3.1 Inhomogeneous Broadening

As mentioned in Chapter I, absorption and fluorescence lineshapes of CNCs are inhomogeneously broadened. We now elaborate on the physical origin of inhomogeneous broadening and how this phenomenon modifies spectral lineshapes.

Generally, inhomogeneous broadening is a phenomenon that affects the optical response from an ensemble of absorbers/emitters in which variations in resonance energy among the ensemble broaden the overall spectral lineshapes. A spectrum is said to be inhomogeneously broadened if the distribution in resonance frequency is much larger than the linewidth of an individual element of the ensemble (called the **homogeneous linewidth**). This situation is shown schematically in Fig. 2.2a:

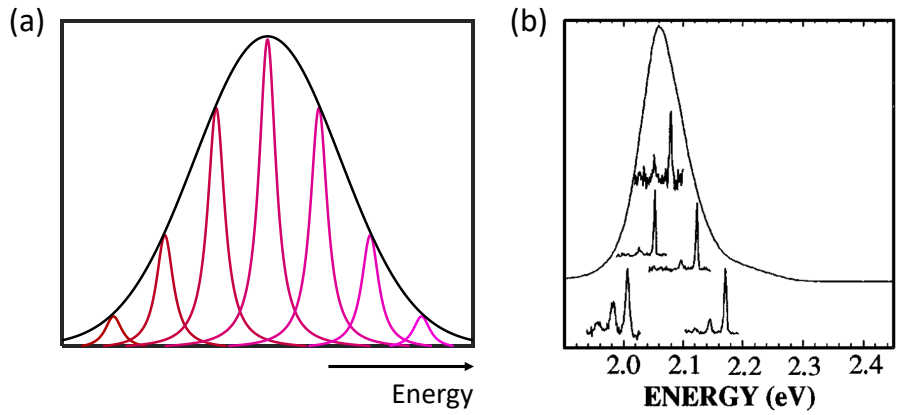

Figure 2.2: (a) Schematic of inhomogeneously broadened lineshape (black) and underlying homogeneous lineshapes (colored). (b) Inhomogeneously broadened fluorescence of an ensemble of 5 nm diameter CdSe CNCs (top). Fluorescence of single CNCs isolated from the ensemble (bottom). Figure (b) adapted from [11].

The dominant source of inhomogeneous broadening in CNCs is unavoidable nanocrystal size-dispersion that arises from the growth process. Variation in nanocrystal size, and therefore quantum confinement energy, results in strongly inhomogeneously broadened absorption and emission as shown in Fig. 2.2b. It should be noted that atomic spectra are also inhomogeneously broadened to a lesser degree, albeit by a different physical mechanism, Doppler broadening [12].

2.3.2 Static Lattice Coupling

The discrete energy levels of CNCs derived in the previous section are in reality energy surfaces as a function of lattice configuration. From a static point of view, in which the lattice deforms adiabatically in response to electronic dynamics, this gives rise to two main phenomena.

First, the lattice constant changes with temperature. This results in resonance energies that depend linearly on temperature.

Second, fluorescence from CNCs generally occurs at lower energy in comparison to absorption. This energy difference is called the **Stokes shift**, and occurs following initial absorption of light due to lattice relaxation towards a minimum in the electronic

potential energy surface.

2.3.3 Dynamic Lattice Coupling

Despite their small size, a characteristic that CNCs inherit from their bulk counterparts is electron-phonon coupling, where **phonons** are lattice vibrations of a material. Various types of phonons are possible, such as acoustic phonon modes that span a continuum of energies and optical phonon modes that are characterized by discrete energies. A general property of all such types of phonons is that periodic lattice oscillations associated with various phonon modes modulate electronic dynamics and distort spectral lineshapes of CNCs from ideal Lorentzians. We will discuss this topic in greater detail in Chapter IV.

References

(1) Reiss, P. In, Rogach, A. L., Ed.; Springer Vienna: Vienna, 2008; Chapter Synthesis of semiconductor nanocrystals in organic solvents, pp 35–72.

(2) Murray, C. B.; Norris, D. J.; Bawendi, M. G. *Journal of the American Chemical Society* **1993**, *115*, 8706–8715.

(3) Heinz, H.; Pramanik, C.; Heinz, O.; Ding, Y.; Mishra, R. K.; Marchon, D.; Flatt, R. J.; Estrela-Lopis, I.; Llop, J.; Moya, S.; Ziolo, R. F. *Surface Science Reports* **2017**, *72*, 1–58.

(4) Efros, A. L.; Nesbitt, D. J. *Nature Nanotechnology* **2016**, *11*, Review Article, 661–671.

(5) Chen, O.; Zhao, J.; Chauhan, V. P.; Cui, J.; Wong, C.; Harris, D. K.; Wei, H.; Han, H.-S.; Fukumura, D.; Jain, R. K.; Bawendi, M. G. *Nature Materials* **2013**, *12*, Article, 445–451.

(6) Kovalenko, M. V. et al. *ACS Nano* **2015**, *9*, PMID: 25608730, 1012–1057.

(7) Shacklette, J. M.; Cundiff, S. T. *Physical Review B* **2002**, *66*, 045309.

(8) Ashcroft, N.; Mermin, D., *Solid State Physics*, 1st ed.; Cengage Learning: 1976.

(9) Liboff, R., *Introductory Quantum Mechanics*, 4th ed.; Addison-Wesley: 2002.

(10) Deligoz, E.; Colakoglu, K.; Ciftci, Y. *Physica B: Condensed Matter* **2006**, *373*, 124–130.

(11) Empedocles, S. A.; Norris, D. J.; Bawendi, M. G. *Physical Review Letters* **1996**, *77*, 3873–3876.

(12) Demtröder, W. In; Springer Berlin Heidelberg: Berlin, Heidelberg, 2014; Chapter Widths and Profiles of Spectral Lines, pp 75–111.

CHAPTER III

Multi-Dimensional Coherent Spectroscopy

3.1 History

The history of multi-dimensional Fourier transform spectroscopy may be traced back to a proposal by Jean Jeener at a NMR summer school in 1971 [1]. Though this 2-D Fourier transform experiment was thought even by Jeener to be too demanding for the computing power available at the time, in the audience sat a student of Richard Ernst who took diligent notes. Ernst's group then proceeded to publish both the first theoretical [2] and experimental [3] studies on 2-D NMR spectroscopy, for which Richard Ernst won the 1991 Nobel Prize in chemistry.

In 1993, Tanimura and Mukamel proposed the application of 2-D Fourier transform spectroscopy in the optical regime to study molecular vibrations [4]. In 1998 the first 2-D optical spectroscopy of electronic transitions was demonstrated by David Jonas' group [5] followed by extension to the infrared regime by Hochstrasser's group to probe vibrational transitions directly in 1999 [6]. These pioneering experiments initiated intense activity in 2-D spectroscopy of molecular systems, and in 2005 the Cundiff group reported the first 2-D optical spectroscopy on semiconductors [7, 8].

Since the first experiments, the term 2-D spectroscopy has predominantly been used to describe experiments that correlate absorption and emission dynamics during the first and third evolution periods in a so-called one-quantum spectrum. However,

coherent time-domain Fourier transform spectroscopy also provides other types of 2-D spectra such as zero-quantum [9] and two-quantum [10] spectra, which represent different cross-sections of the frequency-domain third-order nonlinear response. Furthermore, in 2000 Park and Cho suggested theoretically [11] the extension of 2-D spectroscopy into a third dimension. So-called 3-D spectroscopy of a fifth-order nonlinear response was first demonstrated in 2007 by Zanni's group [12], and that of a third-order nonlinear response by Nelson's group in 2009 [13]. We thus use the general terminology **multi-dimensional coherent spectroscopy (MDCS)** to refer to all spectroscopic techniques that measure a system's complex frequency-domain nonlinear response without integrating across any of its dimensions.

3.2 Four-Wave Mixing (FWM) Spectroscopy

In the perturbative regime, the polarization of a material induced by an incident field may be expanded in powers of the field:

$$P(t') = P^{(1)}(t') + P^{(2)}(t') + P^{(3)}(t') + \dots \tag{3.1}$$

where $P^{(n)}(\tau)$ represents the nth order nonlinear polarization. We ignore the spatial dependences of the fields and polarization for clarity. By a perturbative expansion of the system density matrix, it may be shown (see Appendix A and [14]) that the nth order nonlinear polarization can be expressed as:

$$\begin{aligned} P^{(n)}(t') &= \int_0^\infty \int_0^\infty \cdots \int_0^\infty S^{(n)}(t_1, \dots, t_{n-1}, t_n) \\ &\qquad E(t' - t_n)E(t' - t_n - t_{n-1}) \dots E(t' - t_n - t_{n-1} \cdots - t_1) dt_1 \dots dt_{n-1} dt_n \\ &= \int_{-\infty}^{t'} \int_{-\infty}^{\tau_n} \cdots \int_{-\infty}^{\tau_2} S^{(n)}(\tau_2 - \tau_1, \dots, \tau_n - \tau_{n-1}, t' - \tau_n) \\ &\qquad E(\tau_n)E(\tau_{n-1}) \dots E(\tau_1) d\tau_1 \dots d\tau_{n-1} d\tau_n \end{aligned} \tag{3.2}$$

where the quantity $S^{(n)}(t_1, \ldots, t_{n-1}, t_n)$ is called the **nth order optical response function**. Each term governs the respective nonlinear optical response we measure and together they contain all of the microscopic information about our system. In general, MDCS encompasses a broad range of techniques that measure a nonlinear response function of arbitrary order. Here we restrict our focus to time-domain four-wave mixing (FWM) experiments that probe a sample's third-order nonlinear response, but the concepts and theory developed in this chapter are easily generalized to other MDCS techniques.

3.2.1 Time-Domain FWM Experiments

The most general time-domain FWM experiment consists of three laser pulses with variable inter-pulse delays:

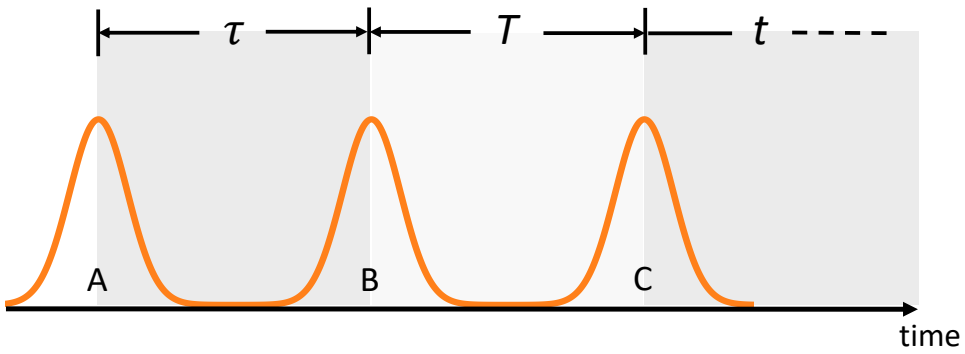

Figure 3.1: Schematic of the three pulses of a time-domain FWM experiment. The inter-pulse delays are denoted τ and T while the evolution time t of the FWM signal is defined after the last pulse.

To understand the relation between the polarization induced by these three pulses and a system's third-order nonlinear optical response function, we take the limit of vanishingly short pulses of infinite bandwidth. In this limit, the combined electric fields of the three pulses may be expressed as delta functions:

$$E(t') = E_A\delta(t') + E_B\delta(t' - \tau) + E_C\delta(t' - T - \tau) \tag{3.3}$$

where we've neglected the complex phase of each field here for simplicity. Before plugging this field into equation (3.2) for third-order ($n = 3$), we note that, due to causality, the response function is only non-zero when all three time arguments are positive [14, 15]. This enforces a direct correspondence between each field term in the third-order polarization and a specific pulse in a three-pulse experiment. The third-order polarization thus becomes:

$$\begin{aligned} P^{(3)}(t') &= \int_{-\infty}^{t'} \int_{-\infty}^{\tau_3} \int_{-\infty}^{\tau_2} S^{(3)}(\tau_2 - \tau_1, \tau_3 - \tau_2, t' - \tau_3) \\ &\qquad E_C \delta(\tau_3 - \tau - T) E_B \delta(\tau_2 - \tau) E_A \delta(\tau_1) d\tau_1 d\tau_2 d\tau_3 \\ &= S^{(3)}(\tau, T, t' - \tau - T) \\ &= S^{(3)}(\tau, T, t) \end{aligned} \tag{3.4}$$

This equation states that three impulsive excitations directly sample $S^{(3)}$. By varying the time-delays $\{\tau, T, t\}$ we can map out desired portions of the third-order optical response function in the time-domain.

3.2.2 Multi-Dimensional Spectra

Upon measuring the time-domain response function in N dimensions, Fourier transform along those axes [16] returns a N-dimensional spectrum that reflects the desired frequency-domain optical response. Most commonly, a Fourier transform along two time delays is performed to obtain a 2-D spectrum as a function of a third temporal variable. In this thesis we measure and analyze two types of spectra resulting from transforming along the time delays $\{\tau, t\}$ and $\{T, t\}$, which we call **one-quantum** and **zero-quantum** 2-D spectra respectively. Each spectrum reflects different cross-sections of the complete three-dimensional (third-order) optical response, and reveals unique aspects of the underlying microscopic physics. An example of each type of 2-D spectrum and its corresponding time-domain representation is shown in Fig. 3.2:

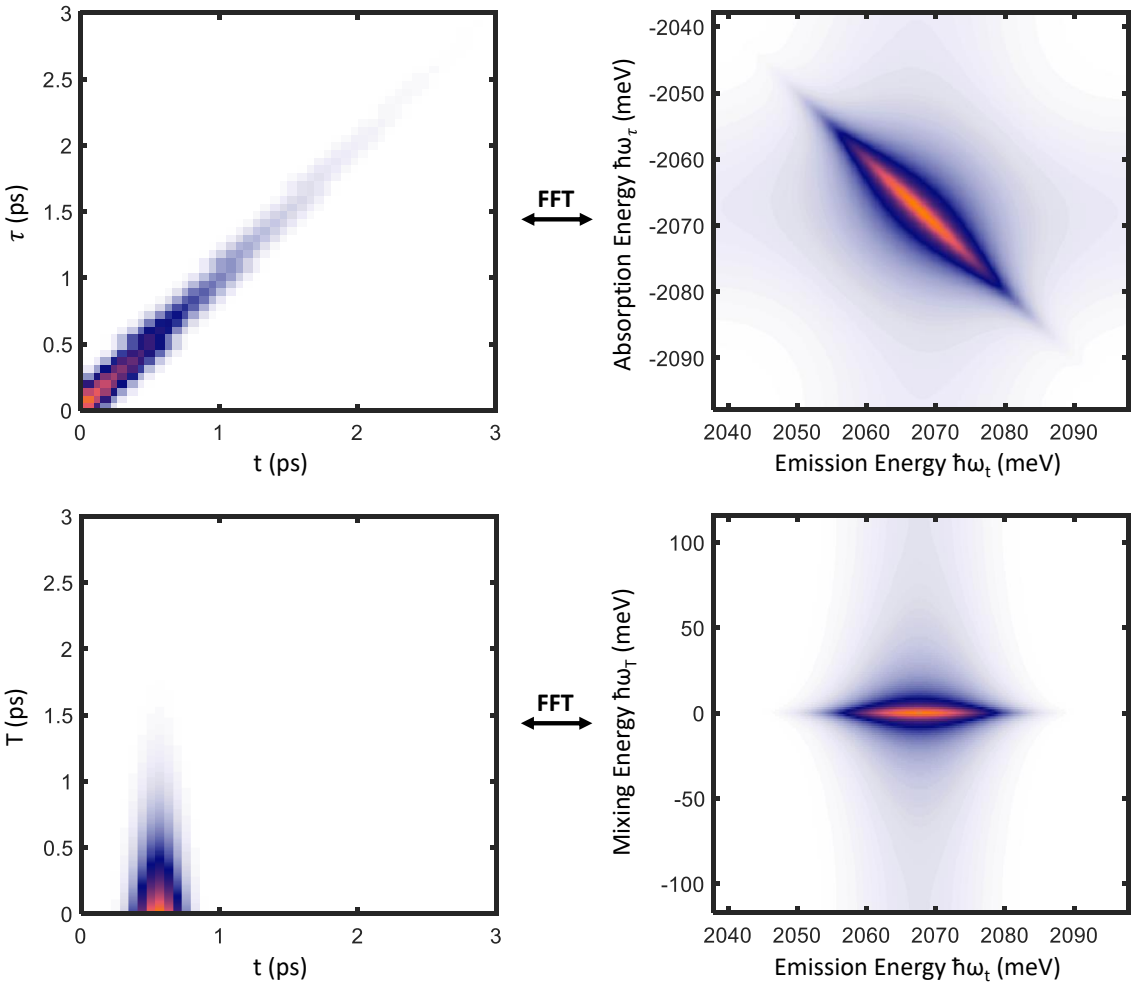

Figure 3.2: $|S^{(3)}|$ within the rotating-wave approximation are related in the time- and frequency-domains by Fourier transform. The responses are simulated with parameters $\gamma = 1$ THz, $\sigma = 10\gamma$, and $\hbar\omega_0 = 2067$ meV (500 THz). One-quantum (top row) and zero-quantum (bottom row) spectra are obtained by measurements along different temporal variables $\{\tau, t\}$ and $\{T, t\}$ respectively. In the one-quantum spectrum the signal manifests along the plot diagonal ($|\hbar\omega_\tau| = |\hbar\omega_t|$), which corresponds to identical absorption and emission energies. Its negative absorption energy axis reflects opposite-sign phase evolution during delays τ and t (see Section 3.4).

It is immediately apparent that the one-quantum and zero-quantum spectra shown in the top and bottom rows of Fig. 3.2 are qualitatively different, which suggests that they provide complementary information. We will discuss the unique aspects of each 2-D spectrum and the functional form of their underlying optical response functions in Section 3.4.

3.3 Experimental Implementation

Because MDCS provides the maximum amount of information about a system's optical response, there is a corresponding, greater complexity in its experimental realization (compared to linear absorption/luminescence or lower-dimensional FWM spectroscopies). We now review the main principles underlying an MDCS experiment, and outline our particular implementation.

3.3.1 Isolating the FWM Signal

Though equation (3.4) defines the third-order polarization induced by three impulsive excitations, we have neglected both higher- and lower-order polarizations. This may seem unreasonable, especially since the linear and second-order (if present) responses are usually stronger than that of third-order, but we isolate the emitted four-wave mixing signal by a technique known as **phase-matching**[1].

As its name suggests, the phase-matching technique relies on the phases of the excitation fields, which we have neglected thus far. Each field may be explicitly expressed in terms of its envelope and phase:

$$E(t) = \mathcal{E}(t)\left(e^{+i\omega t - i\mathbf{k}\cdot\mathbf{r} - i\phi} + e^{-i\omega t + i\mathbf{k}\cdot\mathbf{r} + i\phi}\right) \tag{3.5}$$

Neglecting the arbitrary phase ϕ for clarity, equation (3.4) then becomes:

$$\begin{aligned} P^{(3)}(\mathbf{r}, t') = \int_{-\infty}^{t'}\int_{-\infty}^{\tau_3}\int_{-\infty}^{\tau_2} & S^{(3)}(\tau_2 - \tau_1, \tau_3 - \tau_2, t' - \tau_3) \\ & \mathcal{E}_C(\tau_3)\left(e^{+i(\mathbf{k}_C\cdot\mathbf{r} - \omega_C\tau_3)} + e^{-i(\mathbf{k}_C\cdot\mathbf{r} - \omega_C\tau_3)}\right) \\ & \mathcal{E}_B(\tau_2)\left(e^{+i(\mathbf{k}_B\cdot\mathbf{r} - \omega_B\tau_2)} + e^{-i(\mathbf{k}_B\cdot\mathbf{r} - \omega_B\tau_2)}\right) \\ & \mathcal{E}_A(\tau_1)\left(e^{+i(\mathbf{k}_A\cdot\mathbf{r} - \omega_A\tau_1)} + e^{-i(\mathbf{k}_A\cdot\mathbf{r} - \omega_A\tau_1)}\right) d\tau_1 d\tau_2 d\tau_3 \end{aligned} \tag{3.6}$$

[1]The term phase-matching in the present context should be distinguished from its more common use in the context of maximizing the efficiency of nonlinear optical interactions in a medium.

The exponential factors within the parentheses may then be multiplied to give eight distinct terms that each radiate in a different direction defined by the wavevectors $\mathbf{k} = \pm\mathbf{k}_A \pm \mathbf{k}_B \pm \mathbf{k}_C$. Consider the three excitation pulses arranged in the following **box geometry** [17]:

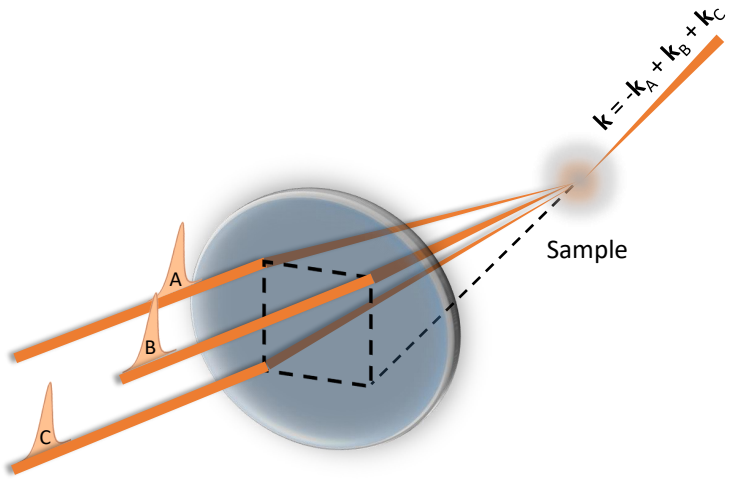

Figure 3.3: Schematic of the box geometry.

where the FWM signal is collected in the emission direction $\mathbf{k} = -\mathbf{k}_\mathrm{A} + \mathbf{k}_\mathrm{B} + \mathbf{k}_\mathrm{C}$. Only a FWM signal arising from all three pulses is emitted in this direction, while other linear and second-order signals, as well as third-order signals arising from single pulses acting multiple times, are directed elsewhere[2]. This method of isolating the FWM signal in the spatial domain is called wave-vector phase-matching. We note that MDCS experiments have also been implemented in collinear geometries by frequency-domain phase-cycling, in which each pulse is shifted by a unique radio-frequency via acousto-optic modulators [18–20].

3.3.2 Measuring the FWM Field

In most spectroscopic techniques, the intensity of an optical response is measured. In contrast, MDCS requires simultaneous measurement of both the signal field ampli-

[2]This is why the box-CARS geometry is described as **background-free**.

tude and phase to completely characterize the optical response of a given order. This may be accomplished via spectral interferometry [21], in which a signal is interfered with a so-called local-oscillator[3] pulse:

$$\begin{aligned} I_{det}(\omega) &\propto \left|\mathcal{F}\left\{E_{sig}(t) + E_{LO}(t)\right\}\right|^2 \\ &\propto \left|E_{sig}(\omega) + E_{LO}(\omega)\right|^2 \\ &\propto I_{sig}(\omega) + I_{LO}(\omega) + 2\mathrm{Re}\left\{E_{sig}(\omega)E^*_{LO}(\omega)\right\} \end{aligned} \tag{3.7}$$

By subtracting the signal and local-oscillator spectra $I_{sig}(\omega)$ and $I_{LO}(\omega)$ respectively, we effectively measure the signal via the third interference term. This is known as **heterodyne detection**, which has two distinct advantages:

1. The interference term is dependent on the phase difference between the signal and local-oscillator fields, allowing for phase-sensitive measurements.

2. The interference term depends linearly on the (usually stronger) local-oscillator field, allowing for more sensitive measurements of weak signal.

For the purposes of heterodyne-detection, box-CARS geometry experiments usually involve another, separate pulse in addition to the three excitation pulses. This is in contrast to **self-heterodyne detection**, in which one of the excitation beams travels in the signal direction and acts as the local-oscillator.

3.3.3 Phase-Stability Criteria

After measurement of the optical response function in the time-domain, the single step of Fourier transforming into the frequency-domain remains. Yet this represents arguably the most challenging aspect of MDCS at optical frequencies, primarily due to what we call the **phase-stability criteria**.

[3]Local-oscillator is terminology borrowed from radio waves.

To understand why phase-stability is essential in MDCS experiments, consider a material with an optical resonance of frequency ω_0. As will be discussed later, such a material's third-order optical response will consist of oscillatory terms of the form $e^{\pm i\omega_0\tau}$ and $e^{\pm i\omega_0 t}$. Any experimental uncertainty in the time-delays τ and t will therefore translate into uncertainty in the resonance frequency:

$$e^{\pm i\omega_0(\tau+\delta\tau)} \rightarrow e^{\pm i[\omega_0+\delta\omega(\tau)]\tau} \qquad e^{\pm i\omega_0(t+\delta t)} \rightarrow e^{\pm i[\omega_0+\delta\omega(t)]t} \tag{3.8}$$

where we've defined the fractional uncertainties $\delta\omega(\tau) = \omega_0\frac{\delta\tau}{\tau}$ and $\delta\omega(t) = \omega_0\frac{\delta t}{t}$. This is why time-delay uncertainty produces noise in a multi-dimensional spectrum:

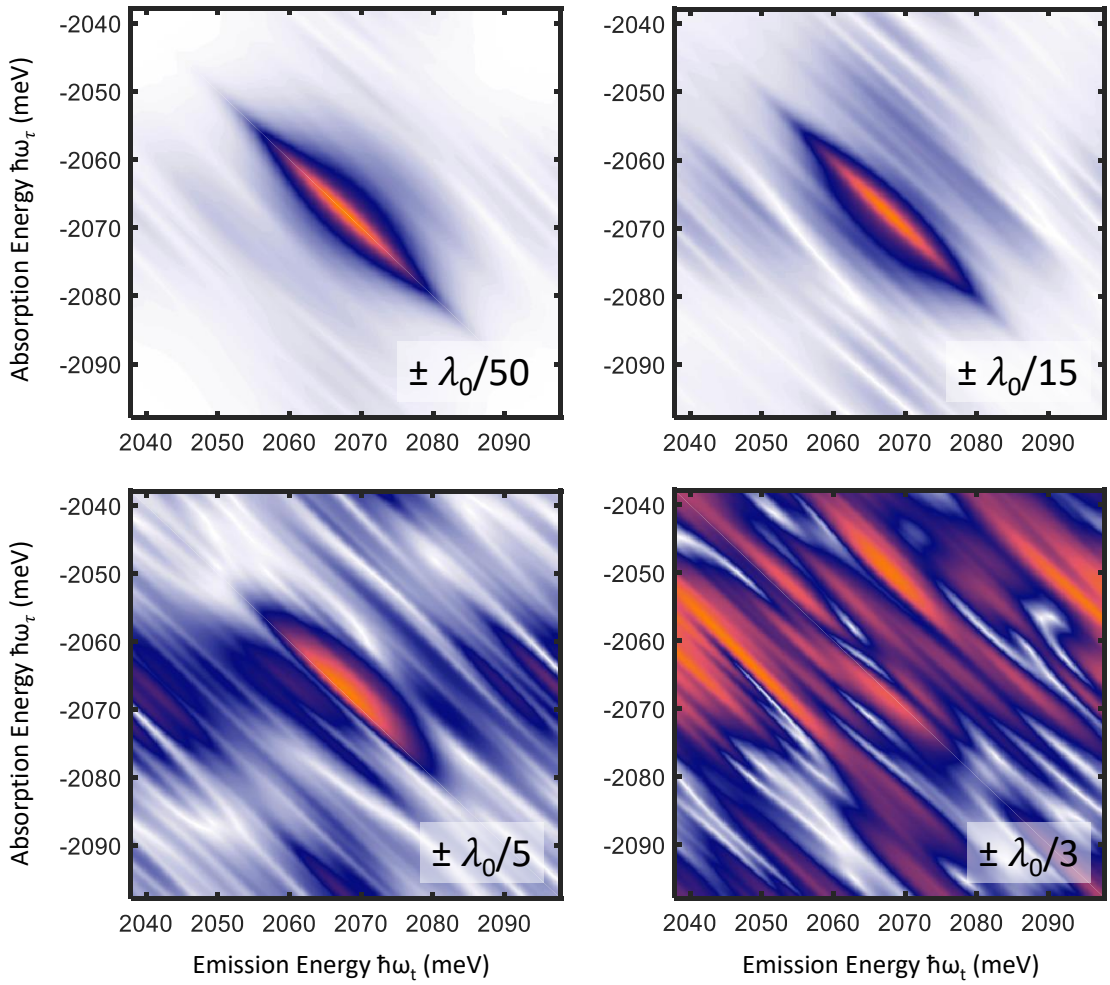

Figure 3.4: 2-D spectra obtained via Fourier transform of the time-domain optical response in Fig. 3.2 for varying pulse delay uncertainty (in terms of $\lambda_0 = \frac{2\pi c}{\omega_0}$).

Fig. 3.4 demonstrates that, to obtain multi-dimensional spectra of acceptable signal to noise ratio, path length fluctuations must be suppressed beneath $\pm\lambda_0/50$. This may be accomplished by either passively stable experimental approaches or active path length stabilization via feedback loops [22]. We note however that the phase-stability criteria may be circumvented if the path-length fluctuations are monitored concurrently with signal acquisition, as is often done in frequency-domain phase-matching MDCS experiments [18–20].

3.3.4 Multi-Dimensional Optical Nonlinear Spectrometer

To implement MDCS in this dissertation, we use a multi-dimensional optical nonlinear spectrometer (originally dubbed the JILA-MONSTR [23]). A MONSTR takes pulses of light as input and, through sequences of mirrors, beamsplitters, and mechanical delay stages, generates four identical copies of each pulse that are arranged in the box geometry with arbitrary temporal delay. A FWM signal is generated by three of the pulses, and is then heterodyne detected with the fourth pulse inside a grating spectrometer. To satisfy the phase-stability criteria, a continuous-wave laser (of 532 nm wavelength in our experiment) co-propagates along the path of each pulse and is reflected by a dichroic mirror at the output port to form nested Michelson interferometers. These retro-reflected beams are then interfered on photo-diodes to provide feedback for servo loops (each connected to a piezoelectric-mounted mirror in each interferometer) that suppress path-length fluctuations beneath $\lambda_0/100$ [23]. Active monitoring of each photo-diode signal during stage movement then ensures accurate stepping of each respective time delay. A schematic representation is shown below in Fig. 3.5.

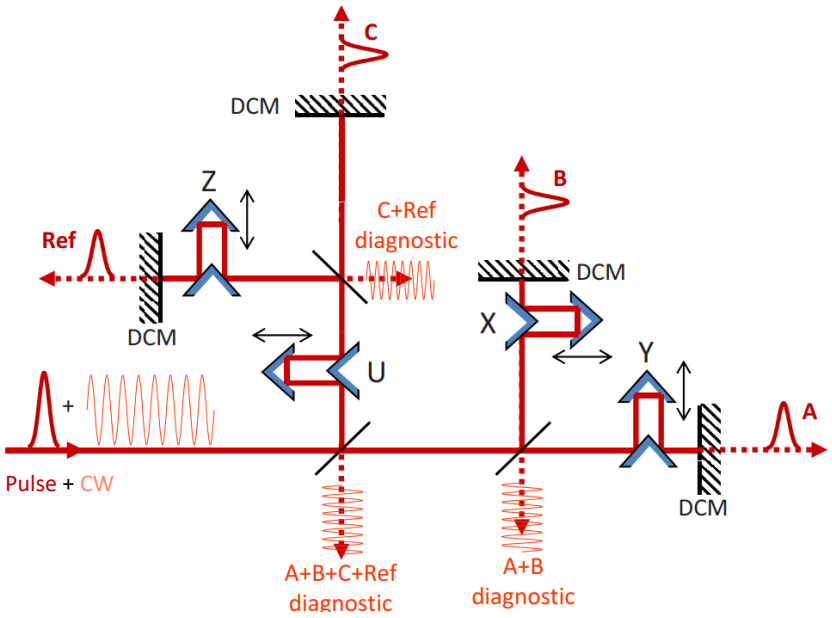

Figure 3.5: Schematic optical diagram of the MONSTR, which splits laser pulses into four identical copies that each traverse a mechanical stage (labeled X, Y, U, and Z) that provides a temporal delay. A co-propagating continuous-wave (CW) laser is reflected by a dichroic mirror (DCM) at the output port to form nested interferometers. Figure adapted from [23].

3.3.5 Laser Source

To perform MDCS, it is important to generate laser pulses from a source that satisfies three criteria: (1) able to reach the wavelength of the sample absorption resonance, (2) possesses sufficient spectral bandwidth to resolve the entire homogeneous lineshape, and (3) generates pulses at a repetition rate slower than the sample population relaxation time to avoid accumulation effects.

The results presented in this dissertation were acquired with pulses sourced from an optical parametric amplifier (Coherent OPA 9400) pumped by a Ti:Sapph regenerative amplifier (Coherent RegA 9000). The pulses are generated at a repetition rate of 250 kHz, and are wavelength-tunable from approximately 570 nm to 650 nm. Note that it is possible to generate pulses outside of this wavelength range with compromised bandwidth.

3.4 The Optical Response Function

Simply knowing that a FWM experiment samples $S^{(3)}$ is not useful. The real utility of such a measurement comes from relating $S^{(3)}$ to the microscopic dynamics of a studied material. To make this connection, we require a functional form for the optical response response function, which is derived in Appendix A:

$$S^{(3)}(\tau_2-\tau_1,\tau_3-\tau_2,t-\tau_3) = \left(-\frac{i}{\hbar}\right)^3 \mathrm{Tr}\left[\mu e^{-\frac{i}{\hbar}H_0(t-t_0)}[\mu_I(\tau_3),[\mu_I(\tau_2),[\mu_I(\tau_1,\rho(t_0)]]]e^{\frac{i}{\hbar}H_0(t-t_0)}\right] \tag{3.9}$$

From the three nested commutators involved, there are eight distinct terms that contribute to the third-order response function. To gain insight into their functional form, we focus on a single term:

$$\begin{aligned} S^{(3)}(\tau_2-\tau_1,\tau_3-\tau_2,t-\tau_3) &= \left(-\frac{i}{\hbar}\right)^3 \mathrm{Tr}\left[\mu e^{-\frac{i}{\hbar}H_0(t-t_0)}\mu_I(\tau_2)\rho(t_0)\mu_I(\tau_1)\mu_I(\tau_3)e^{\frac{i}{\hbar}H_0(t-t_0)}\right]+\ldots \\ &= \left(-\frac{i}{\hbar}\right)^3 \mathrm{Tr}\left[\mu_I(t)\mu_I(\tau_2)\rho(t_0)\mu_I(\tau_1)\mu_I(\tau_3)\right]+\ldots \end{aligned} \tag{3.10}$$

The argument of the trace operation may be intuitively thought of as propagation of the initial density matrix, and is most clearly illustrated for a two-level system composed of states $|0\rangle$ and $|1\rangle$ separated by an energy $E_1-E_0=\hbar\omega_{01}$. Assuming the initial density matrix $\rho(t_0)$ to be $|0\rangle\langle 0|$:

$$\rho(t_0)=|0\rangle\langle 0| = \begin{pmatrix} 1 & 0 \\ 0 & 0 \end{pmatrix} \tag{3.11}$$

and noting that the dipole operator is off-diagonal in the $\{|0\rangle, |1\rangle\}$ basis [14]:

$$\mu = \begin{pmatrix} 0 & \mu_{01} \\ \mu_{01} & 0 \end{pmatrix} \tag{3.12}$$

the action of the first dipole operator $\mu_I(\tau_1)$ is calculated explicitly to be:

$$\begin{aligned}
\rho(t_0)\mu_I(\tau_1) = & \\
& \begin{pmatrix} 1 & 0 \\ 0 & 0 \end{pmatrix} \begin{pmatrix} e^{\frac{i}{\hbar}E_0(\tau_1-t_0)} & 0 \\ 0 & e^{\frac{i}{\hbar}E_1(\tau_1-t_0)} \end{pmatrix} \begin{pmatrix} 0 & \mu_{01} \\ \mu_{01} & 0 \end{pmatrix} \begin{pmatrix} e^{-\frac{i}{\hbar}E_0(\tau_1-t_0)} & 0 \\ 0 & e^{-\frac{i}{\hbar}E_1(\tau_1-t_0)} \end{pmatrix} \\
& = \begin{pmatrix} 0 & e^{i\omega_{01}(\tau_1-t_0)}\mu_{01} \\ 0 & 0 \end{pmatrix}
\end{aligned}$$

Adding the additional terms while preserving the operator ordering:

$$\begin{aligned}
\mu_I(\tau_2)\rho(t_0)\mu_I(\tau_1) &= \begin{pmatrix} 0 & 0 \\ 0 & \mu_{01}e^{i\omega_{01}(\tau_2-\tau_1)}\mu_{01} \end{pmatrix} \\
\mu_I(\tau_2)\rho(t_0)\mu_I(\tau_1)\mu_I(\tau_3) &= \begin{pmatrix} 0 & 0 \\ \mu_{01}e^{i\omega_{01}(\tau_3-t_0)}\mu_{01}e^{i\omega_{01}(\tau_2-\tau_1)}\mu_{01} & 0 \end{pmatrix} \\
\mu_I(t)\mu_I(\tau_2)\rho(t_0)\mu_I(\tau_1)\mu_I(\tau_3) &= \begin{pmatrix} \mu_{01}e^{-i\omega_{01}(t-\tau_3)}\mu_{01}e^{i\omega_{01}(\tau_2-\tau_1)}\mu_{01}\mu_{01} & 0 \\ 0 & 0 \end{pmatrix}
\end{aligned} \tag{3.13}$$

In words, the first dipole operator $\mu_I(\tau_1)$ converts the initial ground state on-diagonal element (called a **population**) into an off-diagonal element (called a **coherence**). The next dipole operator $\mu_I(\tau_2)$ converts this coherence into an excited state population, which is then converted back into a coherence by $\mu_I(\tau_3)$ and finally back into a ground state population $\mu_I(t)$. We can represent this sequence diagrammatically as shown in Fig. 3.6:

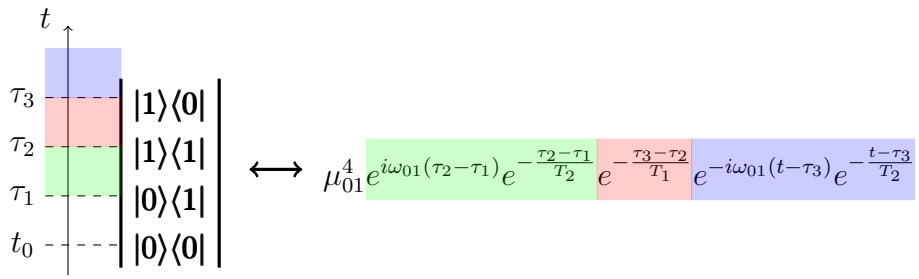

Figure 3.6: Example double-sided Feynman diagram (left) and the equation it represents (right). The colored boxes indicate each time delay and its respective component in the equation.

Diagrams in Fig. 3.6, called **double-sided Feynman diagrams**, provide an intuitive interpretation of the various terms that compose the third-order optical response and their functional form. First, there are four dipole moment terms μ_{01} that correspond to the action of the three pulses at times $\{\tau_1, \tau_2, \tau_3\}$ plus the emission of a FWM signal at time t. The two oscillatory terms $e^{i\omega_{01}(\tau_2-\tau_1)}$ and $e^{-i\omega_{01}(t-\tau_3)}$ reflect the evolutions of the coherences $|0\rangle\langle 1|$ and $|1\rangle\langle 0|$ respectively. Lastly, we have added in Fig. 3.6 the dephasing terms $e^{-\frac{\tau_2-\tau_1}{T_2}}$ and $e^{-\frac{t-\tau_3}{T_2}}$ and population relaxation term $e^{-\frac{\tau_3-\tau_2}{T_1}}$ in by hand. These phenomenological terms are justified in Section 3.5 and Appendix B.

3.4.1 Double-Sided Feynman Diagrams

The above discussion frames double-sided Feynman diagrams as a visual aid for interpreting various terms of the optical response function. Conversely, we may also write down a complete optical response function simply from a given diagram. The usefulness in doing so becomes apparent if we know a-priori every relevant diagram that contributes to the nonlinear response that we measure. Here we outline a systematic procedure to generate all such diagrams, which is described in further detail elsewhere [14, 15].

First recall the collection wavevector $\mathbf{k} = -\mathbf{k}_\mathrm{A} + \mathbf{k}_\mathrm{B} + \mathbf{k}_\mathrm{C}$, where pulse A is said to be **conjugated** due to its negative phase-matching wavevector. We then follow the

rules below to generate all relevant diagrams:

1. The interaction of each pulse is represented by an arrow that points (rightward)leftward for a (non-)conjugate pulse.

2. An arrow pointing (out)inwards represents an (de-)excitation of the bra or ket, depending on the side of the arrow.

3. A fourth dashed arrow is drawn pointing leftward to represent emission of the third-order signal. The following element must be a population state $|n\rangle\langle n|$.

For the two-level system described in this section, two diagrams are possible (according to the above rules and pulse ordering $A \rightarrow B \rightarrow C$) and are shown in Fig. 3.7:

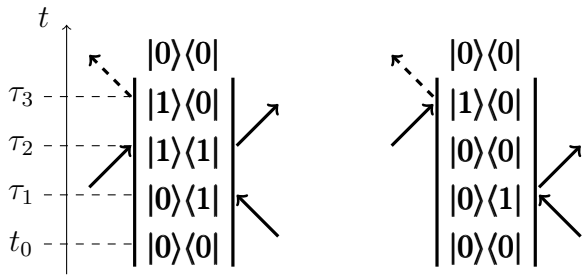

Figure 3.7: The two diagrams that survive the rotating wave approximation and contribute to the $\mathbf{k} = -\mathbf{k}_A + \mathbf{k}_B + \mathbf{k}_C$ FWM signal.

The sequential changes of the density matrix in each diagram are collectively termed either **quantum pathways** or **Liouville pathways**. In Fig. 3.7, the left diagram traversing an intermediate excited state population $|1\rangle\langle 1|$ is called a **stimulated-emission** pathway while the right diagram with an intermediate ground state population $|0\rangle\langle 0|$ is called a **ground-state bleach** pathway. We note that in the presence of a higher-lying doubly-excited state, an additional **excited-state absorption** pathway becomes possible. Additional terms generated by the nested commutator in Equation (3.9) that are not allowed by the diagram rules are negligible in the rotating wave approximation [14, 15].

3.4.2 Quantum Pathways and Multi-Dimensional Spectra

The second, third, and fourth density matrix elements in each diagram dictate the position at which its response will appear on a multi-dimensional spectrum. Taking the left diagram in Fig. 3.7 for example, the second coherence $|0\rangle\langle 1|$ will oscillate at a frequency $\omega_0 - \omega_1 = -\omega_{01}$ which corresponds to an absorption axis position $\hbar\omega_\tau = -\hbar\omega_{01}$. Likewise, the third population $|1\rangle\langle 1|$ oscillates at $\omega_1 - \omega_1 = 0$ which corresponds to a mixing axis position $\hbar\omega_T = 0$ and the fourth coherence $|1\rangle\langle 0|$ oscillates at $\omega_1 - \omega_0 = \omega_{01}$ which corresponds to an emission axis position $\hbar\omega_t = \hbar\omega_{01}$.

To demonstrate the utility of double-sided Feynman diagrams towards interpreting multi-dimensional spectra, consider the more complicated V level system shown in Fig. 3.8a. The excited states $|1\rangle$ and $|2\rangle$ are connected by dipole-allowed transitions to a common ground state $|0\rangle$, and we thus say that the two states $|1\rangle$ and $|2\rangle$ are **coherently coupled**. Figs. 3.8b-i then show the eight possible diagrams for this system:

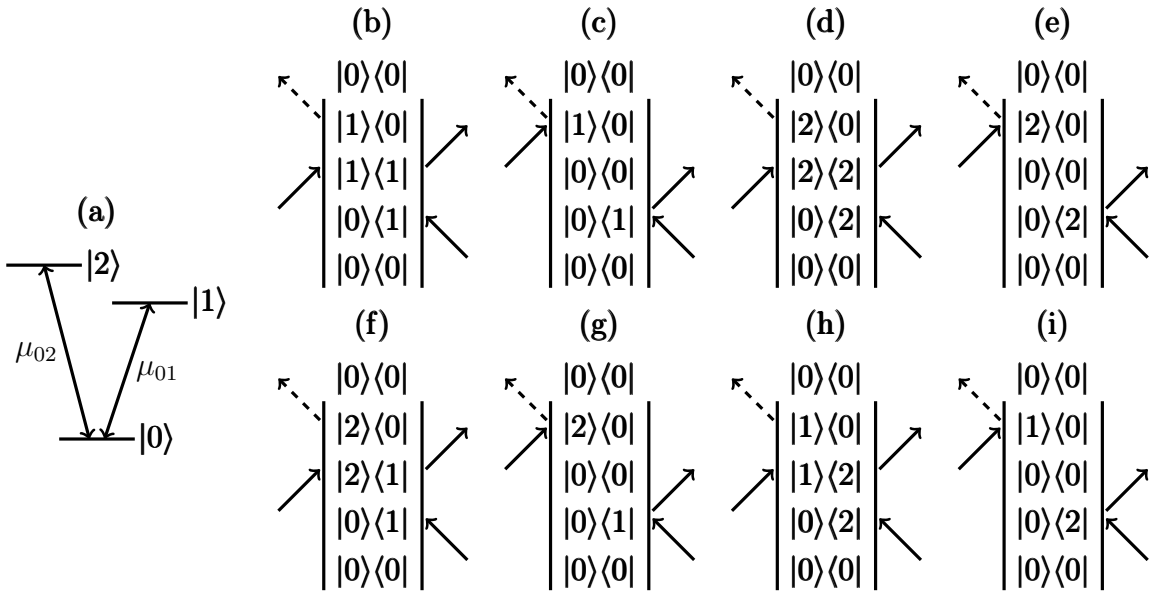

Figure 3.8: (a) V level system with a single ground state $|0\rangle$ and two excited states $|1\rangle$ and $|2\rangle$ as indicated. (b-e) Diagrams representing quantum pathways with absorption and emission from identical transitions. (f-i) Diagrams representing quantum pathways with absorption and emission from different transitions.

One can see that in addition to quantum pathways corresponding to absorption and emission from identical transitions (Fig. 3.8b-e), there are also quantum pathways corresponding to absorption and emission from different transitions (Fig. 3.8f-i). Quantum pathways arising from coherent coupling between two states and those arising from single transitions are indistinguishable in most spectroscopy experiments, but are naturally separated in a multi-dimensional spectrum.

For equal transition dipole moments μ_{01} and μ_{02}, the resultant one-quantum and zero-quantum 2-D spectra of the V level system in Fig. 3.8a are plotted in Fig. 3.9:

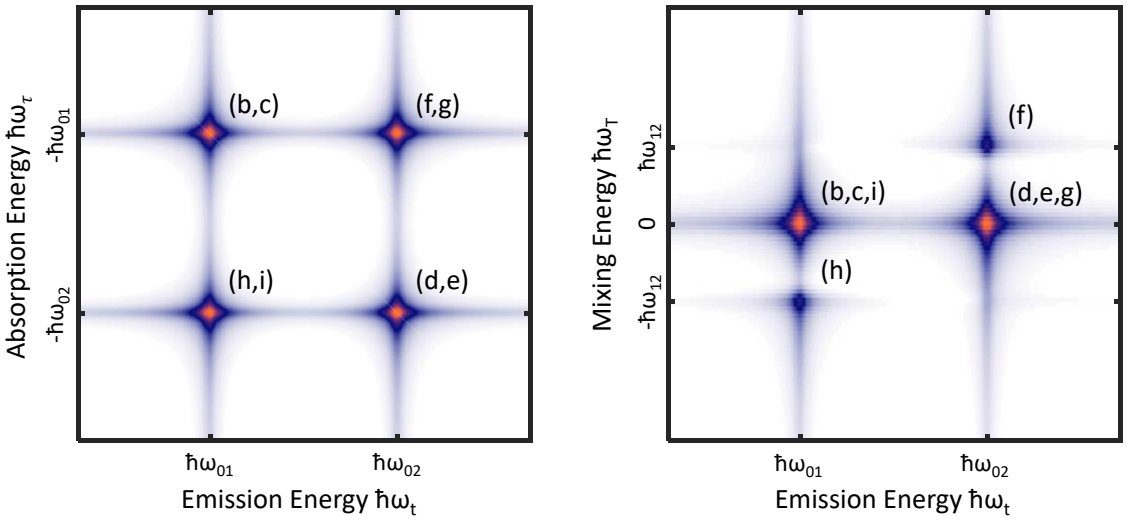

Figure 3.9: One-quantum (left) and zero-quantum (right) 2-D spectra of the V level system in Fig. 3.8a. The letters next to each peak indicate the diagrams in Fig. 3.8b-i corresponding to their underlying quantum pathways.

The direct correspondence between peaks of the 2-D spectra in Fig. 3.9 and specific quantum pathways in Fig. 3.8 illustrates a powerful use of double-sided Feynman diagrams. By generating all possible diagrams for a given electronic system one may assign physical meaning to peaks in a multi-dimensional spectrum in terms of allowed quantum pathways, and even predict a-priori the appearance of multi-dimensional spectra.

3.5 Multi-Dimensional Spectra of CNCs

MDCS of CNCs may, at the most basic level, be understood in terms of transitions between discrete energy levels in either the strong or weak confinement regime. However, examination of experimental multi-dimensional spectra of CNCs reveals many features that point to much more intricate underlying dynamics such as strongly non-Lorentzian lineshapes and sidebands positioned at energy-splittings which do not correspond to that of any electronic energy levels. Most of these features arise from electron-phonon coupling, which is simply the mutual interaction of electronic excitations with the nuclear motion of their host lattice. A general Hamiltonian for a system with two electronic states $|g\rangle$ and $|e\rangle$, representing the ground and excited state respectively, which are coupled to nuclear degrees of freedom $\mathbf{q}$ is the following:

$$\begin{aligned} H &= |g\rangle \left[T(\mathbf{q}) + W_g(\mathbf{q})\right] \langle g| + |e\rangle \left[\hbar\omega_{eg}^0 + T(\mathbf{q}) + W_e(\mathbf{q})\right] \langle e| \\ &= |g\rangle H_g(\mathbf{q}) \langle g| + |e\rangle H_e(\mathbf{q}) \langle e| \end{aligned} \tag{3.14}$$

where $T(\mathbf{q})$ is the nuclear kinetic energy, $W_g(\mathbf{q})$ and $W_e(\mathbf{q})$ are the ground and excited state adiabatic potentials for each electronic state (i.e. the dependence of the electronic energy on the nuclear configuration), and $\hbar\omega_{eg}^0$ is the energy gap in the absence of coupling to nuclear motion. To derive equations of motion for electronic dynamics that incorporate nuclear motion is not trivial. We defer derivation of such equations to Appendix B and more thorough references [15, 24], and state here only the results.

As shown above, the optical response for a single resonance involving two electronic states $|g\rangle$ and $|e\rangle$ separated by a thermally-averaged energy-gap $\overline{\hbar\omega_{eg}}$ is composed of two components:

$$R^{(3)}(\tau, T, t) = R_{ESE}^{(3)} + R_{GSB}^{(3)} + \text{c.c.} \tag{3.15}$$

where $R^{(3)}_{ESE}$ and $R^{(3)}_{GSB}$ are the "excited-state emission" and "ground-state bleach" pathways respectively. General expressions for these two terms that incorporate coupling to nuclear motion are the following:

$$R^{(3)}_{ESE}(\tau,T,t) \propto e^{i\overline{\omega_{eg}}\tau - i\overline{\omega_{eg}}t} e^{-g^*(t)-g^*(\tau)+g^*(T)-g^*(T+t)-g(\tau+T)+g(\tau+T+t)} \tag{3.16}$$

$$R^{(3)}_{GSB}(\tau,T,t) \propto e^{i\overline{\omega_{eg}}\tau - i\overline{\omega_{eg}}t} e^{-g(t)-g^*(\tau)+g(T)-g(T+t)-g(\tau+T)+g(\tau+T+t)} \tag{3.17}$$

which are the rephasing components of the optical response that emit into the phase-matched direction $\mathbf{k}$ = -$\mathbf{k}_{\mathrm{A}}$ + $\mathbf{k}_{\mathrm{B}}$ + $\mathbf{k}_{\mathrm{C}}$. As its name suggests, the **dephasing lineshape** $g(t)$ characterizes the irreversible dephasing of coherences induced by interactions with an environment. The specific functional form of $g(t)$ depends on the specific material system and temperature, but in the so-called **Markovian limit** simplifies to:

$$g(t) = \gamma t = \frac{t}{T_2} \qquad \text{(Markovian Limit)} \tag{3.18}$$

which is a common approximation that the energy-gap fluctuations induced by the environment are uncorrelated (i.e. memory-less). It is simple to recover the phenomenological equation in Fig. 3.6 by plugging equation (3.18) into equation (3.16). In the time-domain these coherences dephase exponentially in the Markovian limit while their corresponding peaks in a linear or multi-dimensional spectrum are ideal Lorentzians. The work presented in the next two chapters focuses on a system, colloidal CdSe nanocrystals, which exhibits electronic dynamics that strongly violate the Markovian approximation.

References

(1) Jeener, J.; Alewaeters, G. *Progress in Nuclear Magnetic Resonance Spectroscopy* **2016**, *94-95*, 75–80.

(2) Aue, W. P.; Bartholdi, E.; Ernst, R. R. *The Journal of Chemical Physics* **1976**, *64*, 2229–2246.

(3) Jeener, J.; Meier, B. H.; Bachmann, P.; Ernst, R. R. *The Journal of Chemical Physics* **1979**, *71*, 4546–4553.

(4) Tanimura, Y.; Mukamel, S. *The Journal of Chemical Physics* **1993**, *99*, 9496–9511.

(5) Hybl, J. D.; Albrecht, A. W.; Faeder, S. M. G.; Jonas, D. M. *Chemical Physics Letters* **1998**, *297*, 307–313.

(6) Hamm, P.; Lim, M.; DeGrado, W. F.; Hochstrasser, R. M. *Proceedings of the National Academy of Sciences* **1999**, *96*, 2036–2041.

(7) Zhang, T.; Borca, C. N.; Li, X.; Cundiff, S. T. *Opt. Express* **2005**, *13*, 7432–7441.

(8) Borca, C. N.; Zhang, T.; Li, X.; Cundiff, S. T. *Chemical Physics Letters* **2005**, *416*, 311–315.

(9) Yang, L.; Zhang, T.; Bristow, A. D.; Cundiff, S. T.; Mukamel, S. *The Journal of Chemical Physics* **2008**, *129*, 234711.

(10) Kim, J.; Mukamel, S.; Scholes, G. D. *Accounts of Chemical Research* **2009**, *42*, PMID: 19552412, 1375–1384.

(11) Park, K.; Cho, M. *The Journal of Chemical Physics* **2000**, *112*, 5021–5036.

(12) Ding, F.; Zanni, M. T. *Chemical Physics* **2007**, *341*, Ultrafast Dynamics of Molecules in the Condensed Phase: Photon Echoes and Coupled Excitations, 95–105.

(13) Turner, D. B.; Stone, K. W.; Gundogdu, K.; Nelson, K. A. *The Journal of Chemical Physics* **2009**, *131*, 144510.

(14) Hamm, P.; Zanni, M., *Concepts and Methods of 2D Infrared Spectroscopy*, 1st ed.; Cambridge University Press: 2011.

(15) Mukamel, S., *Principles of Nonlinear Optical Spectroscopy*, 1st ed.; Oxford University Press: 1999.

(16) Marshall, A. G.; Verdun, F. R., *Fourier Transforms in NMR, Optical, and Mass Spectrometry: A User's Handbook*, 1st ed.; Elsevier Science: 1989.

(17) Eckbreth, A. C. *Applied Physics Letters* **1978**, *32*, 421–423.

(18) Nardin, G.; Autry, T. M.; Silverman, K. L.; Cundiff, S. T. *Opt. Express* **2013**, *21*, 28617–28627.

(19) Lomsadze, B.; Cundiff, S. T. *Science* **2017**, *357*, 1389.

(20) Martin, E. W.; Cundiff, S. T. *Physical Review B* **2018**, *97*, 081301.

(21) Lepetit, L.; Chériaux, G.; Joffre, M. *Journal of the Optical Society of America B* **1995**, *12*, 2467–2474.

(22) Fuller, F. D.; Ogilvie, J. P. *Annual Review of Physical Chemistry* **2015**, *66*, 667–690.

(23) Bristow, A. D.; Karaiskaj, D.; Dai, X.; Zhang, T.; Carlsson, C.; Hagen, K. R.; Jimenez, R.; Cundiff, S. T. *Review of Scientific Instruments* **2009**, *80*, 073108.

(24) May, V.; Kuhn, O., *Charge and Energy Transfer Dynamics in Molecular Systems*, 3rd ed.; Wiley-VCH: 2011.

CHAPTER IV

CdSe CNCs: Acoustic Phonon Coupling

4.1 Acoustic Phonon Coupling in CNCs

In general, one of the most important phenomena that impact quantum dot optoelectronics is electron-phonon coupling. Interactions between electronic excitations and lattice vibrations facilitate energy loss through non-radiative decay processes and play a vital role in coherent control protocols [1–3]. Acoustic vibrational modes are of particular importance, since their low energies mediate coupling between the fine-structure of an exciton manifold [4, 5] and comprise the primary dephasing mechanism of interband coherences [6, 7] in quantum dots. Though usually a continuum of modes, acoustic vibrations can assume discrete modes [8, 9] due to size-confinement in colloidal quantum dots [10, 11]. However, the two pictures of acoustic vibrations as a bulk-like phonon continuum or discrete spherical harmonics are seldom considered simultaneously.

Vibrational coupling to excitons in quantum dots has been studied extensively, but most spectroscopic studies have utilized linear techniques such as absorption and photoluminescence [12–15]. Linear spectroscopies encounter two main obstacles. First, ensembles of all types of quantum dots exhibit inhomogeneous broadening (due to dot size dispersion) of their absorption and emission profiles. Linear techniques only provide the inhomogeneous lineshape of a quantum dot ensemble that reflects its size distribution, and are largely insensitive to its microscopic dynamics. Second, single quantum dot spectroscopy studies that circumvent inhomogeneous broadening have inherent limitations such as time-resolution and dot-to-dot structural variations. These limitations have restricted the focus of most experimental studies to properties of discrete vibrational modes, since signatures of continuum mode coupling are generally weak. Studies that do observe continuum modes are heavily influenced by spectral diffusion at timescales shorter than the integration time [16], and vary greatly between dots [14].

As described in Chapter III, a technique capable of extracting the homogeneous response of an inhomogeneously broadened ensemble is MDCS [17]. MDCS has recently been applied to a variety of quantum dot systems, including interfacial [18], self-assembled [19, 20], and colloidal [21–23] dots, to reveal physics normally obscured by inhomogeneous broadening and/or single-dot experiment limitations. MDCS is ideal to investigate acoustic phonon coupling in CNCs for two main reasons. First, the ensemble-averaged homogeneous response may be retrieved in the presence of inhomogeneity as a function of resonance energy (corresponding to radius in CNCs). Second, vibrational lineshapes are enhanced by nonlinear spectroscopies such as MDCS.

4.2 Sample and Experiment

As the first type of nanocrystal to be synthesized and studied, CdSe CNCs are the most studied and well-characterized colloidal material platform. For this reason,

CdSe CNCs remain an important test bench for studying the numerous aspects of colloidal nanocrystals that are still not understood.

The sample is CNCs composed of a 2 nm mean radius CdSe core and 2.5 nm mean thickness CdZnS shell (shown in Fig. 4.1a), whose synthesis is detailed elsewhere [24]. To study their properties at cryogenic temperatures the CNCs are dispersed in heptamethylnonane, which forms a transparent glass at temperatures below 100 K and is liquid up to room temperature. The colloidal suspension is diluted to an optical density of 0.3 at the room-temperature 1S exciton absorption peak.

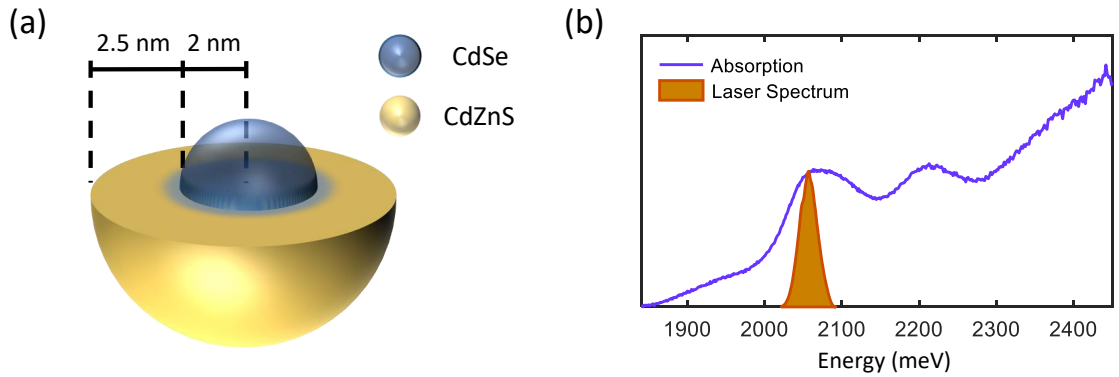

Figure 4.1: (a) Schematic of the CdSe/CdZnS core/shell CNCs. (b) The ensemble sample absorption plotted with the excitation laser spectrum, which is centered on the 1S exciton absorption peak.

To perform MDCS, we use a Multi-Dimensional Optical Nonlinear Spectrometer (MONSTR) [25]. An excitation intensity of 4 W/cm^2 generates a predominately third-order response as verified by the power-dependence of the heterodyned signal. All pulses are co-linearly polarized and centered at wavelength 605 nm. The laser spectrum is compared to the sample absorption spectrum in Fig. 4.1b.

4.3 Low-Energy Vibrations in CNCs

In solids, low-energy acoustic vibrations that assume a continuum of energies modulate the transition energies of resonances. This constitutes the classic problem

of a discrete level system coupled to a heat bath. The finite size of the CNC geometry then introduces discrete vibrations [8, 9]. These vibrations may be separated into the two classes of acoustic and torsional modes, which have longitudinal and transverse character respectively. However, acoustic modes of CNCs embedded in a matrix depend crucially on the difference in longitudinal sound velocities of the CNC and matrix. For a large sound velocity mismatch, confined acoustic modes are sustained by reflections at the CNC surface [11].

In our case we were unable to find values for the low-temperature (glass phase) sound velocity for heptamethylnonane, though from its room temperature (liquid phase) speed [26] 1.285×10^5 cm/s it is plausible that in solid form its longitudinal sound velocity may increase three- to four-fold and become comparable to the CNC longitudinal sound velocity. This small sound velocity mismatch [27] gives rise to an acoustic continuum characteristic of delocalized vibrations in bulk materials [28], since boundary conditions at the CNC surface may be modified such that vibrations of the combined matrix and embedded sphere must be jointly considered. Crucially, transverse torsional modes involving no radial displacement into the surrounding matrix are simultaneously supported by the dot geometry.

4.4 One-Quantum Spectra (Temperature Dependence)

Absolute-value one-quantum spectra are shown in the top row of Fig. 4.2 and have three main features. First, a narrow zero-phonon line is present along the diagonal, which corresponds to absorption and emission at the same energy. Second, a prominent broad pedestal around the zero-phonon line [29, 30], which has the characteristic lineshape of localized excitons coupling to an acoustic phonon continuum bath [13, 31], grows with increasing temperature. At these low temperatures, the pedestal is asymmetric due to higher probability of emission than absorption of vibrational energy. Third, the acoustic phonon pedestal features two peaks next to the zero-phonon

line (seen more clearly in Fig. 4.5). Although the zero-frequency cutoff of the spectral density may result in a sharp feature on the Stokes-side ($\hbar\omega_t - \hbar\omega_\tau < 0$) of the zero-phonon line, we cannot explain the anti-Stokes ($\hbar\omega_t - \hbar\omega_\tau > 0$) peak through solely an acoustic phonon continuum.

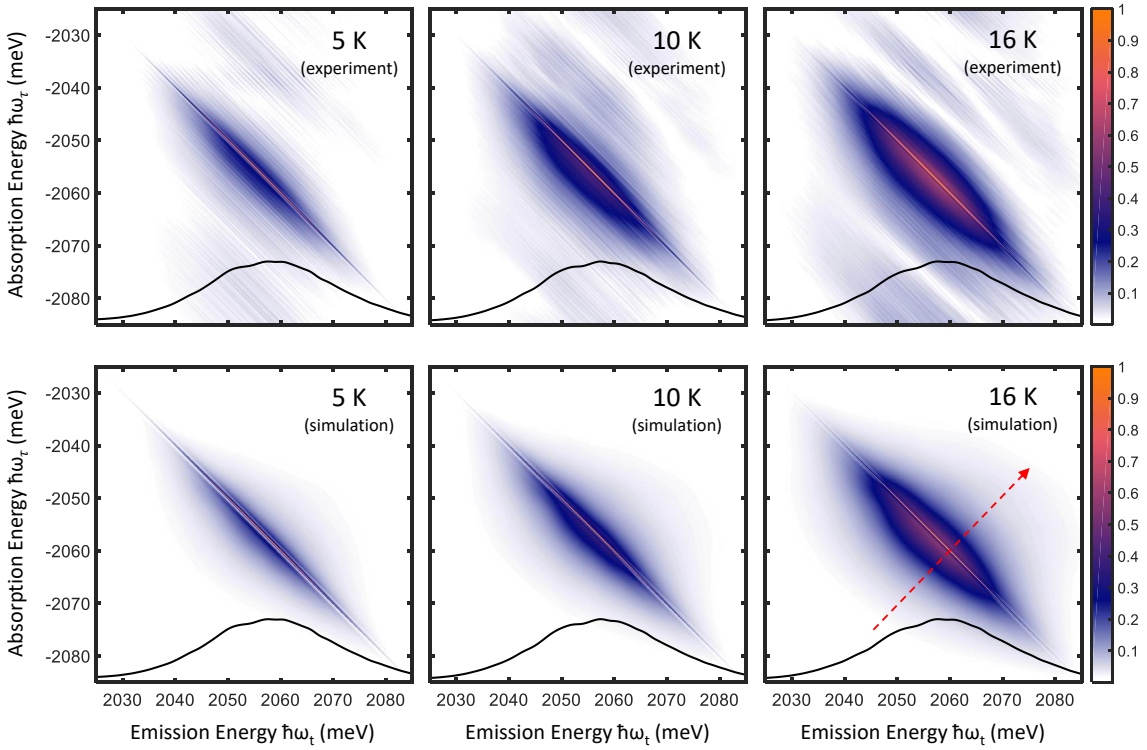

Figure 4.2: Experimental (top row) and simulated (bottom row) absolute-value one-quantum spectra at temperatures 5, 10, and 16 K. All spectra are taken at waiting time $T = 1$ ps. The solid black curves represent the spectra of the excitation and local oscillator pulses for each temperature. A red dashed arrow in the bottom right panel indicates the location of the slices shown in Fig. 4.5.

4.5 Simulation

As described above, coupling to a delocalized acoustic phonon continuum alone cannot describe all features observed in our one-quantum spectra. We thus simulate the acquired one-quantum spectra according to a model that simultaneously incorporates both confined and delocalized vibrational modes. The simulated spectra are shown in the bottom row of Fig. 4.2 and the model is shown schematically in Fig. 4.3.

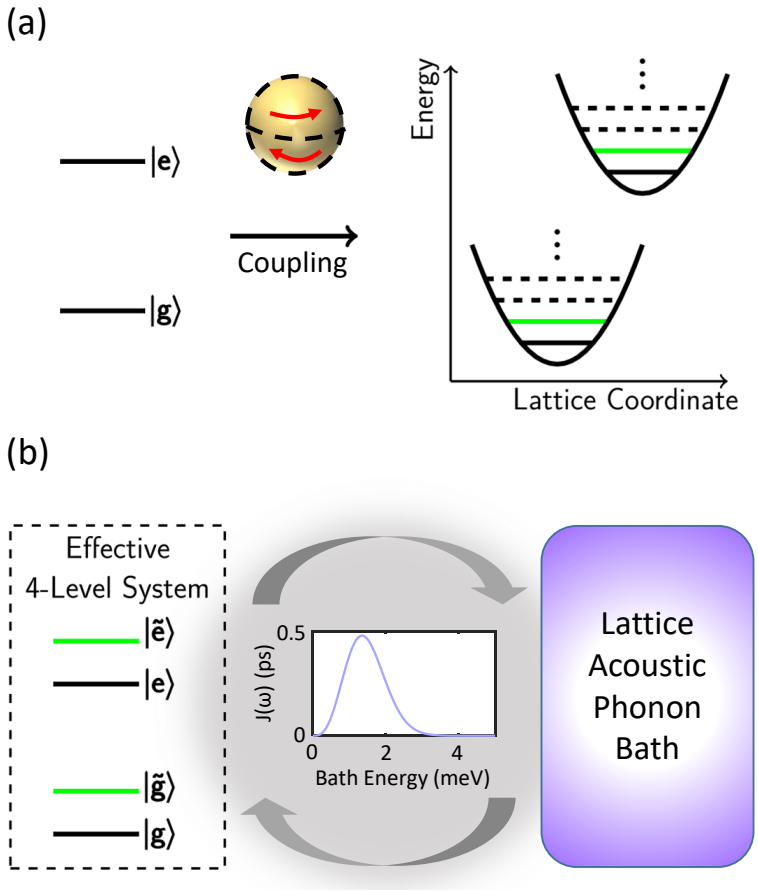

Figure 4.3: (a) Dressing of the ground and excited exciton states by the $(\ell, n) = (2, 0)$ torsional mode results in ladders of states separated by the (2,0) mode energy. (b) The simplified 4-level system formed from the lowest two states of the ground and excited state ladders then couple to a harmonic bath of acoustic phonon continuum states. The coupling strength is characterized by the spectral density function $J(\omega)$, and the $J(\omega)$ used in the simulations below is plotted inset.

A discrete transverse torsional mode "dresses" the ground and excited electronic states to generate ladders of states separated by the torsional mode energy [32] (shown in Fig. 4.3a). By calculating allowed torsional mode energies (indexed by ℓ and n) according to our material parameters (shown in Fig. 4.4), we find that the $(\ell, n) = (2, 0)$ mode matches the features of our experimental spectra. We note that the higher-frequency $(\ell, n) = (1, 0)$ mode, which involves oscillations of a core and shell layer in opposite directions, should couple weakly to excitons in the type-I CdSe/CdZnS CNCs studied here that confine both carriers in the CdSe core [24].

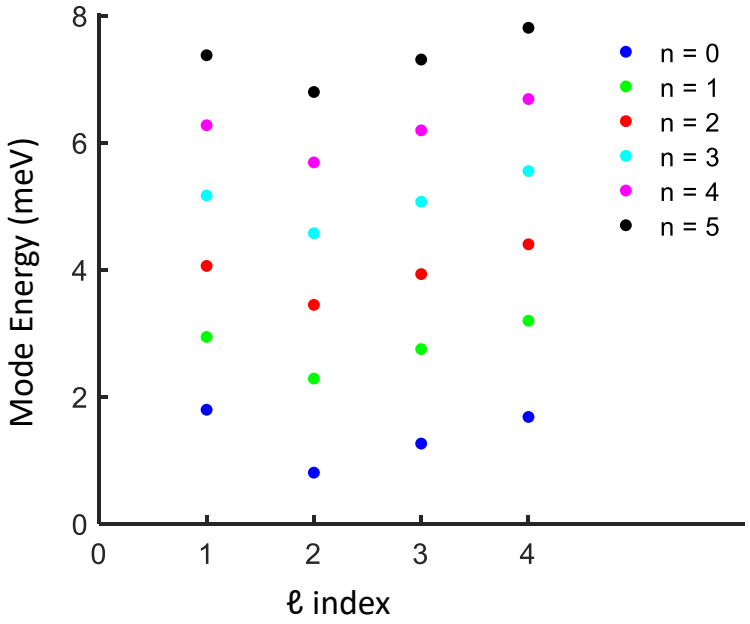

Figure 4.4: Energies of allowed torsional confined acoustic modes at different indices ℓ and n are denoted by the colored dots as indicated.

The transition strengths between these states are determined by the Huang-Rhys parameter S [33]. The energies of these states are then modulated by a continuum bath of longitudinal acoustic phonons via elastic interactions. Assuming the bath is harmonic, that is the coupling is taken to be linear coupling to a continuous distribution of harmonic oscillators, each transition may be modeled by the following Hamiltonian:

$$H = |e\rangle\langle e|\,\hbar\omega_0 + \sum_\alpha \hbar\omega_\alpha a_\alpha^\dagger a_\alpha + |e\rangle\langle e| \sum_\alpha \lambda_\alpha \left(a_\alpha^\dagger + a_\alpha\right) \tag{4.1}$$

where $\hbar\omega_0$ is the transition energy, $a_\alpha^{(\dagger)}$ are the creation/annihilation operators for phonon mode α, and λ_α is the electron-phonon coupling strength for mode α. In order, each term represents the energy of the electronic excitation, the energy of the thermal bath, and the electron-phonon coupling respectively. This Hamiltonian formally resembles the "spin-boson Hamiltonian" [34] and may be solved by identical

techniques [35]. Namely, we can characterize the system-bath interaction by a spectral density function $J(\omega)$ (shown in Fig. 4.3). The spectral density may be loosely interpreted as the frequency spectrum of the energy gap modulation by a coupled harmonic bath. For a spherical nanocrystal with identical electron and hole localization radii (which is the case for Type-I CNCs in the strong confinement regime [36]), the spectral density of an acoustic phonon bath

$$J_a(\omega) = A\omega^p e^{-\omega^2/\omega_c^2} \tag{4.2}$$

may be derived analytically [37], where A characterizes the coupling strength, ω_c is a cutoff frequency that determines the width of acoustic phonon spectral features, and p is an integer that depends on the coupling mechanism ($p = (1)3$ for (deformation potential) piezoelectric coupling) [35]. In one-quantum spectra A, ω_c, and p determine the relative amplitude, width, and steepness of the central pedestal feature respectively, and serve as orthogonal parameters that uniquely determine the size and shape of the pedestal. The relation between the spectral density and the lineshape function $g(t)$ is derived in Appendix B:

$$g(t) = \frac{1}{2\pi}\int_{-\infty}^{\infty}[1-\cos(\omega t)]\coth(\beta\hbar\omega/2)J_a(\omega)d\omega + \frac{i}{2\pi}\int_{-\infty}^{\infty}[\sin(\omega t)-\omega t]J_a(\omega)d\omega \tag{4.3}$$

which determines the dephasing dynamics according to equations (3.16) and (3.17).

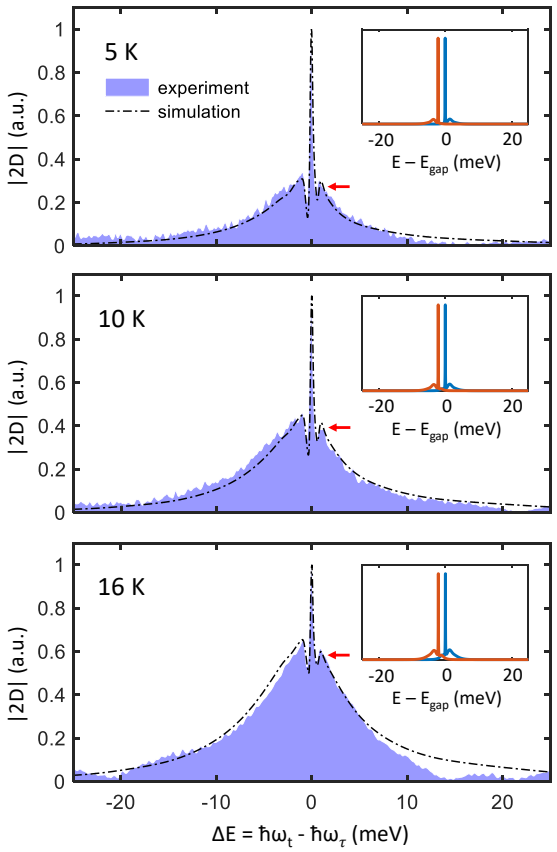

Figure 4.5: Cross-diagonal slices of the experimental (solid purple curve) and simulated (black line) absolute-value single-quantum spectra in Fig. 4.2, in which the slice locations are indicated by a red dashed arrow. The corresponding simulated absorption (blue) and fluorescence (orange) lineshapes are plotted inset as a function of detuning from the thermally averaged ground state electronic energy gap E_{gap}.

To compare experiment and simulation more closely, we plot cross-diagonal slices centered at energy $|\hbar\omega_\tau| = |\hbar\omega_t| = 2060$ meV in Fig. 4.5. Comparison of the single-quantum spectrum slices with the simulated absorption and fluorescence lineshapes plotted inset contrasts the difference in strength (relative to the zero-phonon line) between linear and third-order vibrational lineshapes. The enhancement of vibrational lineshapes in the third-order response is due to additional terms involving the dephasing lineshape function which are absent in the linear response. The nonlinear response of a system may therefore reveal vibrational couplings that are otherwise too weak to observe via linear spectroscopies.

4.5.1 Parameters

For the model described above, analytic expressions are not available to fit experimental lineshapes. We thus emphasize that the goal of our simulations is not to extract numerical values for specific quantities, but rather to elucidate the nature of the underlying microscopic dynamics. The torsional mode energy $E_{(2,0)}$ is calculated [8], while accounting for the core-shell structure of our dots (see Fig. 4.4 and [38]), to be 0.8 meV, and is the value used in our simulation. The torsional mode Huang-Rhys parameter used is $S = 0.6$. We were unable to obtain good agreement between experiment and simulation for deformation potential coupling ($p = 1$) with the continuum acoustic modes. Although excitons in free-standing few-nm radii CNCs are thought to couple to acoustic vibrations predominately via the deformation potential mechanism [8], this suggests that the delocalized acoustic vibrations considered here couple through the long-range piezoelectric interaction ($p = 3$) used in our simulation. Coherences between states $|g\rangle$ and $|e\rangle$ are simulated with a dephasing rate $\hbar\gamma = 0.4$ meV to match the zero-phonon linewidth while coherences involving the vibrationally-excited states $|\tilde{g}\rangle$ and $|\tilde{e}\rangle$ dephase more quickly at $\hbar\gamma = 1.6$ meV. The remaining parameters used are $A = 0.47$ ps^4 and $\hbar\omega_c = 1.15$ meV.

4.5.2 Finite Pulse Bandwidth Effects

Although idealized MDCS experiments that use vanishingly short pulses of infinite bandwidth would probe the entire third-order response function of a material, real experiments are limited to pulses of finite pulse duration and bandwidth. The most obvious effect of finite bandwidth is that only the optical response lying within the laser spectrum is probed. It is therefore important to account for this and any other distortions due to finite pulse bandwidth. The most convenient way to do so is in the

frequency domain [39]:

$$S^{(3)}(\omega_\tau, \omega_T, \omega_t) \propto R^{(3)}(\omega_\tau, \omega_T, \omega_t) E_1(\omega_\tau) E_2(\omega_T - \omega_\tau) E_3(\omega_t - \omega_T) \tag{4.4}$$

The simulated spectra in Fig. 4.2 are thus obtained after numerically including finite pulse bandwidth effects for a large inhomogeneously broadened ($\sigma = 50$ meV) response function by using the respective experimental laser spectrum at each temperature:

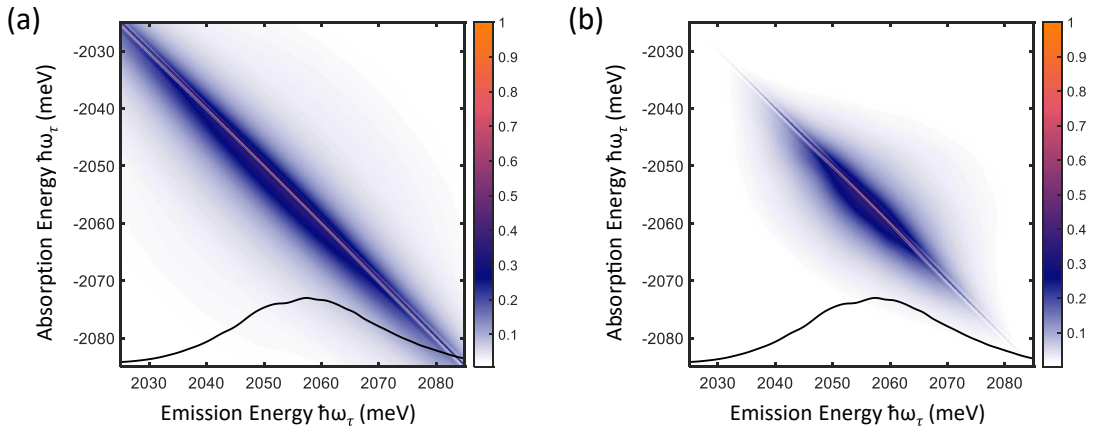

Figure 4.6: (a) Simulated one-quantum spectrum with large inhomogeneous broadening that represents the full nanocrystal size distribution. (b) Simulated one-quantum spectrum after applying finite pulse bandwidth effects to the spectrum in (a).

4.5.3 Many-Body Effects

In higher-dimensional semiconductor nanostructures, many-body effects have been found to manifest in multi-dimensional spectra [40, 41]. It is therefore important to characterize their role in our measurements. First, the effects of Coulomb correlation that gives rise to the excitonic states probed in our experiment are primarily characterized by a correlation energy that changes the energy gap [42] and do not modify the spectral density functional form [35] given by equation (4.2).

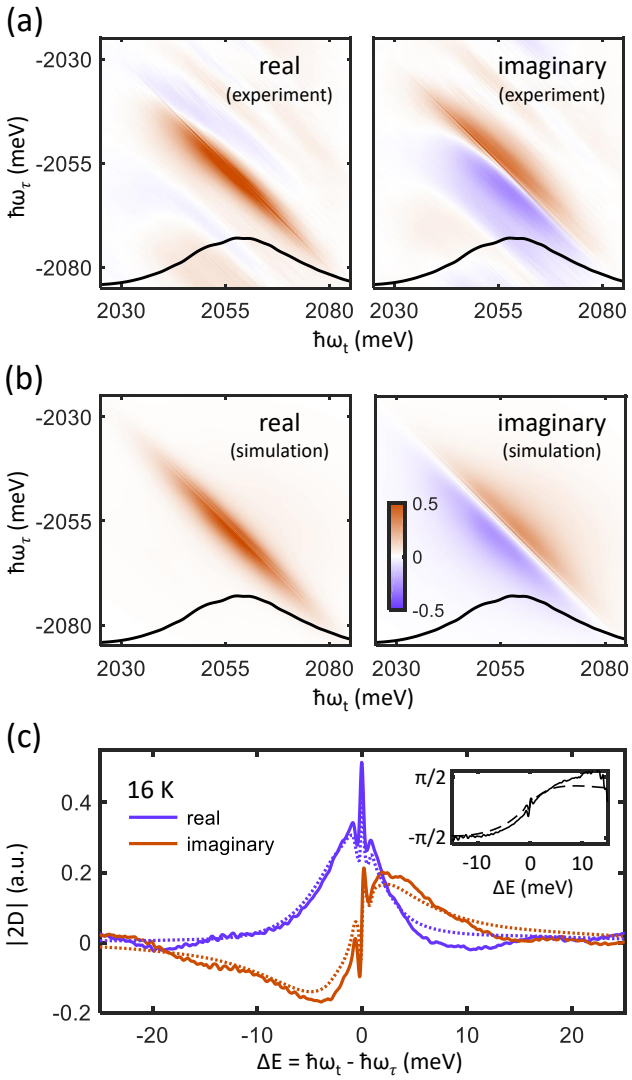

Figure 4.7: (a) Experimental and (b) simulated single-quantum spectrum quadratures at 16 K. The experimental spectrum is phased by maximizing the real-quadrature zero-phonon line. (c) Cross-diagonal slices of the experimental (solid lines) and simulated (dotted lines) single-quantum spectrum quadratures at 16 K. Inset shows the corresponding phase across the slice. The slice location is the same as indicated by the red dashed arrow in Fig. 4.2.

In terms of higher-order correlation effects, we neglect in our simulations excited state absorption (ESA) pathways [20, 43] that involve doubly-excited states with a binding energy Δ_{XX}. Previous studies have determined Δ_{XX} to be tens of meV [23, 44] and beyond our laser bandwidth, so we do not expect these pathways to contribute to our single-quantum spectra. Our experimental parameters also correspond

to less than 0.2 excitons per nanocrystal [38], which precludes significant nonlinear signals arising from excited initial states. Nevertheless, we verify this assumption by examining the quadratures of the complex spectrum at 16 K plotted in Fig. 4.7a. Although the overall phase was not retrieved in our experiment, the complex single-quantum spectrum is phased in Fig. 4.7 by maximizing the absorptive real part. We observe no evidence of ESA pathways, which would appear as an opposite sign sideband located at $\hbar\omega_t = |\hbar\omega_\tau| - \Delta_{\mathrm{XX}}$ in the lower left region of single-quantum spectra [41]. The corresponding quadratures of the simulated single-quantum spectrum are plotted in Fig. 4.7b, which agree well with experiment. To examine the quadratures more closely, slices of the experimental and simulated spectra are taken at the same positions as in Figs. 4.2 and 4.5 and plotted in Fig. 4.7c. As shown by the experimental and simulated phases plotted inset, no phase flip (indicative of an ESA sideband) is observed in the pedestal region.

4.6 Summary

In conclusion, we have observed vibrational lineshapes in the third-order nonlinear response of a core-shell CNC ensemble that indicate simultaneous existence of discrete and continuum acoustic vibrational modes. As a primary mechanism of energy loss and dephasing, understanding acoustic phonon coupling is crucial to the design and implementation of CNCs in optoelectronic devices. In particular, devices based on CNC-doped glasses [45] or superlattices [46], and even other colloidal materials such as nanorods [47] or nanoplatelets [48], should be designed with an engineered spectral density to minimize energy loss and other dissipative processes due to interactions with acoustic vibrations.

References

(1) Quilter, J. H.; Brash, A. J.; Liu, F.; Glässl, M.; Barth, A. M.; Axt, V. M.; Ramsay, A. J.; Skolnick, M. S.; Fox, A. M. *Phys. Rev. Lett.* **2015**, *114*, 137401.

(2) Kaldewey, T.; Lüker, S.; Kuhlmann, A. V.; Valentin, S. R.; Ludwig, A.; Wieck, A. D.; Reiter, D. E.; Kuhn, T.; Warburton, R. J. *Phys. Rev. B* **2017**, *95*, 161302.

(3) Reindl, M.; Jöns, K. D.; Huber, D.; Schimpf, C.; Huo, Y.; Zwiller, V.; Rastelli, A.; Trotta, R. *Nano Lett.* **2017**, *17*, 4090–4095.

(4) Masia, F.; Accanto, N.; Langbein, W.; Borri, P. *Phys. Rev. Lett.* **2012**, *108*, 087401.

(5) Lüker, S.; Kuhn, T.; Reiter, D. E. *Phys. Rev. B* **2017**, *95*, 195305.

(6) Accanto, N.; Masia, F.; Moreels, I.; Hens, Z.; Langbein, W.; Borri, P. *ACS Nano* **2012**, *6*, 5227–5233.

(7) Jakubczyk, T.; Delmonte, V.; Fischbach, S.; Wigger, D.; Reiter, D. E.; Mermillod, Q.; Schnauber, P.; Kaganskiy, A.; Schulze, J.-H.; Strittmatter, A.; Rodt, S.; Langbein, W.; Kuhn, T.; Reitzenstein, S.; Kasprzak, J. *ACS Photonics* **2016**, *3*, 2461–2466.

(8) Takagahara, T. *Phys. Rev. Lett.* **1993**, *71*, 3577–3580.

(9) Kuok, M. H.; Lim, H. S.; Ng, S. C.; Liu, N. N.; Wang, Z. K. *Phys. Rev. Lett.* **2003**, *90*, 255502.

(10) Oron, D.; Aharoni, A.; de Mello Donega, C.; van Rijssel, J.; Meijerink, A.; Banin, U. *Phys. Rev. Lett.* **2009**, *102*, 177402.

(11) Werschler, F.; Hinz, C.; Froning, F.; Gumbsheimer, P.; Haase, J.; Negele, C.; de Roo, T.; Mecking, S.; Leitenstorfer, A.; Seletskiy, D. V. *Nano Lett.* **2016**, *16*, 5861–5865.

(12) Woggon, U.; Gindele, F.; Wind, O.; Klingshirn, C. *Physical Review B* **1996**, *54*, 1506–1509.

(13) Besombes, L.; Kheng, K.; Marsal, L.; Mariette, H. *Phys. Rev. B* **2001**, *63*, 155307.

(14) Fernée, M. J.; Littleton, B. N.; Cooper, S.; Rubinsztein-Dunlop, H.; Gómez, D. E.; Mulvaney, P. *J. Phys. Chem. C* **2008**, *112*, 1878–1884.

(15) Fernee, M. J.; Sinito, C.; Mulvaney, P.; Tamarat, P.; Lounis, B. *Physical Chemistry Chemical Physics* **2014**, *16*, 16957–16961.

(16) Empedocles, S. A.; Bawendi, M. G. *J. Phys. Chem. B* **1999**, *103*, 1826–1830.

(17) Cundiff, S. T.; Mukamel, S. *Phys. Today* **2013**, *66*, 44–49.

(18) Martin, E. W.; Cundiff, S. T. *Physical Review B* **2018**, *97*, 081301.

(19) Langbein, J. K.; Portolan, S.; Rastelli, A.; Wang, L.; Plumhof, J. D.; Schmidt, O. G.; W. *New J. Phys.* **2013**, *15*, 055006.

(20) Suzuki, T.; Singh, R.; Bayer, M.; Ludwig, A.; Wieck, A. D.; Cundiff, S. T. *Phys. Rev. Lett.* **2016**, *117*, 157402.

(21) Gellen, T. A.; Lem, J.; Turner, D. B. *Nano Lett.* **2017**, *17*, 2809–2815.

(22) Park, S. D.; Baranov, D.; Ryu, J.; Cho, B.; Halder, A.; Seifert, S.; Vajda, S.; Jonas, D. M. *Nano Lett.* **2017**, *17*, 762–771.

(23) Seiler, H.; Palato, S.; Sonnichsen, C.; Baker, H.; Kambhampati, P. *Nano Lett.* **2018**, *18*, 2999–3006.

(24) Lim, J.; Jeong, B. G.; Park, M.; Kim, J. K.; Pietryga, J. M.; Park, Y.-S.; Klimov, V. I.; Lee, C.; Lee, D. C.; Bae, W. K. *Adv. Mater.* **2014**, *26*, 8034–8040.

(25) Bristow, A. D.; Karaiskaj, D.; Dai, X.; Zhang, T.; Carlsson, C.; Hagen, K. R.; Jimenez, R.; Cundiff, S. T. *Review of Scientific Instruments* **2009**, *80*, 073108.

(26) Luning Prak, D. J.; Jones, M. H.; Cowart, J. S.; Trulove, P. C. *J. Chem. Eng. Data* **2015**, *60*, 1157–1165.

(27) Sirenko, A. A.; Belitsky, V. I.; Ruf, T.; Cardona, M.; Ekimov, A. I.; Trallero-Giner, C. *Phys. Rev. B* **1998**, *58*, 2077–2087.

(28) Murray, D. B.; Saviot, L. *Phys. Rev. B* **2004**, *69*, 094305.

(29) Palinginis, P.; Wang, H. *Appl. Phys. Lett.* **2001**, *78*, 1541–1543.

(30) Palinginis, P.; Tavenner, S.; Lonergan, M.; Wang, H. *Phys. Rev. B* **2003**, *67*, 201307.

(31) Krummheuer, B.; Axt, V. M.; Kuhn, T. *Phys. Rev. B* **2002**, *65*, 195313.

(32) May, V.; Kuhn, O., *Charge and Energy Transfer Dynamics in Molecular Systems*, 3rd ed.; Wiley-VCH: 2011.

(33) De Jong, M.; Seijo, L.; Meijerink, A.; Rabouw, F. T. *Phys. Chem. Chem. Phys.* **2015**, *17*, 16959–16969.

(34) Leggett, A. J.; Chakravarty, S.; Dorsey, A. T.; Fisher, M. P. A.; Garg, A.; Zwerger, W. *Reviews of Modern Physics* **1987**, *59*, 1–85.

(35) Calarco, T.; Datta, A.; Fedichev, P.; Pazy, E.; Zoller, P. *Phys. Rev. A* **2003**, *68*, 012310.

(36) Sahin, M.; Nizamoglu, S.; Kavruk, A. E.; Demir, H. V. *J. Appl. Phys.* **2009**, *106*, 043704.

(37) Lüker, S.; Kuhn, T.; Reiter, D. E. *Phys. Rev. B* **2017**, *96*, 245306.

(38) Liu, A.; Almeida, D. B.; Bae, W.-K.; Padilha, L. A.; Cundiff, S. T. *The Journal of Physical Chemistry Letters* **2019**, *10*, 6144–6150.

(39) Do, T. N.; Gelin, M. F.; Tan, H.-S. *J. Chem. Phys.* **2017**, *147*, 144103.

(40) Li, X.; Zhang, T.; Borca, C. N.; Cundiff, S. T. *Phys. Rev. Lett.* **2006**, *96*, 057406.

(41) Hao, K.; Specht, J. F.; Nagler, P.; Xu, L.; Tran, K.; Singh, A.; Dass, C. K.; Schüller, C.; Korn, T.; Richter, M.; Knorr, A.; Li, X.; Moody, G. *Nat. Commun.* **2017**, *8*, Article.

(42) Tyrrell, E. J.; Tomic, S. *J. Phys. Chem. C* **2015**, *119*, 12720–12730.

(43) Hamm, P.; Zanni, M., *Concepts and Methods of 2D Infrared Spectroscopy*, 1st ed.; Cambridge University Press: 2011.

(44) Salvador, M. R.; Sreekumari Nair, P.; Cho, M.; Scholes, G. D. *Chem. Phys.* **2008**, *350*, 56–68.

(45) Dong, G.; Wang, H.; Chen, G.; Pan, Q.; Qiu, J. *Front. Mater.* **2015**, *2*, 13.

(46) Kagan, C. R.; Lifshitz, E.; Sargent, E. H.; Talapin, D. V. *Science* **2016**, *353*, DOI: 10.1126/science.aac5523.

(47) Hu, M.; Wang, X.; Hartland, G. V.; Mulvaney, P.; Juste, J. P.; Sader, J. E. *Journal of the American Chemical Society* **2003**, *125*, 14925–14933.

(48) Flatten, L. C.; Christodoulou, S.; Patel, R. K.; Buccheri, A.; Coles, D. M.; Reid, B. P. L.; Taylor, R. A.; Moreels, I.; Smith, J. M. *Nano Lett.* **2016**, *16*, 7137–7141.

CHAPTER V

CdSe CNCs: Optical Phonon Coupling

5.1 Optical Phonon Coupling in CNCs

In Chapter IV, we discussed coupling of excitons to acoustic vibrational modes which involve in-phase motion of adjacent atoms in a lattice. In the case of a diatomic lattice, such as the aforementioned CdSe, optical vibrational modes that involve out-of-phase motion of different atoms of the diatomic basis become possible. Such out-of-phase optical vibrations generally occur at higher frequencies compared to their acoustic counterparts, and thus result in distinct spectral signatures at discrete energies. In particular, the concentrated spectral weight of optical phonons in a narrow frequency range introduces periodic modulation of the exciton energy gap which may strongly modify coherence dephasing dynamics.

5.1.1 Markovian and Non-Markovian Dephasing

As discussed in Chapter III, the interactions of excitons with their surroundings may be considered either Markovian (resonance energy fluctuations are instantaneous and uncorrelated) or non-Markovian (timescales of the interactions and exciton dynamics are comparable, and energy fluctuations are correlated). In the Markovian regime, coherences dephase exponentially at a rate $1/T_2$ and the physical origins of the dephasing mechanisms are obscured. In the non-Markovian regime however, the physical nature of the dephasing interactions manifests as non-exponential evolution of coherences [1]. Though it is known that optical phonon coupling in semiconductors may induce non-Markovian dephasing [2], the μs temporal resolution limit of spectrally-resolved single dot studies [3, 4] exceeds the correlation time of the vibrational coupling in CNCs [5].

In the spectral domain, Markovian and non-Markovian dephasing are difficult to distinguish from lineshape analysis of weak vibrational sidebands. Due to the subpicosecond timescales of most optical vibrations however, measuring optical phonon coupling directly in the temporal domain (particularly in the presence of inhomogeneous broadening in CNCs) is often even more problematic. Indeed, without access to exciton dynamics at timescales of the vibrational coupling itself, studies of CNCs have thus far assumed effective homogeneous broadening in the Markovian limit [6–9]. A technique capable of circumventing inhomogeneous broadening with femtosecond time-resolution is thus necessary to reveal signatures of non-Markovian dynamics in CNCs.

5.2 One-Quantum Spectra (T Delay Dependence)

One-quantum spectra were acquired at a temperature of 20 K for delay T increasing from 0 fs to 675 fs at 25 fs intervals. All spectra were relatively phased by

maximizing the absorptive lineshape for one quadrature. We plot in Figs. 5.1a and 5.1b the one-quantum spectrum at $T = 0$ and a slice perpendicular to the diagonal line. Here, we focus on sidebands observed at energies $\Delta E \approx \pm 26$ meV (matching the LO phonon mode energy $\hbar\omega_{LO}$ of CdSe [10]), which are highlighted by the green and yellow arrows in Fig. 5.1a and 5.1b. In Fig. 5.1c it can be seen that Fourier transforming the evolution along time T of the complex slices at $\Delta E = -26$ meV reveals a clear peak indicative of quantum oscillations in time T corresponding to allowed intraband coherences at the LO-phonon energy. Such oscillations have previously been observed in three-pulse integrated FWM experiments [11, 12], but were not spectrally resolved and correlated in their absorption and emission dynamics.

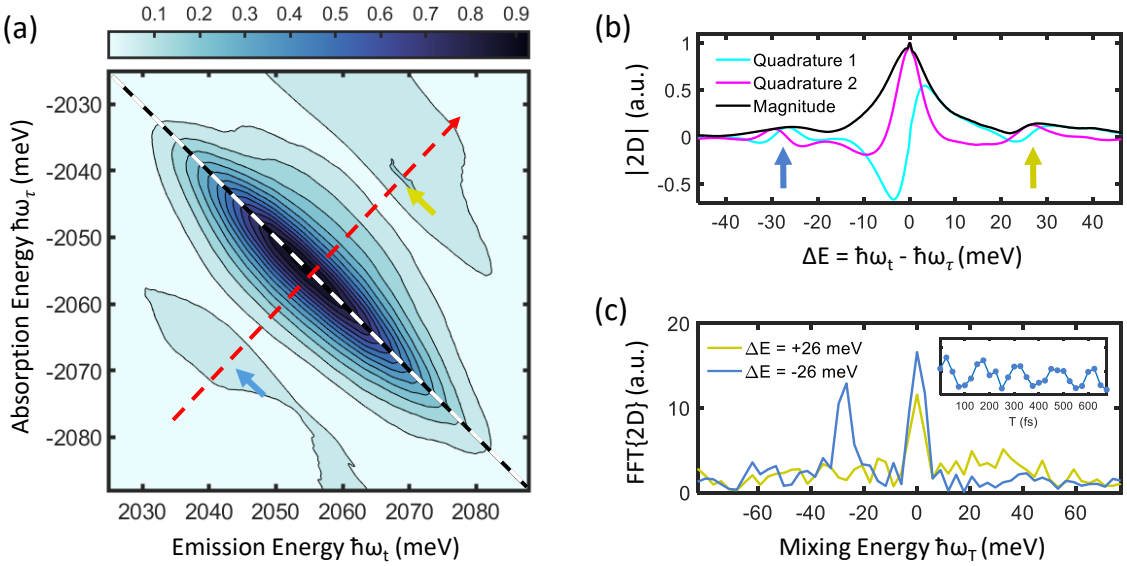

Figure 5.1: (a) Magnitude one-quantum spectrum at $T = 0$. The dashed white and red lines indicate the diagonal ($|\hbar\omega_\tau| = |\hbar\omega_t|$) and plot slice location respectively. (b) Magnitude and quadratures of the $T = 0$ plot slice centered at $|\hbar\omega_\tau| = |\hbar\omega_t| = 2055$ meV. (c) Fourier transforms of the (twice zero-padded) complex evolutions of the $\Delta E = -26$ meV and its conjugate $\Delta E = +26$ meV points. These slice positions are marked by arrows in (a) and (b). Inset shows absolute value evolution of the $\Delta E = -26$ meV point.

5.3 Zero-Quantum Spectra

Fig. 5.1 reveals two main non-intuitive observations: (1) only the Stokes sideband exhibits oscillations due to the LO-phonon coupling as a function of T and (2) its Fourier spectrum in Fig. 5.1c is one-sided. Complicating the study of these one-quantum data however, is the fact that the responses involving intraband coherences during T appear at the same coordinates as those involving population states during T. Overlapping pathways on a one-quantum spectrum may be separated by spectral filtering of the excitation pulses [13–15]. Another method is to acquire zero-quantum spectra, which spectrally separate intraband coherence pathway responses from population state responses directly [16]. We thus acquire zero-quantum spectra at τ spanning 0 fs to 550 fs, three of which are plotted in Fig. 5.2:

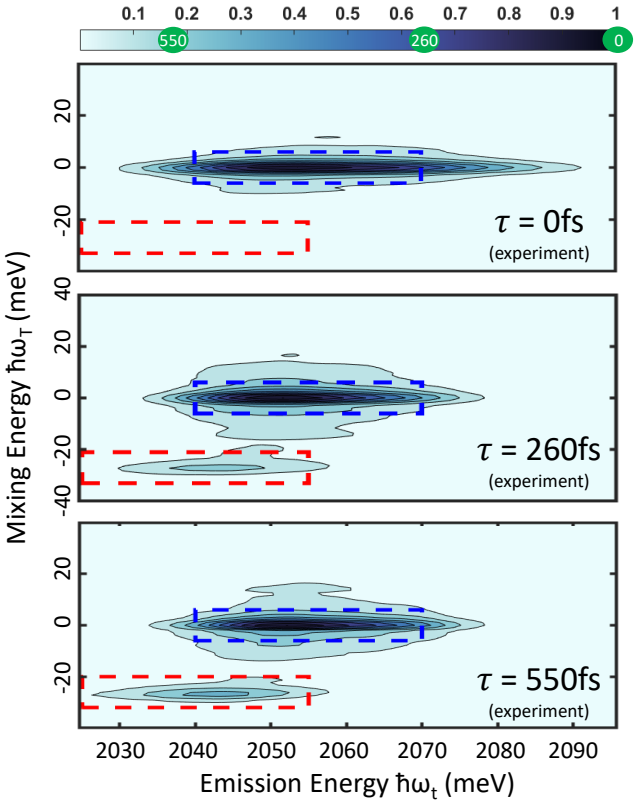

Figure 5.2: Zero-quantum plots at $\tau = 0$ fs, 260 fs, and 550 fs as indicated. Dashed blue and red boxes indicate the integrated areas for their respective peak intensities. The relative normalizations of each plot are indicated on the colorbar.

As τ increases, a sideband appears at the LO-phonon energy $\omega_T = -26$ meV. The sideband formation is also asymmetric as no peak is observed at $\omega_T = +26$ meV, agreeing with the one-sided spectrum in Fig. 5.1c. Most interestingly, integrating the spectrum over the blue and red dashed rectangles shown in Figs. 5.2 and 5.3b reveals that both peaks strengthen during early τ (130 fs for the $\omega_T = 0$ peak and 250 fs for the sideband). The full evolutions are shown in Figs. 5.3c and 5.3d. To explain these observations, we simulate the system's response and its resultant zero-quantum spectra.

5.4 Simulation

We simulate the optical response in two ways. First, we model the resonant exciton transition coupled to both acoustic continuum phonon and discrete LO-phonon modes. Their spectral densities are taken to be a Lorentzian centered at the LO-phonon energy [17] and the acoustic phonon spectral density described in Chapter IV [18, 19] with parameters found by comparison to one-quantum spectra [20]. To gain physical insight, we then neglect coupling to acoustic phonon modes and simulate a system of levels consisting of Franck-Condon transitions between ground and excited state manifolds formed from ladders of states separated by the LO-phonon energy [21]. The oscillator strengths between states are proportional to their respective Franck-Condon factors [22], which are functions of the Huang-Rhys parameter S (characterizing the electronic-vibrational coupling strength) and the initial/final vibrational excitation number m/n. Due to our laser bandwidth of 30 meV and decreasing transition strength with higher m and n, it is assumed that the main transitions contributing to the signal occur between the zeroth and first vibrational states in the ground $\{|g\rangle, |\tilde{g}\rangle\}$ and excited state manifolds $\{|e\rangle, |\tilde{e}\rangle\}$ as shown in Fig. 5.3a The ensemble-averaged transitions between these states then form the peaks of the simulated zero-quantum spectrum in Fig. 5.3b. We then make two simplifications.

First, since the sample temperature of 20 K is much lower than the LO-phonon Boltzmann temperature of 302 K, we assume all excited CNCs begin in the ground state $|g\rangle$. Second, we repeated the zero-quantum experiment with co- and cross-circularly polarized excitation and observed the same peak behaviors. Because the CNC selection rules dictate (suppression)enhancement of doubly-excited transitions by (co-)cross-circular excitation [23], we neglect transitions into doubly-excited states in the simulations.

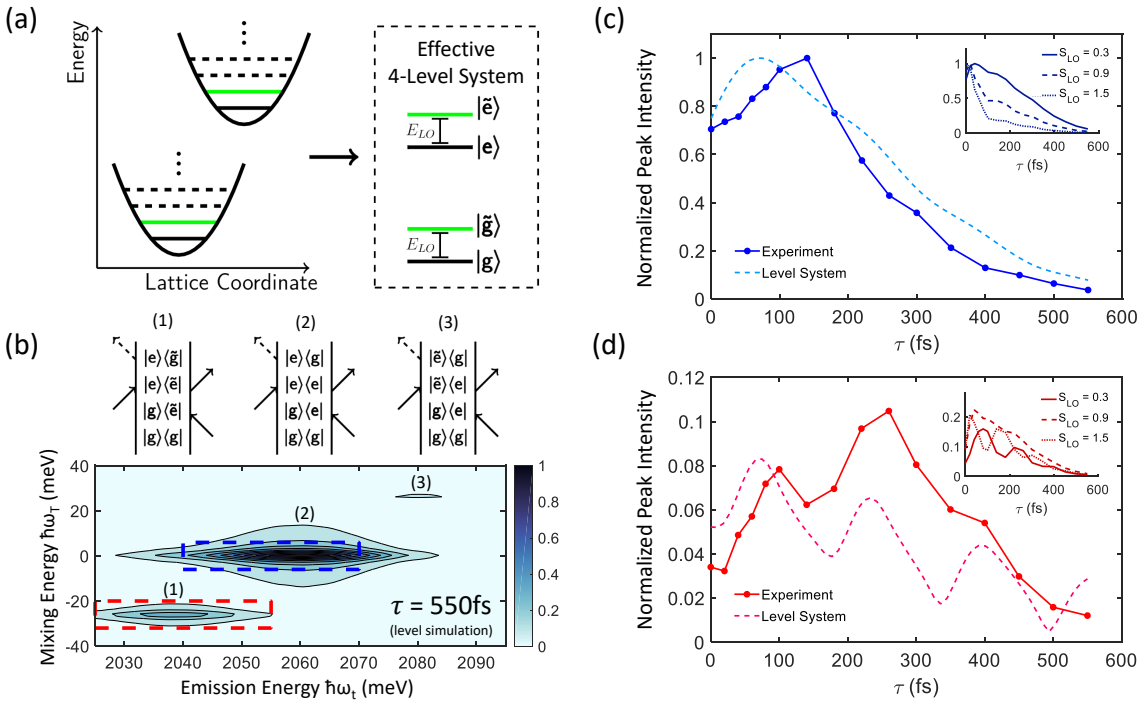

Figure 5.3: (a) Schematic of the reduced 4-level system used to interpret the data. (b) Simulated zero-quantum spectrum at $\tau = 550$ fs with the parameters $S = 0.3$, $\tau_c = \tau_c^{vib} = 1$ ps, $\Delta\omega = 15$ meV, and $\Delta\omega^{vib} = 3$ meV. Three Feynman diagrams (1), (2), and (3) are shown and their zero-quantum response positions $\{E_{emi}, E_{mix}\}$ are $\{E_g - E_{LO}, -E_{LO}\}$, $\{E_g, 0\}$, and $\{E_g + E_{LO}, +E_{LO}\}$ respectively. (c),(d) Evolution of the experimental and level system simulation $E_{mix} = 0$ and $E_{mix} = -E_{LO}$ peak intensities (integrated over the colored boxed areas in (b)) respectively as a function of delay τ. The peak intensity evolutions for spectral density simulations that include acoustic mode coupling are plotted inset for $S_{LO} = 0.3$, 0.9, and 1.5. Oscillations at ω_{LO} in (d) are due to polarization interference [24] between separate quantum pathways.

To relate the observed peaks to evolution of coherences and populations, Feynman diagrams are used (discussed in Chapter III). We show in Fig. 5.3b three example diagrams and the positions at which their responses will appear on the simulated zero-quantum spectra.

The quantum pathways represented by the Feynman diagrams associate each peak's rise in τ with evolution of interband coherences generated by the first excitation pulse, and inclusion of non-Markovian dynamics allows for a photon echo integration [25] rise to occur. Non-Markovian dephasing lineshapes are obtained by applying the cumulant expansion to the spectral diffusion trajectory $U_{ij}(t)$ of a coherence ρ_{ij}, where $i, j = \{g, e, \tilde{g}, \tilde{e}\}$, and truncating at second-order [1]:

$$\begin{aligned} \rho_{ij}(t) &\propto e^{-i\omega_{ij}t} e^{-\frac{i}{\hbar}\int_0^t U_{ij}(\tau)d\tau} \\ &\approx e^{-i\omega_{ij}t} e^{-\int_0^t \int_0^{\tau_2} C(\tau_1)d\tau_1 d\tau_2} \end{aligned} \tag{5.1}$$

where the lineshape function $g(t)$ is determined by the correlation function $C(t)$:

$$C(t) = \frac{1}{\hbar^2}\mathrm{Tr_B}\left[U_{ij}(t)U_{ij}(0)\rho_g\right] \tag{5.2}$$

where ρ_g is the equilibrium density matrix of the nuclear degrees of freedom that modulate the resonance energy and $\mathrm{Tr_B}[\ldots]$ indicates a trace over these bath states. A detailed derivation may be found in Appendix B. Though the correlation function may be studied by 3PEPS experiments [26, 27], reported 3PEPS data [5, 28] are mainly dominated by a fast decrease in peak shift and suffer from ambiguities due to coherent signals during pulse overlap.

A zero-quantum spectrum simulated for the 4-level system in Fig. 5.3a is plotted in Fig. 5.3b, with non-Markovian dephasing lineshapes from the Kubo ansatz $C(t) = \Delta\omega^2 e^{-\frac{|t|}{\tau_c}}$ (where $\Delta\omega$ and τ_c are the frequency amplitude and correlation time of the spectral diffusion) [29]. Comparison between experimental and simulated spectra at

$\tau = 550$ fs shows good agreement between peak positions and intensities. Crucially, we achieve this agreement by assigning a large spectral diffusion amplitude $\Delta\omega = 15$ meV to "vibration-less coherences" (ρ_{eg} and ρ_{ge}) and a comparatively smaller amplitude $\Delta\omega^{vib} = 3$ meV to "coupled coherences" (all ρ_{ij} involving states $\tilde{g}$ and $\tilde{e}$). Because no sidebands appear if $\Delta\omega = \Delta\omega^{vib}$, the sideband observed in experiment indicates strong modification of dephasing dynamics via coupling to lattice LO vibrational modes. However, Fig. 5.3d shows that matching the decay rate at large τ in both models result in sideband rise times much shorter than the 250 fs rise time observed from experiment. Recently, Gellen et al. have reported broadening of the homogeneous linewidth in CdSe CNCs due to LO-phonon coupling [9]. However, the discrepancy between experiment and simulation for the zero-quantum sideband evolution indicates that dynamics induced by coupling to LO modes are more complex than simply an increase in the pure-dephasing rate. The non-Markovian signatures observed may indicate an anharmonic phonon bath or even breakdown of the usual second-order cumulant truncation [30]. Single-dot studies, which have found similar lineshapes for the zero-phonon line and phonon replicas [31], are only sensitive to spectral diffusion at $> \mu$s timescales that broaden all features uniformly.

To date, two regimes of spectral diffusion have been identified, on the seconds [32] and sub-μs timescales [3]. Previous studies have focused on free surface charges [4, 33] and surface ligand rearrangement [4, 32] as possible causes for the band-edge Stark shift [34] that leads to spectral diffusion (to be contrasted with spectral diffusion due to continuum scattering in higher-dimensional systems [35]). The above theories are not sufficient to explain our results, which clearly point to LO-phonon coupling as a major factor in spectral diffusion on femtosecond timescales. We propose the random environmental perturbations that cause energy gap fluctuations become less dominant when nuclear motion is initiated in the LO mode. The local fields induced by nuclear motion extend over many unit cells - effectively over the entire core volume

of our CNCs. For CNCs grown with a shell structure, such as for our sample, it is reasonable to expect that surface charge dynamics are weak compared to Fröhlich coupling between the exciton and local fields that synchronizes the exciton motion with that of the CNC core lattice. The spectral diffusion dynamics then approach timescales on the order of the LO phonon period $T_{LO} \approx 150$ fs, and non-Markovian evolution of coupled coherences may then occur. We also found for 3 nm radius bare core (no shell) CNCs the anomalous dephasing dynamics largely disappear, shown in Fig. 5.4:

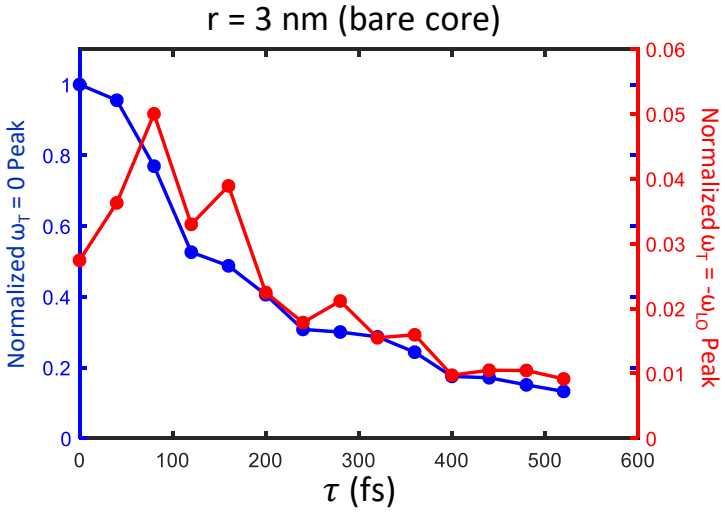

Figure 5.4: Evolution of the $E_{mix} = 0$ and $E_{mix} = -E_{LO}$ zero-quantum peak intensities, taken of the 3 nm radius bare-core nanocrystals, as a function of delay τ. Experimental parameters are identical to those of Figs. 5.2 and 5.3.

This supports our theory, since LO phonon coupling strength has been shown both experimentally and theoretically to vary weakly with dot size in the few-nm size regime [36]. We reason that removal of screening by a shell layer allows surface charge effects to take precedence over LO-phonon coupling.

5.5 Summary

In conclusion, we have found that spectral diffusion of exciton resonances in CdSe CNCs is strongly modified in the presence of coupled vibrational excitations. The non-Markovian dephasing lineshapes we have observed serves as a direct probe of exciton-phonon coupling in CNCs on their intrinsic timescales. In addition to advancing the fundamental understanding of CNCs necessary to mitigate spectral diffusion, these results will prove crucial in applications of systems with strong vibrational coupling towards areas in which pure decoherence is relevant (e.g. single-photon emission [37, 38] and quantum information [39, 40]) and emphasize the largely unexplored physics of CNCs in the femtosecond temporal regime.

References

(1) Mukamel, S., *Principles of Nonlinear Optical Spectroscopy*, 1st ed.; Oxford University Press: 1999.

(2) Hügel, W. A.; Heinrich, M. F.; Wegener, M.; Vu, Q. T.; Bányai, L.; Haug, H. *Phys. Rev. Lett.* **1999**, *83*, 3313–3316.

(3) Coolen, L.; Brokmann, X.; Spinicelli, P.; Hermier, J.-P. *Physical Review Letters* **2008**, *100*, 027403.

(4) Beyler, A. P.; Marshall, L. F.; Cui, J.; Brokmann, X.; Bawendi, M. G. *Physical Review Letters* **2013**, *111*, 177401.

(5) Salvador, M. R.; Graham, M. W.; Scholes, G. D. *The Journal of Chemical Physics* **2006**, *125*, 184709.

(6) Biadala, L.; Louyer, Y.; Tamarat, P.; Lounis, B. *Physical Review Letters* **2009**, *103*, 037404.

(7) Masia, F.; Accanto, N.; Langbein, W.; Borri, P. *Phys. Rev. Lett.* **2012**, *108*, 087401.

(8) Accanto, N.; Masia, F.; Moreels, I.; Hens, Z.; Langbein, W.; Borri, P. *ACS Nano* **2012**, *6*, 5227–5233.

(9) Gellen, T. A.; Lem, J.; Turner, D. B. *Nano Lett.* **2017**, *17*, 2809–2815.

(10) Fernee, M. J.; Sinito, C.; Mulvaney, P.; Tamarat, P.; Lounis, B. *Physical Chemistry Chemical Physics* **2014**, *16*, 16957–16961.

(11) Mittleman, D. M.; Schoenlein, R. W.; Shiang, J. J.; Colvin, V. L.; Alivisatos, A. P.; Shank, C. V. *Physical Review B* **1994**, *49*, 14435–14447.

(12) Patton, B.; Langbein, W.; Woggon, U.; Maingault, L.; Mariette, H. *Physical Review B* **2006**, *73*, 235354.

(13) Tollerud, J. O.; Hall, C. R.; Davis, J. A. *Optics Express* **2014**, *22*, 6719–6733.

(14) Wen, P.; Nelson, K. A. *The Journal of Physical Chemistry A* **2013**, *117*, 6380–6387.

(15) Senlik, S. S.; Policht, V. R.; Ogilvie, J. P. *The Journal of Physical Chemistry Letters* **2015**, *6*, 2413–2420.

(16) Yang, L.; Zhang, T.; Bristow, A. D.; Cundiff, S. T.; Mukamel, S. *The Journal of Chemical Physics* **2008**, *129*, 234711.

(17) Seibt, J.; Pullerits, T. *The Journal of Physical Chemistry C* **2013**, *117*, 18728–18737.

(18) Calarco, T.; Datta, A.; Fedichev, P.; Pazy, E.; Zoller, P. *Phys. Rev. A* **2003**, *68*, 012310.

(19) Lüker, S.; Kuhn, T.; Reiter, D. E. *Phys. Rev. B* **2017**, *96*, 245306.

(20) Liu, A.; Almeida, D. B.; Bae, W.-K.; Padilha, L. A.; Cundiff, S. T. *The Journal of Physical Chemistry Letters* **2019**, *10*, 6144–6150.

(21) May, V.; Kuhn, O., *Charge and Energy Transfer Dynamics in Molecular Systems*, 3rd ed.; Wiley-VCH: 2011.

(22) De Jong, M.; Seijo, L.; Meijerink, A.; Rabouw, F. T. *Phys. Chem. Chem. Phys.* **2015**, *17*, 16959–16969.

(23) Scholes, G. D. *The Journal of Chemical Physics* **2004**, *121*, 10104–10110.

(24) Meier, T.; Thomas, P.; Koch, S., *Coherent Semiconductor Optics: From Basic Concepts to Nanostructure Applications*, 1st ed.; Springer: 2006.

(25) Lorenz, V. O.; Cundiff, S. T. *Physical Review Letters* **2005**, *95*, 163601.

(26) Fleming, G. R.; Passino, S. A.; Nagasawa, Y. *Philosophical Transactions of the Royal Society of London. Series A: Mathematical, Physical and Engineering Sciences* **1998**, *356*, 389.

(27) Lorenz, V. O.; Mukamel, S.; Zhuang, W.; Cundiff, S. T. *Physical Review Letters* **2008**, *100*, 013603.

(28) McKimmie, L. J.; Lincoln, C. N.; Jasieniak, J.; Smith, T. A. *The Journal of Physical Chemistry C* **2010**, *114*, 82–88.

(29) Hamm, P.; Zanni, M., *Concepts and Methods of 2D Infrared Spectroscopy*, 1st ed.; Cambridge University Press: 2011.

(30) Chen, H.-B.; Lambert, N.; Cheng, Y.-C.; Chen, Y.-N.; Nori, F. *Scientific Reports* **2015**, *5*, Article.

(31) Fernée, M. J.; Littleton, B. N.; Cooper, S.; Rubinsztein-Dunlop, H.; Gómez, D. E.; Mulvaney, P. *J. Phys. Chem. C* **2008**, *112*, 1878–1884.

(32) Fernée, M. J.; Plakhotnik, T.; Louyer, Y.; Littleton, B. N.; Potzner, C.; Tamarat, P.; Mulvaney, P.; Lounis, B. *The Journal of Physical Chemistry Letters* **2012**, *3*, 1716–1720.

(33) Müller, J.; Lupton, J. M.; Rogach, A. L.; Feldmann, J.; Talapin, D. V.; Weller, H. *Physical Review Letters* **2004**, *93*, 167402.

(34) Empedocles, S. A.; Bawendi, M. G. *Science* **1997**, *278*, 2114.

(35) Wang, Z.; Reimann, K.; Woerner, M.; Elsaesser, T.; Hofstetter, D.; Hwang, J.; Schaff, W. J.; Eastman, L. F. *Physical Review Letters* **2005**, *94*, 037403.

(36) Lin, C.; Gong, K.; Kelley, D. F.; Kelley, A. M. *The Journal of Physical Chemistry C* **2015**, *119*, 7491–7498.

(37) Lin, X.; Dai, X.; Pu, C.; Deng, Y.; Niu, Y.; Tong, L.; Fang, W.; Jin, Y.; Peng, X. *Nature Communications* **2017**, *8*, 1132.

(38) Chandrasekaran, V.; Tessier, M. D.; Dupont, D.; Geiregat, P.; Hens, Z.; Brainis, E. *Nano Letters* **2017**, *17*, 6104–6109.

(39) Pryor, C. E.; Flatté, M. E. *Applied Physics Letters* **2006**, *88*, 233108.

(40) Engel, H.-A.; Recher, P.; Loss, D. *Solid State Communications* **2001**, *119*, 229–236.

CHAPTER VI

$CsPbI_3$ Perovskite Nanocubes (PNCs)

Cesium lead-halide perovskites were first synthesized over a century ago with a general chemical formula $CsPbX_3$ (where X = Cl, Br, or I). Recently, synthesis of $CsPbX_3$ perovskite nanocubes (PNCs) was achieved [1, 2], which combines the advantages of perovskites (e.g., efficient luminescence, long carrier diffusion length) with that of colloidal NC materials (e.g., surface engineering, size-tunable emission). Perovskite NCs exhibit luminescence with quantum yields reaching nearly unity [3], in contrast to the optimized 80% quantum yield achieved by chalcogenide NCs coated with a gradient shell [4]. Although all other colloidal materials suffer inhibited emission from lower energy dark states [5], the unusual brightness of perovskite NCs is now believed to originate from an optically active, nondegenerate triplet state that emits efficiently despite the presence of a dark singlet state [6, 7].

The unique exciton fine-structure of perovskite NCs has significantly extended the potential applications of colloidal NCs. In particular, the three non-degenerate bright triplet states and their orthogonally-oriented dipole moments have generated much excitement for potential applications in quantum information processing [8, 9]. However, engineering exciton superposition states as information carriers will require an intimate knowledge of their coherent dynamics, which are still not well-understood. The exciton fine structure of perovskite NCs has thus far only been studied via single-

NC photoluminescence [6, 10, 11] and transient absorption [12, 13] techniques, which have provided information only about their incoherent population dynamics. Furthermore, inhomogeneous spectral broadening due to NC size dispersion limits the utility of linear spectroscopic techniques in studying NC ensembles. More sophisticated methods are thus required [14–17] to extract the desired ensemble-averaged coherent properties of perovskite NCs.

6.1 Sample and Experiment

The NCs studied are cube-shaped, with side lengths of 8.7 ± 2.6 nm measured from transmission electron microscopy measurements (shown in Fig. 6.1a). These sizes are comparable to the $CsPbI_3$ exciton Bohr diameter (12 nm) [1], and correspond to a room temperature 1S exciton absorption peak centered around 1900 meV (shown in Fig. 6.1b). The synthesis method is described in [18]. Just as described in Chapter IV, we suspend the NCs in heptamethylnonane to study them at low temperatures.

In this Chapter, we acquire both one-quantum spectra (which correlate the absorption energy $\hbar\omega_\tau$ with the emission energy $\hbar\omega_t$) and zero-quantum spectra (which correlate the intraband mixing energy $\hbar\omega_T$ and the emission energy $\hbar\omega_t$) while additionally varying the excitation beam polarizations. Specifically, the polarization of the second pulse (labeled B in Fig. 6.1d) is chosen to align either parallel or orthogonal to the co-linear polarizations of the other two pulses to probe different quantum pathways. We denote the two polarization schemes as co-linear excitation and cross-linear excitation respectively.

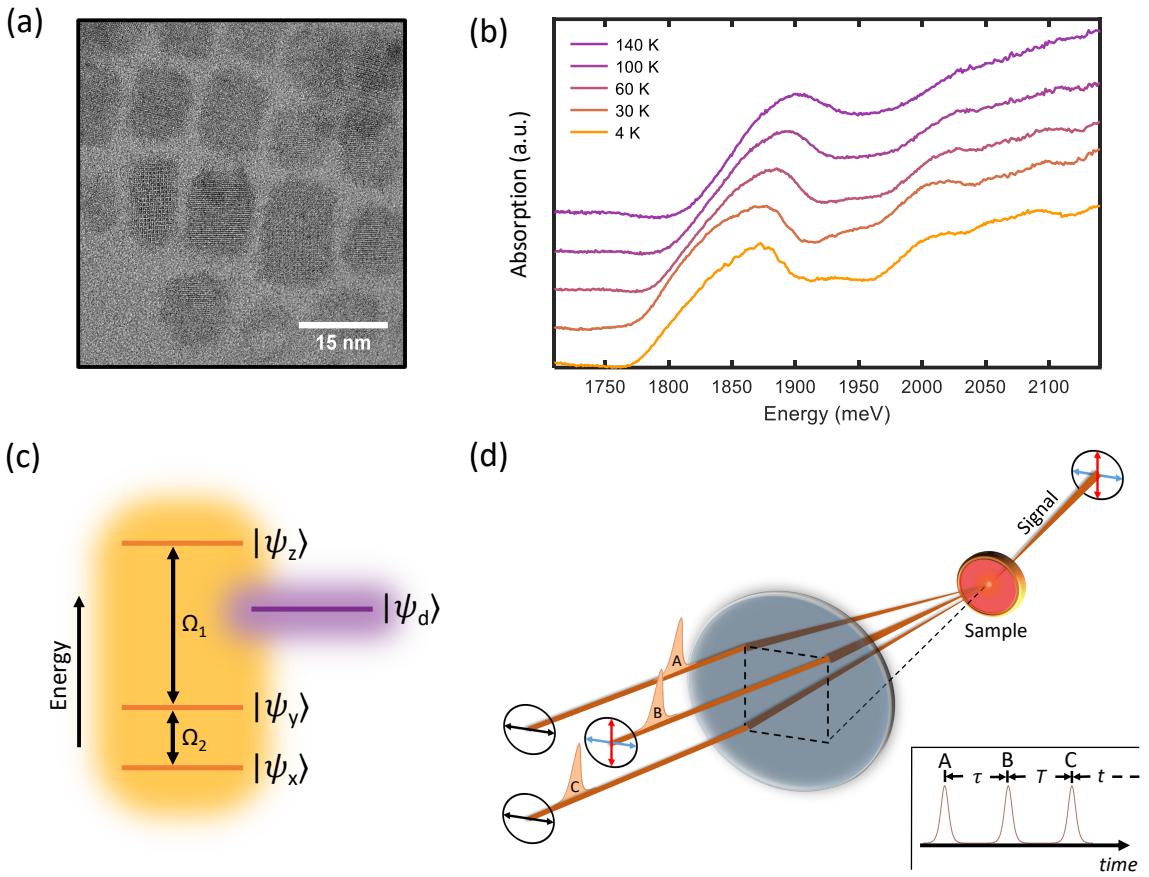

Figure 6.1: (a) Transmission electron micrograph of representative $CsPbI_3$ NCs. (b) Perovskite NC absorption spectra as a function of temperature [19]. (c) Energy level diagram of the non-degenerate bright triplet states $\{\psi_x, \psi_y, \psi_z\}$ that form the band-edge. The dark singlet state $|\psi_d\rangle$ is shown to lie between states $|\psi_y\rangle$ and $|\psi_z\rangle$, which is argued in the main text. (d) Schematic of the MDCS experiment. Three pulses A, B, and C arranged in the box geometry are focused onto the sample with varying time delays as shown in the inset. Double-sided arrows in circles denote the polarization of each pulse. Pulses A and C are horizontally polarized, which is indicated by the horizontal arrows. Pulse B is either horizontally or vertically polarized, which corresponds to an emitted signal of either horizontal or vertical polarization respectively as indicated by arrows of matching color of the emitted signal.

6.2 One-Quantum Spectra

One-quantum spectra were acquired at a temperature of 4.6 K with co-linear and cross-linear excitation (shown in Figs. 6.2a and 6.2b). Both spectra show numerous peaks that are elongated in the diagonal direction ($|\hbar\omega_\tau| = |\hbar\omega_t|$), reflecting inhomo-

geneous broadening [20]. By taking cross-diagonal slices (indicated by the red/white dashed lines in Figs. 6.2a and 6.2b), the ensemble-averaged homogeneous response of NCs with a certain resonance energy is obtained [20]. We plot cross-diagonal slices of the one-quantum spectra in Figs. 6.2c and 6.2d. In the full slices (inset), asymmetric peaks are observed for $|\Delta E| \gtrsim 4$ meV which we attribute to electronic-vibrational coupling. The main plots of each slice section (highlighted by the yellow boxes inset) show symmetric peaks that, due to their polarization dependence, we attribute to absorption and emission involving different triplet state coherences.

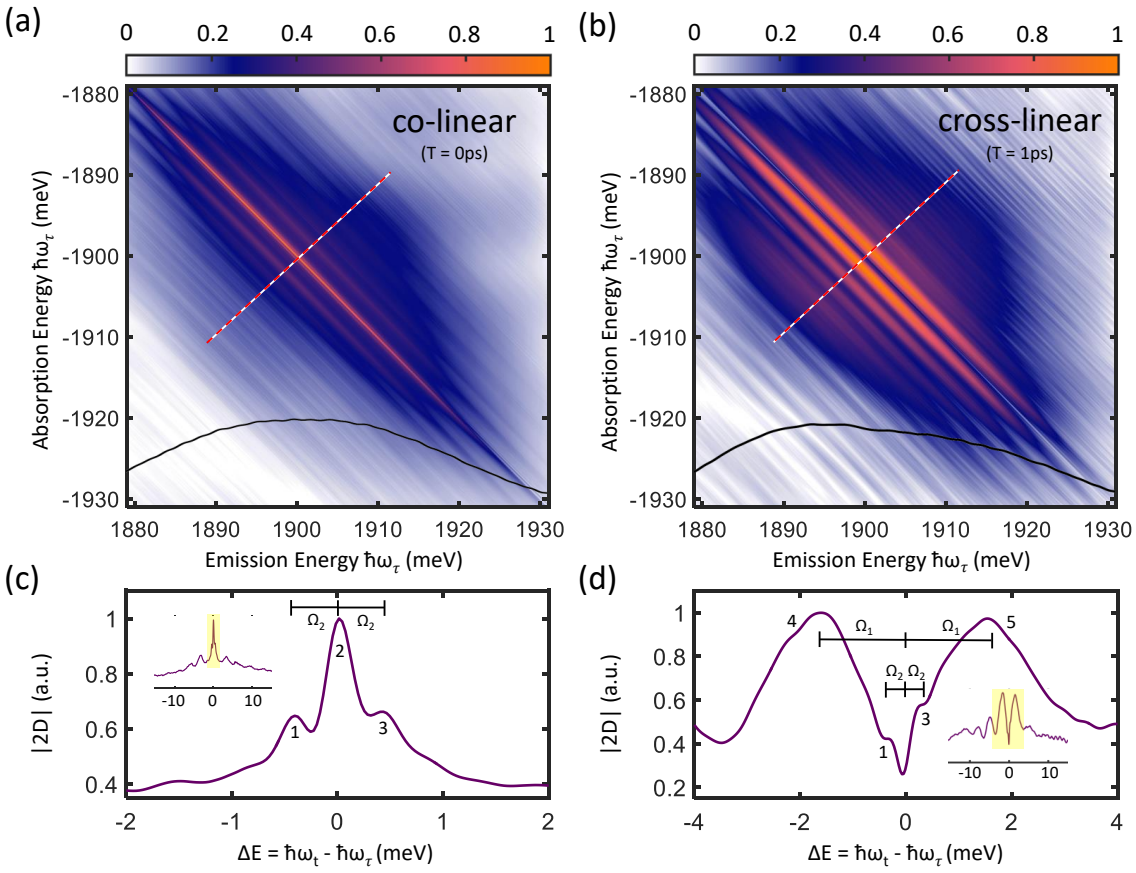

Figure 6.2: Magnitude one-quantum spectrum at 4.6 K with (a) co-linear and (b) cross-linear excitation. The white/red dashed lines and solid black lines indicate the cross-slice locations and laser pulse spectra respectively. Cross-slice centered at $|\hbar\omega_\tau| = |\hbar\omega_t| = 1900$ meV of the (c) co-linear and (d) cross-linear excitation one-quantum spectrum. Numbers in (c) and (d) indicate peaks arising from electronic interband coherences and populations.

As discussed in Chapter III, the origin of observed peaks is interpreted as changes

in the system density matrix induced by each pulse that form accessible quantum pathways [21]. Peaks 1 and 3 in Fig. 6.2c are generated by absorption and emission of coherences involving $|g\rangle$ and both triplet states $|\psi_x\rangle$ and $|\psi_y\rangle$. We note that our measurements do not inform the ordering of states $\left|\psi_{x/y}\right\rangle$, so we assume the ordering shown in Fig. 6.1c for labeling the dephasing rates discussed below. The central peak 2 is likewise generated by quantum pathways involving absorption and emission by coherences of identical resonance energy $|g\rangle\langle\psi_i|$ and $|\psi_i\rangle\langle g|$ respectively. In Fig. 6.2d peaks 1 and 3 are visible as shoulders on two new peaks 4 and 5, which are generated by absorption and emission of coherences involving $|g\rangle$ and triplet states $|\psi_y\rangle$ and $|\psi_z\rangle$. The polarization dependence of all five peaks reflects orthogonally-oriented linear dipole moments of the three triplet states. Here, the peak strengths are determined by the projection of each dipole moment onto the observation plane of each NC. However, the absence of a clear sideband at $\Delta E = \pm(\Omega_1 + \Omega_2)$, corresponding to coupling between the transitions involving $|g\rangle$ and triplet states $|\psi_x\rangle$ and $|\psi_z\rangle$, suggests a much stronger dipole moment for $|\psi_y\rangle$ compared to those of $|\psi_x\rangle$ and $|\psi_z\rangle$.

6.2.1 Cross-Diagonal Lineshape Fits

Fitting the cross-diagonal lineshapes also extracts the homogeneous linewidths γ_i (see Appendix C and [20]) of triplet state transitions between $|g\rangle$ and $|\psi_i\rangle$. In this context one-quantum spectra are particularly useful when compared to integrated FWM techniques [22], since the cross-diagonal slice position $|\hbar\omega_t| = |\hbar\omega_\tau|$ reflects an effective NC size. Though the peaks 1 and 4 and peaks 3 and 5 would ideally be mirror-images, vibrational coupling distorts the lineshapes of peaks 1 and 4. We thus fit only the $\Delta E \geq 0$ side. Fit of the co-linear slice lineshape (Fig. 6.2c) gives a sideband (peaks 1 and 3) dephasing rate $\hbar\frac{\gamma_x+\gamma_y}{2} = 0.12$ meV (5.49 ps) and a zero-phonon line (peak 2) dephasing rate 0.124 meV (5.32 ps). Fit of peaks 4 and 5 in the cross-linear slice lineshape (Fig. 6.2d) gives a dephasing rate $\hbar\frac{\gamma_y+\gamma_z}{2} = 0.496$ meV

(1.33 ps). The fitted triplet state energy splittings are likewise $\Omega_1 = 1.82$ meV and $\Omega_2 = 0.24$ meV. If the dipole moment of state $|\psi_y\rangle$ is indeed much larger than those of $|\psi_x\rangle$ and $|\psi_z\rangle$, the zero-phonon line dephasing rate will approximately equal $\hbar\gamma_y$ which in turn determines the individual triplet state dephasing rates $\gamma_x = 0.116$ meV ($T_2^x = 5.68$ ps), $\gamma_y = 0.124$ meV ($T_2^y = 5.32$ ps), and $\gamma_z = 0.868$ meV ($T_2^z = 0.76$ ps).

It is quite unexpected that the optical dephasing rate γ_z is so much faster than those of the other two triplet states γ_x and γ_y. Although this disparity suggests a fundamentally different dephasing mechanism for coherences involving state $|\psi_z\rangle$, photoluminescence of similar orthorhombic perovskite NCs that exhibit triplet state structure reveals similar emission linewidths for all three states of the manifold [6, 7]. We resolve this discrepancy by proposing a unique exciton fine-structure comprised of a dark singlet state $|\psi_d\rangle$ that lies above the states $|\psi_x\rangle$ and $|\psi_y\rangle$, which form the band-edge, while remaining below the third triplet state $|\psi_z\rangle$ (shown in Fig. 6.1c). Rapid relaxation from $|\psi_z\rangle$ to $|\psi_d\rangle$ then significantly decreases the population lifetime T_1^z, and consequently T_2^z as well [21]. Such a fine-structure has been theoretically predicted [23] in certain ranges of NC size due to competition between the Rashba effect and electron-hole exchange interaction. Our hypothesis is further supported by previous photoluminescence studies of $CsPbI_3$ NCs of nearly identical size [10] which revealed polarized doublets corresponding to $|\psi_x\rangle$ and $|\psi_y\rangle$ but did not detect the third triplet state $|\psi_z\rangle$, whose emission would be quenched by non-radiative relaxation to $|\psi_d\rangle$ according to our model. In accordance with the predicted size-dependence of the relative dark state energy [23], we also observe an abrupt increase in T_2^y with increasing slice position which results from a crossing in energy of $|\psi_y\rangle$ and $|\psi_d\rangle$ (shown in Fig. 6.3). While γ_x does not exhibit a clear monotonic increase or decrease with changing size, γ_y sharply increases at a slice position of around 1900 meV. This indicates that, within the size-distribution probed by our laser bandwidth, $|\psi_y\rangle$ becomes degenerate with $|\psi_d\rangle$ at an energy gap of around 1900 meV and

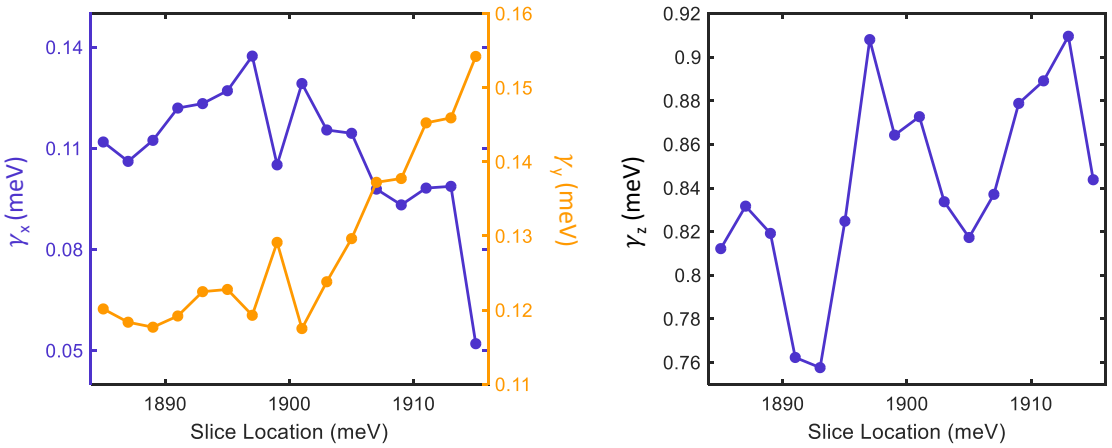

Figure 6.3: Extracted dephasing rates of each triplet state transition.

becomes increasingly higher in energy at larger slice positions. However, a more statistically comprehensive study is needed to draw firm quantitative conclusions about the nanocrystal size dependence of the triplet state energies and dephasing rates.

6.3 Zero-Quantum Spectra

Many of the quantum pathways that generate the sidebands in Figs. 6.2a and 6.2b involve inter-triplet coherences, which are quantum coherences between triplet states that are not necessarily dipole coupled [24]. Of both fundamental and practical importance is the inter-triplet coherence time, which defines the timescale during which the superposition states involved may be coherently manipulated. Inter-triplet coherences are those density matrix elements of the form $|\psi_i\rangle \langle\psi_j|$ where $i, j = \{x, y, z\}$ and $i \neq j$. To directly measure and characterize these coherences, we take zero-quantum spectra at varying temperature and delay τ. For co-linear excitation no inter-triplet coherences between $|\psi_x\rangle$ and $|\psi_y\rangle$ are observed. It is ambiguous whether their corresponding peaks are weak, or are simply obscured by the linewidth of a central $\omega_T = 0$ peak. For cross-linear excitation, we further isolate the inter-triplet coherence pathways by passing the measured FWM signal through a vertical polar-

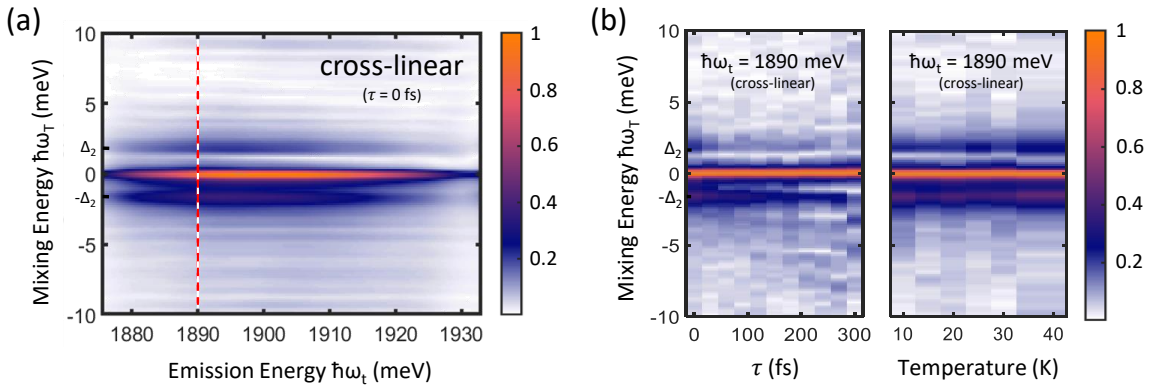

Figure 6.4: (a) Magnitude zero-quantum spectrum taken at $\tau = 0$ fs and 20 K by passing the FWM signal through a vertical polarizer. Two sidebands due to inter-triplet coherences are observed. (b) Evolution of normalized slices taken along the dashed red line in (a) at $\hbar\omega_t = 1890$ meV as a function of delay τ (at 20 K) and temperatures [10, 15, 20, 25, 30, 40] K (at $\tau = 0$ fs).

izer. We plot a resultant cross-linear zero-quantum spectrum at 20 K in Fig. 6.4a. Sidebands are observed at mixing energies identical to the positions of peaks 4 and 5 in Fig. 6.2d, which we attribute to inter-triplet coherences between $|\psi_y\rangle$ and $|\psi_z\rangle$. An inter-triplet coherence between $|\psi_x\rangle$ and $|\psi_z\rangle$ is observed in neither the co-linear nor cross-linear zero-quantum spectra, which is consistent with a dominant transition dipole of state $|\psi_y\rangle$ as argued above. In Fig. 6.4b, the evolutions of normalized slices (at $\hbar\omega_T = 1890$ meV) as a function of delay τ and temperature are shown. The FWM signal dephases rapidly with increasing τ and results in an equally rapid decrease of sideband visibility, in contrast to the opposite behavior of vibrational intraband coherences discussed in Chapter V and [17]. No change in the amplitude ratio between sidebands 6 and 8 is observed as temperature increases, confirming that the state splitting observed indeed belongs to the bright-triplet excited state rather than from thermal filling of higher-lying ground states. We note that the triplet state coherences in one-quantum spectra broaden significantly with increasing temperature, and are not resolved at temperatures above 15 K. In contrast, no significant broadening is observed in Fig. 6.3b of the inter-triplet coherence linewidth up to 40 K, indicating that inter-triplet coherences are robust against thermal dephasing [14].

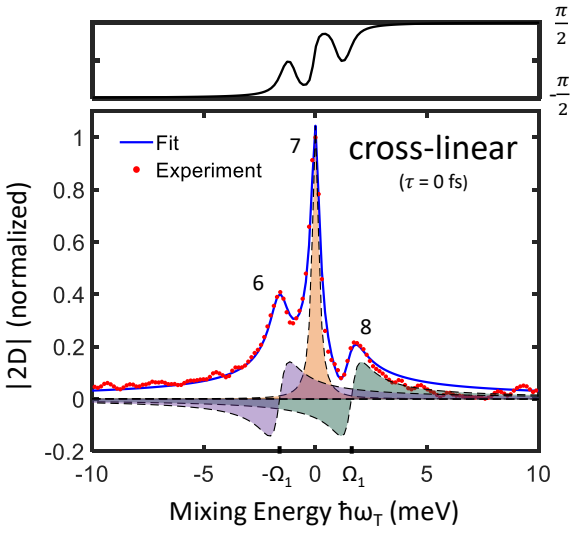

Figure 6.5: Fit of cross-slice taken at $\tau = 0$ fs, in which the complex Lorentzians of peaks 6 and 8 are shifted by phases $-\frac{\pi}{2}$ relative to peak 7. The shaded curves represent the real quadratures of each Lorentzian used to fit lineshape.

A slice at $\tau = 0$ fs is plotted in Fig. 6.5, from which we can extract the inter-triplet coherence time. However, the quantum pathways that generate peaks 6 and 8 involve identical dipole moments $\mu_y^2\mu_z^2$, from which we expect equal peak amplitudes contrary to the uneven peaks observed. This difference is due to interference between the three complex Lorentzian lineshapes underlying the overall amplitude lineshape, and the fit to experiment is performed by shifting the phase of each sideband Lorentzian lineshape by identical factors of $-\frac{\pi}{2}$ relative to the central $\omega_T = 0$ peak. From our fit, we extract an energy splitting $\Omega_1 = 1.61$ meV and an inter-triplet coherence time $T_2^{yz} = 1.36$ ps at 20 K.

6.4 Summary

In conclusion, we have measured and characterized both optical frequency triplet coherences and terahertz frequency inter-triplet coherences. We have also presented evidence of an exciton bandedge whose emission is partially quenched by an intermediate dark state, which contributes important insight into the controversial nature

of exciton ground states in different perovskite NC materials [6, 7]. As a material still in its infancy, perovskite NCs show promise for applications in opto-electronic devices. Particularly, the minimal thermal broadening of inter-triplet coherences observed here motivates study of applications above cryogenic temperatures. For example, in a triplet-state analogue of valleytronics in two-dimensional materials [25], superpositions of triplet states could be initialized and read-out with linearly polarized light and coherently manipulated via terahertz radiation as information carriers [26].

References

(1) Protesescu, L.; Yakunin, S.; Bodnarchuk, M. I.; Krieg, F.; Caputo, R.; Hendon, C. H.; Yang, R. X.; Walsh, A.; Kovalenko, M. V. *Nano Letters* **2015**, *15*, 3692–3696.

(2) Ha, S.-T.; Su, R.; Xing, J.; Zhang, Q.; Xiong, Q. *Chemical Science* **2017**, *8*, 2522–2536.

(3) Liu, F.; Zhang, Y.; Ding, C.; Kobayashi, S.; Izuishi, T.; Nakazawa, N.; Toyoda, T.; Ohta, T.; Hayase, S.; Minemoto, T.; Yoshino, K.; Dai, S.; Shen, Q. *ACS Nano* **2017**, *11*, 10373–10383.

(4) Jaehoon, L.; Guk, J. B.; Myeongjin, P.; Kyeong, K. J.; M., P. J.; Young-Shin, P.; I., K. V.; Changhee, L.; C., L. D.; Ki, B. W. *Advanced Materials* **2014**, *26*, 8034–8040.

(5) Nirmal, M.; Norris, D. J.; Kuno, M.; Bawendi, M. G.; Efros, A. L.; Rosen, M. *Physical Review Letters* **1995**, *75*, 3728–3731.

(6) Becker, M. A. et al. *Nature* **2018**, *553*.

(7) Tamarat, P.; Bodnarchuk, M. I.; Trebbia, J.-B.; Erni, R.; Kovalenko, M. V.; Even, J.; Lounis, B. *Nature Materials* **2019**, *18*, 717–724.

(8) Rainò, G.; Becker, M. A.; Bodnarchuk, M. I.; Mahrt, R. F.; Kovalenko, M. V.; Stöferle, T. *Nature* **2018**, *563*, 671–675.

(9) Utzat, H.; Sun, W.; Kaplan, A. E. K.; Krieg, F.; Ginterseder, M.; Spokoyny, B.; Klein, N. D.; Shulenberger, K. E.; Perkinson, C. F.; Kovalenko, M. V.; Bawendi, M. G. *Science* **2019**, *363*, 1068.

(10) Yin, C.; Chen, L.; Song, N.; Lv, Y.; Hu, F.; Sun, C.; Yu, W. W.; Zhang, C.; Wang, X.; Zhang, Y.; Xiao, M. *Physical Review Letters* **2017**, *119*, 026401.

(11) Chen, L.; Li, B.; Zhang, C.; Huang, X.; Wang, X.; Xiao, M. *Nano Letters* **2018**, *18*, 2074–2080.

(12) Makarov, N. S.; Guo, S.; Isaienko, O.; Liu, W.; Robel, I.; Klimov, V. I. *Nano Letters* **2016**, *16*, 2349–2362.

(13) Castañeda, J. A.; Nagamine, G.; Yassitepe, E.; Bonato, L. G.; Voznyy, O.; Hoogland, S.; Nogueira, A. F.; Sargent, E. H.; Cruz, C. H. B.; Padilha, L. A. *ACS Nano* **2016**, *10*, 8603–8609.

(14) Moody, G.; Kavir Dass, C.; Hao, K.; Chen, C.-H.; Li, L.-J.; Singh, A.; Tran, K.; Clark, G.; Xu, X.; Berghäuser, G.; Malic, E.; Knorr, A.; Li, X. *Nature Communications* **2015**, *6*, Article.

(15) Hao, K.; Moody, G.; Wu, F.; Dass, C. K.; Xu, L.; Chen, C.-H.; Sun, L.; Li, M.-Y.; Li, L.-J.; MacDonald, A. H.; Li, X. *Nature Physics* **2016**, *12*.

(16) Liu, A.; Almeida, D. B.; Bae, W.-K.; Padilha, L. A.; Cundiff, S. T. *The Journal of Physical Chemistry Letters* **2019**, *10*, 6144–6150.

(17) Liu, A.; Almeida, D. B.; Bae, W. K.; Padilha, L. A.; Cundiff, S. T. *Physical Review Letters* **2019**, *123*, 057403.

(18) Nagamine, G.; Rocha, J. O.; Bonato, L. G.; Nogueira, A. F.; Zaharieva, Z.; Watt, A. A. R.; de Brito Cruz, C. H.; Padilha, L. A. *The Journal of Physical Chemistry Letters* **2018**, *9*, 3478–3484.

(19) Liu, A.; Bonato, L. G.; Sessa, F.; Almeida, D. B.; Isele, E.; Nagamine, G.; Zagonel, L. F.; Nogueira, A. F.; Padilha, L. A.; Cundiff, S. T. *arXiv e-prints* **2019**, arXiv:1908.04881, arXiv:1908.04881.

(20) Siemens, M. E.; Moody, G.; Li, H.; Bristow, A. D.; Cundiff, S. T. *Optics Express* **2010**, *18*, 17699–17708.

(21) Mukamel, S., *Principles of Nonlinear Optical Spectroscopy*, 1st ed.; Oxford University Press: 1999.

(22) Becker, M. A.; Scarpelli, L.; Nedelcu, G.; Rainò, G.; Masia, F.; Borri, P.; Stöferle, T.; Kovalenko, M. V.; Langbein, W.; Mahrt, R. F. *Nano Letters* **2018**, *18*, 7546–7551.

(23) Sercel, P. C.; Lyons, J. L.; Wickramaratne, D.; Vaxenburg, R.; Bernstein, N.; Efros, A. L. *Nano Letters* **2019**, DOI: 10.1021/acs.nanolett.9b01467.

(24) Ferrio, K. B.; Steel, D. G. *Phys. Rev. Lett.* **1998**, *80*, 786–789.

(25) Schaibley, J. R.; Yu, H.; Clark, G.; Rivera, P.; Ross, J. S.; Seyler, K. L.; Yao, W.; Xu, X. *Nature Reviews Materials* **2016**, *1*, Review Article.

(26) Langer, F.; Schmid, C. P.; Schlauderer, S.; Gmitra, M.; Fabian, J.; Nagler, P.; Schüller, C.; Korn, T.; Hawkins, P. G.; Steiner, J. T.; Huttner, U.; Koch, S. W.; Kira, M.; Huber, R. *Nature* **2018**, *557*, 76–80.

CHAPTER VII

$CsPbI_3$ Perovskite Nanoplatelets

Although perovskite nanocrystals were initially limited to nanocube geometries, synthesis of perovskite nanoplatelets was shortly achieved [1, 2]. Perovskite nanoplatelets share the efficient and tunable photo-physics of their nanocube counterparts while possessing unique characteristics of their own. Their planar geometry allows for directional light absorption/emission [3] and efficient energy transfer in stacked superlattices [4], while precise control of the polyhedral layer thickness results in remarkable homogeneity in the dominant out-of-plane quantum confinement [5]. Because the absorption and emission energy of nanoplatelets is predominantly determined by the nanoplatelet thickness, variation in lateral confinement of electronic excitations is commonly believed to be negligible.

Claims that colloidal nanoplatelet absorption/emission resonances are homogeneously broadened have primarily been based on comparing single nanoplatelet and ensemble photoluminescence spectra [6–8]. However, such measurements may be biased by exceptional nanoplatelets and do not constitute definitive proof that colloidal nanoplatelets are homogeneously broadened. A first integrated four-wave mixing (FWM) study has also been performed on $MAPbI_3$ nanoplatelets to extract the average homogeneous linewidth at a single temperature and excitation density [9], but provided no information about its dependence on temperature, excitation den-

sity, or nanoplatelet lateral size. Elucidating the dominant homogeneous broadening mechanisms is crucial to engineer colloidal nanoplatelets with ever narrower optical resonances for use in applications such as low-threshold lasing [10] and to increase the already impressive energy transfer efficiencies of nanoplatelet superlattices [4, 5]. To properly determine the homogeneous and inhomogeneous linewidths in the presence of a large lateral size distribution, a more advanced nonlinear spectroscopic technique such as MDCS is required to separate and characterize the two contributions to linewidth broadening.

7.1 Sample and Experiment

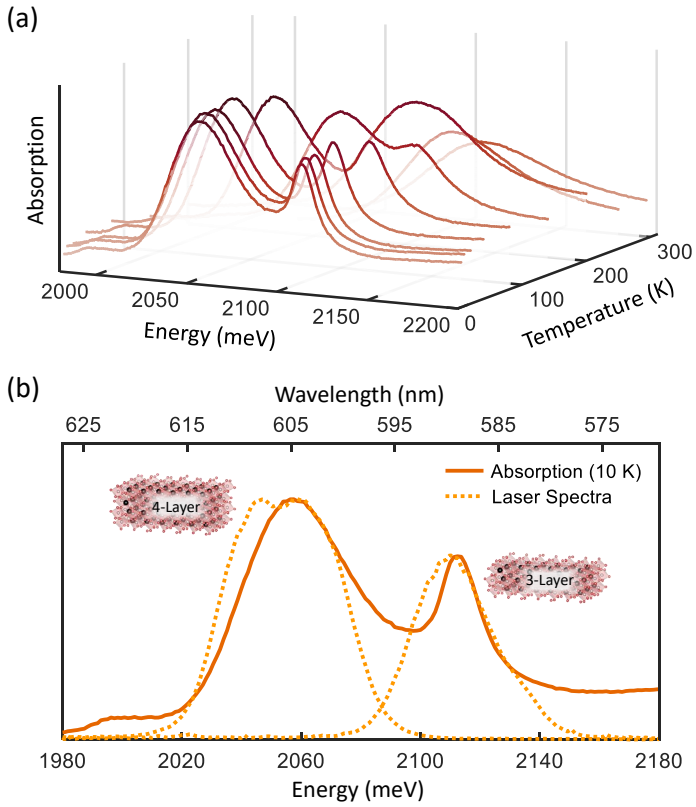

Figure 7.1: (a) Temperature-dependent absorption spectra of nanoplatelets synthesized at 170°C. A single broad absorption peak is visible at room-temperature, which splits into two peaks attributed to different layer thicknesses at cryogenic temperatures. (b) Comparison of the 4-layer (left) and 3-layer (right) absorption peaks in (a) at 10 K with the respective excitation laser spectra used to perform MDCS.

The studied $CsPbI_3$ perovskite nanoplatelets were synthesized via a method [11] modified from that reported by Sheng, et al. [12]. Both 3-layer and 4-layer thick nanoplatelets were synthesized at a reaction temperature of 170°C, as evident from the low-temperature absorption spectra shown in Fig. 7.1. Measurements were also performed on 4-layer nanoplatelets synthesized at a reaction temperature of 110°C, which yields smaller 4-layer nanoplatelets with larger resonance energies and no observable 3-layer nanoplatelets.

The spectra of the 70 fs duration pulses used to perform MDCS are centered at each nanoplatelet absorption peak (shown in Fig. 7.1b). All pulses are co-linearly polarized.

7.2 One-Quantum Spectra (Temperature Dependence)

In one-quantum spectra, inhomogeneous and homogeneous broadening manifest as broadening in the diagonal ($|\hbar\omega_\tau| = |\hbar\omega_t|$) and orthogonal cross-diagonal directions respectively [13]. The cross-diagonal lineshape at a given position along the diagonal $\hbar\omega_{\mathrm{CD}} = |\hbar\omega_\tau| = |\hbar\omega_t|$ reflects the ensemble-averaged homogeneous response of nanoplatelets with a resonance energy $\hbar\omega_{\mathrm{CD}}$. Fitting the diagonal and cross-diagonal lineshapes simultaneously [13, 14] then provides the homogeneous and inhomogeneous linewidths ($\gamma = \frac{\hbar}{T_2}$ and σ respectively). However, because the 4-layer nanoplatelet absorption linewidths exceed our laser bandwidth, the diagonal linewidths in our one-quantum spectra do not necessarily represent the total inhomogeneous distribution of resonance energies.

Absolute-value one-quantum spectra of 4-layer and 3-layer nanoplatelets are shown in Figs. 7.2a and 7.2c respectively. The vertical and horizontal axes represent the absorption and emission energies of the colloidal nanoplatelets as indicated, and the negative absorption energies reflect inverse phase evolution during delays τ and t. The diagonally-elongated lineshapes indicate that, despite dominant out-of-plane quantum

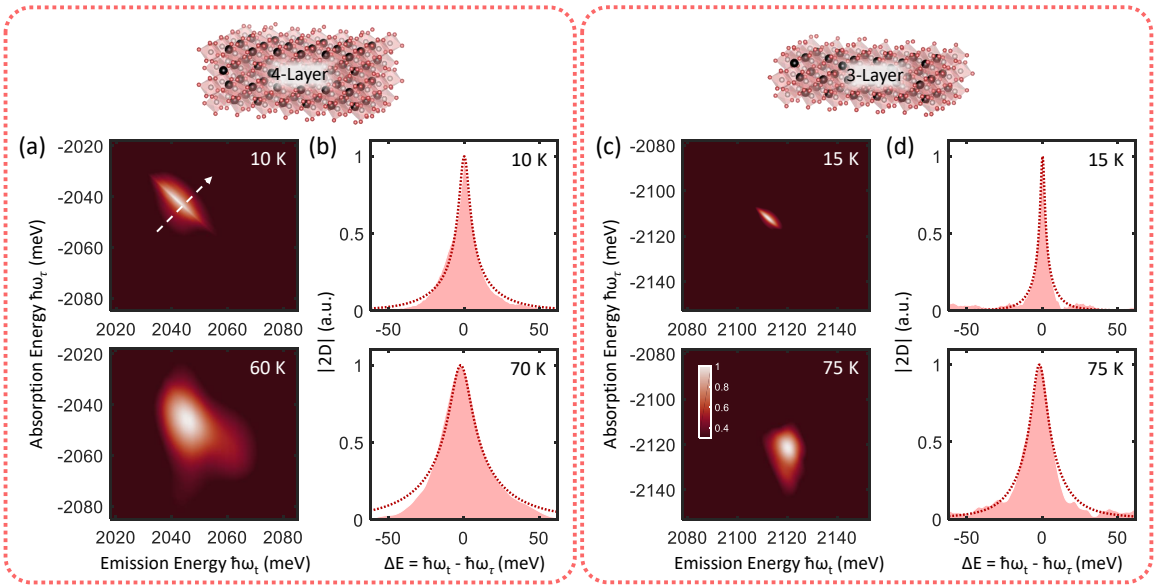

Figure 7.2: (a,c) Absolute value one-quantum spectra of (a) 4-layer and (c) 3-layer nanoplatelets synthesized at a reaction temperature of 170°C and acquired with excitation densities $N_X = 1.753 \times 10^{13}$ and 1.875×10^{13} cm^{-2} respectively at the indicated temperatures. The waiting time was set to $T = 1$ ps to avoid coherent signals during pulse overlap. (b,d) Cross-diagonal slices of the (b) 4-layer and (d) 3-layer one-quantum spectra centered at 2043 meV and 2113 meV respectively. The cross-diagonal slice location for the 15 K slice in (b) is indicated by the white dashed arrow in (a). Experimental data and lineshape fits are plotted as the shaded area plots and dotted lines respectively.

confinement, exciton resonances in perovskite nanoplatelets still possess inhomogeneous broadening due to varying confinement of lateral exciton center-of-mass motion. The degree of inhomogeneous broadening depends strongly on layer thickness, which is evident from the difference in diagonal widths between Figs. 7.2a and 7.2c.

7.2.1 Thermal Dephasing

With increasing temperature, the lineshapes in the cross-diagonal direction broaden, which is characteristic of thermal dephasing due to elastic exciton-phonon scattering [15, 16]. Specifically, first-order exciton-phonon scattering processes result in broad-

ening that may be modeled by the following expression [17]:

$$\gamma(T, N_X) = \gamma_0(N_X) + AT \tag{7.1}$$

where $\gamma_0(N_X)$ is the zero-temperature linewidth at a given excitation density N_X and the second term represents coupling to low-energy acoustic phonon modes with coupling strength A. In anticipation of the experimental linewidth temperature dependence, we neglect broadening due to discrete optical phonon modes that result in an exponential increase. To quantify thermal broadening in each system we plot cross-diagonal slices centered at $\hbar\omega_{\mathrm{CD}} = 2050$ meV and 2113 meV in Figs. 7.2b and 7.2d, which reflect homogeneous broadening of nanoplatelets with resonance energy $\hbar\omega_{\mathrm{CD}}$. The lineshapes fit well to expressions derived for exponential dephasing in the Markovian limit [13]. As the nanoplatelet bandgaps blue-shift with increasing temperature, we adjust the slice locations by a commensurate energy.

The temperature-dependent values of the homogeneous linewidth γ (each fitted from a one-quantum spectrum taken at its respective temperature) are plotted in Fig. 7.3. The linewidth increases linearly with temperature, which is characteristic of acoustic phonon coupling as described by equation (7.1). The thermal dephasing parameters extracted from the linear fits shown in Fig. 7.3 are $A = 0.032$ meV/K (3-layer) and $A = 0.041$ meV/K (4-layer), which indicate relatively weaker acoustic phonon coupling in the former. Weaker vibrational coupling in 3-layer nanoplatelets is also reflected in their smaller thermal band-gap renormalization. Both values are comparable to that of similar two-dimensional systems such as monolayer WSe_2 (0.06 meV/K) [15] and quantum wells (≈ 0.01 meV/K) [18].

Because optical phonon coupling is extremely weak in nanoplatelets, as evidenced by the linear bandgap temperature-dependence [19] and absence of vibrational sidebands in the experimental one-quantum spectra, it is reasonable to assume the homo-

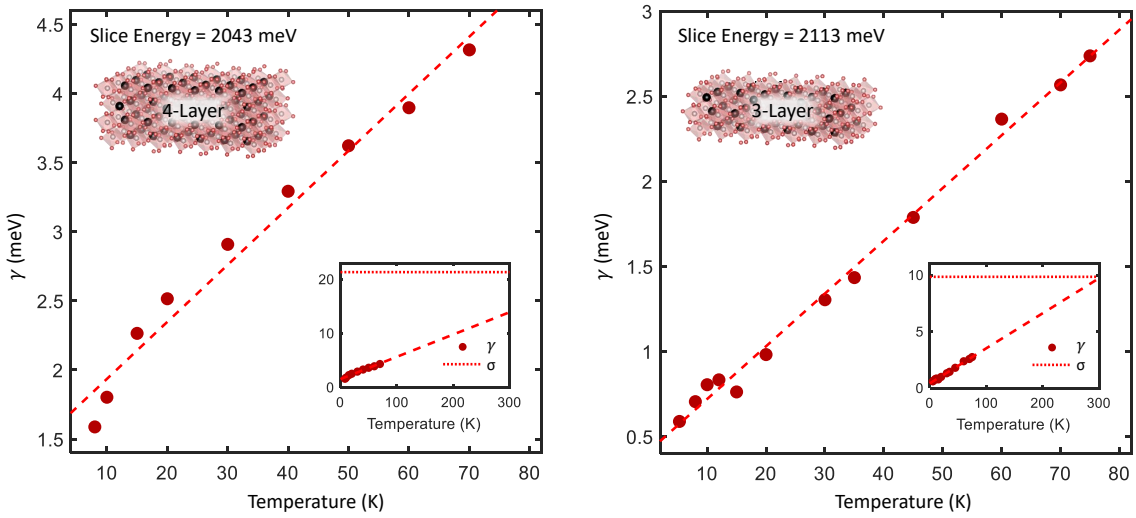

Figure 7.3: Dependence of the fitted homogeneous linewidths on temperature for 4-layer (left) and 3-layer (right) nanoplatelets synthesized at a reaction temperature of 170°C. Experimental parameters are the same as in Fig. 7.2. The homogeneous linewidths for both samples follow linear temperature dependences. The linear fits shown are $\gamma = 1.52 + (0.041)T$ meV (4-layer) and $\gamma = 0.41 + (0.032)T$ meV (3-layer). The values of γ and σ extrapolated to room-temperature are plotted inset. The inhomogeneous linewidths, found by fitting the low-temperature absorption peaks to Voigt lineshapes as described in the text, are $\sigma = 21.32$ meV (4-layer) and $\sigma = 9.84$ meV (3-layer) and plotted as horizontal dotted lines.

geneous linewidth continues increasing linearly to higher temperatures. In the insets of Fig. 7.3, we plot the inhomogeneous linewidth (found by fitting the absorption peaks at 10 K to Voigt profiles [20] by using our respective measured values of γ) and extrapolate the homogeneous linewidths to room-temperature to predict the crossover temperature at which homogeneous broadening exceeds inhomogeneous broadening. The crossover temperatures for 3-layer and 4-layer nanoplatelets are 296 K and 480 K, which indicate that thinner nanoplatelets are indeed homogeneously broadened at room temperature. In 4-layer nanoplatelets the extrapolated homogeneous linewidth at room temperature ($\gamma(294\text{ K}) = 15.43$ meV) is still significantly smaller than the inhomogeneous linewidth ($\sigma = 19.72$ meV), suggesting that further work is required to minimize size inhomogeneity in thick nanoplatelets for homogeneous exciton resonances at long-wavelengths.

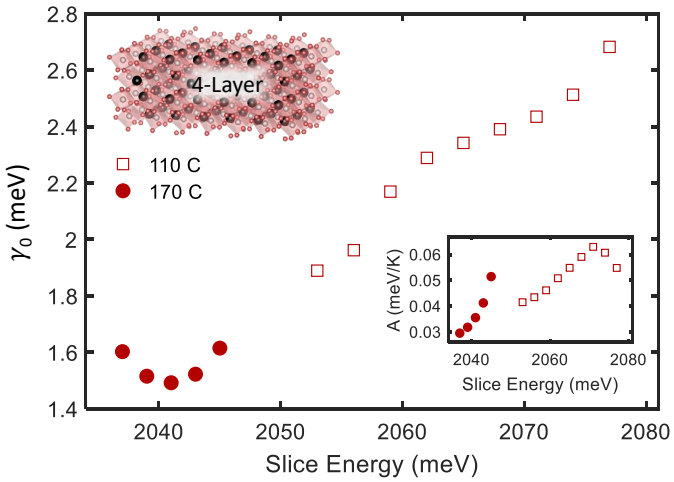

Figure 7.4: Dependence of the zero-temperature linewidth on slice position. The values γ_0 are found by extrapolating the fitted linewidths to zero-temperature, as shown in Fig. 7.3. The dependences of the fitted thermal broadening parameter A on slice position are then plotted inset for both 4-layer samples synthesized at 110°C and 170°C reaction temperatures.

7.2.2 Resonance Energy Dependence

The large inhomogeneous broadening in 4-layer nanoplatelets also invites further resolving their temperature dependence analysis in terms of resonance energy, which corresponds to the cross-diagonal slice position in a one-quantum spectrum. In colloidal nanoplatelets, the resonance energy distribution directly corresponds to variations in lateral size and quantum confinement. The extrapolated zero-temperature homogeneous linewidth γ_0 is plotted in Fig. 7.4 as a function of slice position, which exhibits an increase with increasing slice position (resonance energy). The slice position (resonance energy) dependence of the thermal dephasing parameter A is then plotted for both samples in Fig. 7.4. Interestingly, the 110°C nanoplatelets exhibit increasing thermal dephasing with increasing resonance energy before decreasing beyond 2070 meV. The physical origin of this inflection point at 2070 meV is not obvious, but its energy coincides with the activation energy of excitation-induced dephasing (shown in Fig. 7.5a and discussed in the next section). The observed trend may thus arise from an interplay between confinement of the exciton wavefunction and

center-of-mass motion, and the concomitant changes in vibrational coupling.

7.3 One-Quantum Spectra (Power Dependence)

Another dominant extrinsic dephasing mechanism in semiconductors is excitation-induced dephasing (EID) [15, 21, 22], which arises from electronic many-body interactions. Our narrow excitation bandwidths, well-matched to the probed exciton resonances, restricts the source of EID to unbound exciton-exciton scattering [15, 23]. In two-dimensional systems, this may be described by a linear dependence on excitation density N_X [15, 24]:

$$\gamma(T, N_X) = \gamma(T) + BN_X \tag{7.2}$$

where $\gamma(T)$ is the zero-density linewidth at temperature T and B is the exciton-exciton interaction strength. The excitation densities are calculated from the experimental laser parameters and sample optical density [15].

The homogeneous linewidth at 10 K is plotted in Fig. 7.5a as a function of excitation density for both 3-layer and 4-layer nanoplatelets. We find that the linewidth increases linearly with excitation density for both thicknesses and temperatures, a clear signature of EID, as described by equation (7.2). While the fitted EID parameters B are 1.56×10^{-14} meV cm^2 and 1.67×10^{-14} meV cm^2 for 3-layer and 4-layer (170°C) nanoplatelets respectively, it varies nearly an order of magnitude from 1.41×10^{-14} meV cm^2 to 1.07×10^{-13} meV cm^2 for 110°C 4-layer nanoplatelets depending on slice position (shown in Fig. 7.5b). These values are much smaller than the EID parameter in, for example, monolayer WSe_2 (2.7×10^{-12} meV cm^2 [15]), which may be due to differences in Coulomb screening between a glass matrix (in this study) and vacuum [15].

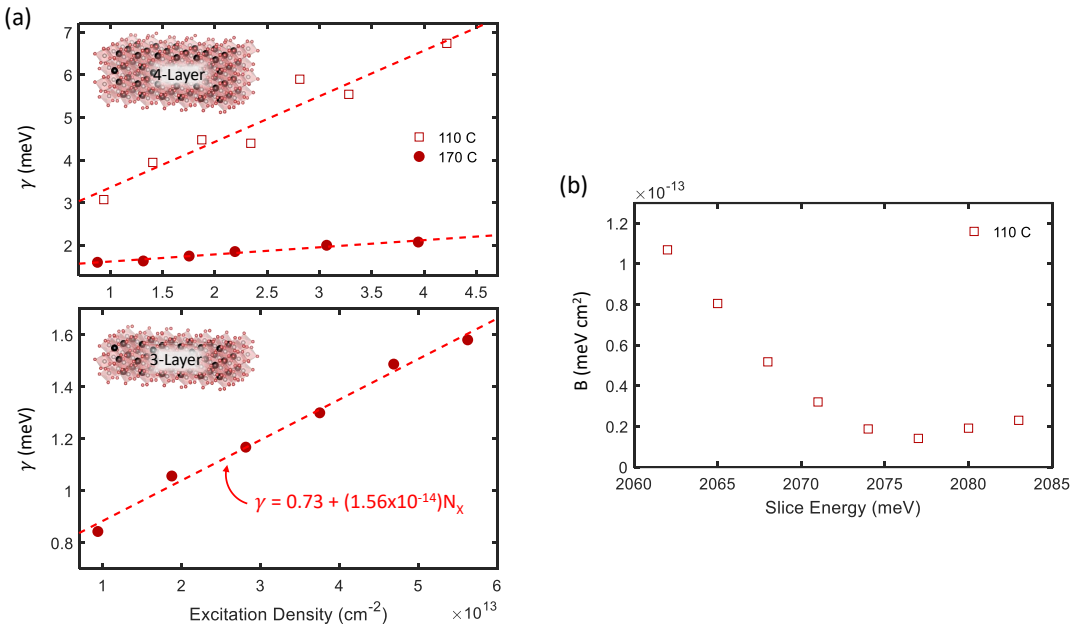

Figure 7.5: (a) Fitted values of the homogeneous linewidth as a function of excitation density for 4-layer (top) and 3-layer (bottom) nanoplatelets at 10 K. The 4-layer linewidths are fitted from slices taken at 2062 meV (110°C) and 2043 meV (170°C) while the 3-layer linewidths are fitted from slices at 2113 meV. (b) Dependence of the EID parameter B on slice position in 4-layer (110°C) nanoplatelets. The EID parameter of 170°C 4-layer nanoplatelets does not noticeably depend on slice position.

We now discuss the relative EID strengths between the 110°C and 170°C 4-layer nanoplatelets, which differ by an order-of-magnitude (shown in Fig. 7.5a). We attribute this decrease in EID for larger 170°C nanoplatelets to a corresponding decrease in inter-exciton separation [15]. The increase in EID with decreasing slice position for 110° nanoplatelets may then be understood by considering the effect of nanoplatelet size on multiple exciton dynamics. In large nanoplatelets (smaller resonance energy) multiple excitons may form without forming biexciton complexes, which may then undergo scattering events that result in EID. In small nanoplatelets (larger resonance energy), the nanoplatelet size becomes comparable to the exciton Bohr diameter in $CsPbI_3$ of 12 nm [25] and favors biexciton formation (whose binding energy lies beyond our excitation bandwidth [26]).

7.4 Summary

In conclusion, we have directly measured and quantified both homogeneous and inhomogeneous broadening in $CsPbI_3$ perovskite nanoplatelets. Via temperature- and excitation density-dependent measurements, we have revealed the dominant homogeneous broadening mechanisms to be acoustic phonon coupling and excitation-induced dephasing. By informing the relevant design parameters for engineering optical resonances, our results are directly relevant for implementing colloidal nanoplatelets in practical devices. For example, we find that large-area nanoplatelets offer advantages such as narrow intrinsic homogeneous linewidths and minimal excitation-induced dephasing at low excitation densities and are therefore likely to be advantageous in coherent opto-electronic devices. However, small-area nanoplatelets (that suppress multiple free-exciton formation) may be required for narrow and stable exciton resonances in high optical intensity applications.

References

(1) Bekenstein, Y.; Koscher, B. A.; Eaton, S. W.; Yang, P.; Alivisatos, A. P. *Journal of the American Chemical Society* **2015**, *137*, 16008–16011.

(2) Tong, Y.; Bladt, E.; Aygüler, M. F.; Manzi, A.; Milowska, K. Z.; Hintermayr, V. A.; Docampo, P.; Bals, S.; Urban, A. S.; Polavarapu, L.; Feldmann, J. *Angewandte Chemie International Edition* **2016**, *55*, 13887–13892.

(3) Jurow, M. J.; Morgenstern, T.; Eisler, C.; Kang, J.; Penzo, E.; Do, M.; Engelmayer, M.; Osowiecki, W. T.; Bekenstein, Y.; Tassone, C.; Wang, L.-W.; Alivisatos, A. P.; Brütting, W.; Liu, Y. *Nano Letters* **2019**, *19*, 2489–2496.

(4) Rowland, C. E.; Fedin, I.; Zhang, H.; Gray, S. K.; Govorov, A. O.; Talapin, D. V.; Schaller, R. D. *Nature Materials* **2015**, *14*.

(5) Weidman, M. C.; Seitz, M.; Stranks, S. D.; Tisdale, W. A. *ACS Nano* **2016**, *10*, 7830–7839.

(6) Tessier, M. D.; Javaux, C.; Maksimovic, I.; Loriette, V.; Dubertret, B. *ACS Nano* **2012**, *6*, 6751–6758.

(7) Nasilowski, M.; Mahler, B.; Lhuillier, E.; Ithurria, S.; Dubertret, B. *Chemical Reviews* **2016**, *116*, 10934–10982.

(8) Izquierdo, E.; Robin, A.; Keuleyan, S.; Lequeux, N.; Lhuillier, E.; Ithurria, S. *Journal of the American Chemical Society* **2016**, *138*, 10496–10501.

(9) Bohn, B. J.; Simon, T.; Gramlich, M.; Richter, A. F.; Polavarapu, L.; Urban, A. S.; Feldmann, J. *ACS Photonics* **2018**, *5*, 648–654.

(10) Yang, Z.; Pelton, M.; Fedin, I.; Talapin, D. V.; Waks, E. *Nature Communications* **2017**, *8*, 143.

(11) Bonato, L. G.; Moral, R. F.; Nagamine, G.; de Oliveira, A. A.; Germino, J. C.; da Silva, D. S.; Galembeck, F.; Padilha, L. A.; Nogueira, A. F. Revealing the Role of Tin (IV) Halides in the Anisotropic Growth of $CsPbX_3$ Perovskite Nanoplates (to be published).

(12) Sheng, X. et al. *Advanced Functional Materials* **2018**, *28*, 1800283.

(13) Siemens, M. E.; Moody, G.; Li, H.; Bristow, A. D.; Cundiff, S. T. *Optics Express* **2010**, *18*, 17699–17708.

(14) Martin, E. W.; Cundiff, S. T. *Physical Review B* **2018**, *97*, 081301.

(15) Moody, G.; Kavir Dass, C.; Hao, K.; Chen, C.-H.; Li, L.-J.; Singh, A.; Tran, K.; Clark, G.; Xu, X.; Berghäuser, G.; Malic, E.; Knorr, A.; Li, X. *Nature Communications* **2015**, *6*, Article.

(16) Liu, A.; Almeida, D. B.; Bae, W. K.; Padilha, L. A.; Cundiff, S. T. *Physical Review Letters* **2019**, *123*, 057403.

(17) Rudin, S.; Reinecke, T. L.; Segall, B. *Physical Review B* **1990**, *42*, 11218–11231.

(18) Wagner, H. P.; Schätz, A.; Maier, R.; Langbein, W.; Hvam, J. M. *Physical Review B* **1997**, *56*, 12581–12588.

(19) Liu, A.; Bonato, L. G.; Sessa, F.; Almeida, D. B.; Isele, E.; Nagamine, G.; Zagonel, L. F.; Nogueira, A. F.; Padilha, L. A.; Cundiff, S. T. *arXiv e-prints* **2019**, arXiv:1908.04881, arXiv:1908.04881.

(20) Whiting, E. E. *Journal of Quantitative Spectroscopy and Radiative Transfer* **1968**, *8*, 1379–1384.

(21) Wang, H.; Ferrio, K. B.; Steel, D. G.; Berman, P. R.; Hu, Y. Z.; Binder, R.; Koch, S. W. *Physical Review A* **1994**, *49*, R1551–R1554.

(22) Shacklette, J. M.; Cundiff, S. T. *Physical Review B* **2002**, *66*, 045309.

(23) Schultheis, L.; Kuhl, J.; Honold, A.; Tu, C. W. *Physical Review Letters* **1986**, *57*, 1635–1638.

(24) Honold, A.; Schultheis, L.; Kuhl, J.; Tu, C. W. *Physical Review B* **1989**, *40*, 6442–6445.

(25) Protesescu, L.; Yakunin, S.; Bodnarchuk, M. I.; Krieg, F.; Caputo, R.; Hendon, C. H.; Yang, R. X.; Walsh, A.; Kovalenko, M. V. *Nano Letters* **2015**, *15*, 3692–3696.

(26) Chen, J. et al. *Communications Physics* **2019**, *2*, 80.

CHAPTER VIII

Outlook and Future Directions

This dissertation has presented our results from applying multi-dimensional coherent spectroscopy to colloidal nanocrystals at cryogenic temperatures. Particularly at low temperatures, virtually every single spectrum taken contains features with new physics ready to be teased out by careful interpretation. As such, future directions abound and we list here only a small subset.

8.1 Novel Colloidal Heterostructures

In Chapters IV and V we discussed our results on CdSe CNCs, which were synthesized in a core-shell geometry. Other novel heterostructures are possible, such as core-shell nanoplatelets and so-called spherical quantum wells [1] consisting of a shell active region. We have performed initial linear and nonlinear spectroscopic measurements of CdSe spherical quantum wells, which have revealed greatly-enhanced exciton-phonon coupling that is sensitive to outer capping layer thickness. Further work is necessary to elucidate the effect of changing active-layer geometry on exciton-phonon coupling in CNCs.

8.2 Vibrational Coupling in Perovskite Nanocubes

In Chapter VI we presented multi-dimensional spectra of $CsPbI_3$ perovskite nanocubes and primarily discussed features arising from the triplet exciton fine-structure. However, the one-quantum spectra are dominated by large pedestals that reflect electronic coupling to acoustic vibrations. Due to the complex perovskite lattice basis, many optical vibrational modes simultaneously couple to excitons and give rise to numerous sidebands superimposed on the acoustic phonon pedestals. Such strong signatures of exciton-phonon coupling indicate that lattice vibrations must play a primary role in determining the opto-electronic properties of perovskite nanocubes. A systematic study involving MDCS of perovskite nanocubes with varying waiting time and temperature will help elucidate the underlying microscopic dynamics.

8.3 Broad-Bandwidth MDCS of CNCs

The results presented in this dissertation were acquired using an optical parametric amplifier (OPA) pumped by a Ti:Sapph regenerative amplifier. Such a system was among the first to allow for wavelength-tunable femtosecond pulses with serviceable bandwidth. Today, these systems have largely been supplanted by OPAs pumped by fiber-based amplifiers that not only offer superior operational stability, but also increased wavelength-tunability, broader spectral bandwidths, and larger pulse energies. In particular, broader spectral bandwidths greatly increase the capabilities of MDCS in studying CNCs. Signatures of high-energy optical phonon modes and trions/biexcitons become accessible, and coupling to higher-lying electronic states could be investigated. The ability to cover a greater portion of the inhomogeneous spectral distribution also facilitates more efficient systematic size-dependence studies.

8.4 Pre-Pulse MDCS of CNCs

As demonstrated by our group [2, 3] and others [4, 5], the addition of an incoherent pre-pulse prior to each MDCS measurement introduces a host of new phenomena that manifest in multi-dimensional spectra. While traditional MDCS measurements assume quantum pathways that begin in an electronic ground state at thermal equilibrium, a pre-pulse prepares a certain excited-state population that is also probed by MDCS. In the context of CNCs, a particularly interesting experiment would involve a high-photon energy pre-pulse (at least twice the fundamental energy gap) that excites hot-carriers. As these hot-carriers undergo impact ionization and generate multiple excitons, MDCS can probe this process on its intrinsic timescale. Such an experiment exploits the unique capabilities of MDCS, and would constitute the first direct measurement of the controversial carrier multiplication phenomenon [6].

References

(1) Jeong, B. G.; Park, Y.-S.; Chang, J. H.; Cho, I.; Kim, J. K.; Kim, H.; Char, K.; Cho, J.; Klimov, V. I.; Park, P.; Lee, D. C.; Bae, W. K. *ACS Nano* **2016**, *10*, 9297–9305.

(2) Suzuki, T.; Singh, R.; Bayer, M.; Ludwig, A.; Wieck, A. D.; Cundiff, S. T. *Phys. Rev. Lett.* **2016**, *117*, 157402.

(3) Martin, E. W.; Cundiff, S. T. *Physical Review B* **2018**, *97*, 081301.

(4) Bredenbeck, J.; Helbing, J.; Behrendt, R.; Renner, C.; Moroder, L.; Wachtveitl, J.; Hamm, P. *The Journal of Physical Chemistry B* **2003**, *107*, 8654–8660.

(5) Xiong, W.; Laaser, J. E.; Paoprasert, P.; Franking, R. A.; Hamers, R. J.; Gopalan, P.; Zanni, M. T. *Journal of the American Chemical Society* **2009**, *131*, 18040–18041.

(6) Klimov, V. I. *Annual Review of Condensed Matter Physics* **2014**, *5*, 285–316.

APPENDICES

APPENDIX A

Optical Response Function - Hilbert Space

A.1 Interaction Representation - Wavefunction

In spectroscopic experiments where a material interacts with light, its Hamiltonian may naturally be separated into two components:

$$H(t) = H_0 + W(t) \tag{A.1}$$

where H_0 is a time-independent system Hamiltonian (which describes the system under no external perturbation), and a time-dependent interaction Hamiltonian $W(t)$ that describes the system's interaction with an applied electric field:

$$W(t) = -\mu E(t) \tag{A.2}$$

where μ is the dipole moment of the probed transition. The Schrodinger equation for the system wavefunction $|\psi(t)\rangle$ is defined:

$$\frac{d}{dt}|\psi(t)\rangle = -\frac{i}{\hbar}H|\psi(t)\rangle \tag{A.3}$$

When analyzing a two-component Hamiltonian such as in equation (A.1), it is often most natural to perform calculations in the so-called **interaction representation**. This representation is advantageous since the dynamics of the system Hamiltonian H_0 are separated from those induced by the interaction $W(t)$. We first introduce the wavefunction in the interaction picture:

$$|\psi_I(t)\rangle = e^{\frac{i}{\hbar}H_0(t-t_0)} |\psi(t)\rangle \tag{A.4}$$

Plugging this definition into the Schrodinger equation, we find:

$$\frac{d}{dt} |\psi_I(t)\rangle = -\frac{i}{\hbar} W_I(t) |\psi_I(t)\rangle \tag{A.5}$$

where we've defined the interaction representation of $W(t)$:

$$W_I(t) = e^{\frac{i}{\hbar}H_0(t-t_0)} W(t) e^{-\frac{i}{\hbar}H_0(t-t_0)} \tag{A.6}$$

The interaction Schrodinger equation (A.4) yields the formal solution:

$$|\psi_I(t)\rangle = |\psi_I(t_0)\rangle - \frac{i}{\hbar} \int_{t_0}^{t} W_I(\tau) |\psi_I(\tau)\rangle \, d\tau \tag{A.7}$$

By iteratively plugging this solution back into itself, we obtain a power series expansion solution in $W_I(t)$:

$$|\psi_I(t)\rangle = |\psi_I(t_0)\rangle + \sum_{n=1}^{\infty} \left(-\frac{i}{\hbar}\right)^n \int_{t_0}^{t} \int_{t_0}^{\tau_n} \cdots \int_{t_0}^{\tau_2} W_I(\tau_n) W(\tau_{n-1}) \ldots W(\tau_1) |\psi_I(t_0)\rangle \, d\tau_1 \ldots d\tau_{n-1} d\tau_n \tag{A.8}$$

A.2 Interaction Representation - Density Matrix

From the definition of the interaction wavefunction (A.1), the density matrix may easily be recast in the interaction representation:

$$\begin{aligned}\rho(t) &= |\psi(t)\rangle \langle\psi(t)| \\ &= e^{-\frac{i}{\hbar}H_0(t-t_0)} |\psi_I(t)\rangle \langle\psi_I(t)| e^{\frac{i}{\hbar}H_0(t-t_0)} \\ &= e^{-\frac{i}{\hbar}H_0(t-t_0)} \rho_I(t) e^{\frac{i}{\hbar}H_0(t-t_0)}\end{aligned} \tag{A.9}$$

Recalling the Heisenberg equation of motion for $\rho(t)$:

$$\frac{d}{dt}\rho(t) = -\frac{i}{\hbar}[H(t), \rho(t)] \tag{A.10}$$

where $[A, B] = AB - BA$ is the commutator between two operators A and B. This may similarly be recast in the interaction representation as:

$$\frac{d}{dt}\rho_I(t) = -\frac{i}{\hbar}[W_I(t), \rho_I(t)] \tag{A.11}$$

which yields a power series expansion solution analogous to (A.8):

$$\begin{aligned}\rho_I(t) = \rho_I(t_0) + \sum_{n=1}^{\infty} \left(-\frac{i}{\hbar}\right)^n \int_{t_0}^{t}\int_{t_0}^{\tau_n}\cdots\int_{t_0}^{\tau_2} \\ [W_I(\tau_n), [W_I(\tau_{n-1}), \ldots [W_I(\tau_1), \rho_I(t_0)]\ldots]]\, d\tau_1 \ldots d\tau_{n-1} d\tau_n \\ = \rho(t_0) + \sum_{n=1}^{\infty} \left(-\frac{i}{\hbar}\right)^n \int_{t_0}^{t}\int_{t_0}^{\tau_n}\cdots\int_{t_0}^{\tau_2} E(\tau_n)E(\tau_{n-1})\ldots E(\tau_1) \\ [\mu_I(\tau_n), [\mu_I(\tau_{n-1}), \ldots [\mu_I(\tau_1), \rho(t_0)]\ldots]]\, d\tau_1 \ldots d\tau_{n-1} d\tau_n\end{aligned} \tag{A.12}$$

where we've also defined the interaction representation of the dipole operator μ:

$$\mu_I(t) = e^{\frac{i}{\hbar}H_0(t-t_0)}\mu e^{-\frac{i}{\hbar}H_0(t-t_0)} \tag{A.13}$$

We can easily recover the Schrodinger representation density matrix:

$$\begin{aligned}\rho(t) &= e^{-\frac{i}{\hbar}H_0(t-t_0)}\rho_I(t)e^{\frac{i}{\hbar}H_0(t-t_0)} \\ &= \rho(t_0) + \sum_{n=1}^{\infty}\left(-\frac{i}{\hbar}\right)^n \int_{t_0}^{t}\int_{t_0}^{\tau_n}\cdots\int_{t_0}^{\tau_2} E(\tau_n)E(\tau_{n-1})\ldots E(\tau_1) \\ &\qquad e^{-\frac{i}{\hbar}H_0(t-t_0)}\left[\mu_I(\tau_n),\left[\mu_I(\tau_{n-1}),\ldots\left[\mu_I(\tau_1),\rho(t_0)\right]\ldots\right]\right]e^{\frac{i}{\hbar}H_0(t-t_0)}d\tau_1\ldots d\tau_{n-1}d\tau_n\end{aligned} \tag{A.14}$$

A.3 Nonlinear Polarization

The nonlinear polarization is defined by:

$$P(t) = \mathrm{Tr}\left[\mu\rho(t)\right] = P^{(0)}(t) + \sum_{n=1}^{\infty}P^{(n)}(t) \tag{A.15}$$

where we've defined the zeroth order polarization $P^{(0)}(t) = \mathrm{Tr}\left[\mu\rho(t_0)\right]$ and the power series expansion terms:

$$\begin{aligned}P^{(n)}(t) &= \left(-\frac{i}{\hbar}\right)^n \int_{t_0}^{t}\int_{t_0}^{\tau_n}\cdots\int_{t_0}^{\tau_2} E(\tau_n)E(\tau_{n-1})\ldots E(\tau_1) \\ &\qquad \mathrm{Tr}\left[\mu e^{-\frac{i}{\hbar}H_0(t-t_0)}\left[\mu_I(\tau_n),\left[\mu_I(\tau_{n-1}),\ldots\left[\mu_I(\tau_1),\rho(t_0)\right]\ldots\right]\right]e^{\frac{i}{\hbar}H_0(t-t_0)}\right] \\ &\qquad\qquad d\tau_1\ldots d\tau_{n-1}d\tau_n \\ &= \int_{t_0}^{t}\int_{t_0}^{\tau_n}\cdots\int_{t_0}^{\tau_2} S^{(n)}(\tau_2-\tau_1,\ldots,\tau_n-\tau_{n-1},t-\tau_n) \\ &\qquad E(\tau_n)E(\tau_{n-1})\ldots E(\tau_1)d\tau_1\ldots d\tau_{n-1}d\tau_n\end{aligned} \tag{A.16}$$

where $S^{(n)}$ is the nth order optical response function.

APPENDIX B

Optical Response Function - Liouville Space

In this Appendix equations describing the optical response of a system that incorporate nuclear degrees of freedom are derived. Our treatment follows that of Mukamel's tome [1], but is more explicit and direct[1].

B.1 Liouville Space Dynamics

Recall the time-dependent Schrodinger equation, which is the equation of motion of our system wavefunction $|\psi(t)\rangle$:

$$\frac{\partial |\psi(t)\rangle}{\partial t} = -\frac{i}{\hbar} H |\psi(t)\rangle \qquad \frac{\partial \langle\psi(t)|}{\partial t} = \frac{i}{\hbar} \langle\psi(t)| H \tag{B.1}$$

Using this equation of motion, we can calculate the density matrix equation of motion:

$$\begin{aligned} \frac{\partial \rho}{\partial t} &= \left(\frac{\partial |\psi(t)\rangle}{\partial t}\right) \langle\psi(t)| + |\psi(t)\rangle \left(\frac{\partial \langle\psi(t)|}{\partial t}\right) \\ &= -\frac{i}{\hbar} H |\psi(t)\rangle \langle\psi(t)| + \frac{i}{\hbar} |\psi(t)\rangle \langle\psi(t)| H \\ &= -\frac{i}{\hbar} [H, \rho] \end{aligned} \tag{B.2}$$

[1] In this Appendix we use the notation of Mukamel [1] to facilitate correspondence, but the results may be translated into the notation of this thesis by the replacements $t_1 \to \tau$, $t_2 \to T$, and $t_3 \to t$.

This equation of motion for the density matrix is known as the Heisenberg equation or quantum Liouville equation (in analogy to the classical Liouville equation). Hereafter we will refer to it simply as the Liouville equation.

B.1.1 Liouville Space Notation

Hilbert space is spanned by wavefunctions, whose dynamics we calculate using the Schrodinger equation. The density matrix, on the other hand, spans a different space called Liouville space and we calculate the dynamics using the Liouville equation. It will thus be beneficial to recast our equations into a notation more amenable to manipulating the density matrix.

Consider the system density matrix ρ expressed in an arbitrary basis $|j\rangle\langle k|$:

$$\rho = \sum_{j,k} \rho_{jk} |j\rangle\langle k| \tag{B.3}$$

We now introduce the notation $|j\rangle\langle k| \rightarrow |jk\rangle\rangle$ and $\rho \rightarrow |\rho\rangle\rangle$:

$$\rho = \sum_{j,k} \rho_{jk} |j\rangle\langle k| \quad \rightarrow \quad |\rho\rangle\rangle = \sum_{j,k} \rho_{jk} |jk\rangle\rangle \tag{B.4}$$

where the double-ket (and also double-bra later on) will in general represent Liouville space vectors, which are equivalent to operators in Hilbert space. For example, an operator A will be written in Liouville space notation as:

$$A = \sum_{j,k} A_{jk} |j\rangle\langle k| \quad \rightarrow \quad |A\rangle\rangle = \sum_{j,k} A_{jk} |jk\rangle\rangle \tag{B.5}$$

The double-bra is defined as the Hermitian conjugate of a double-ket:

$$\langle\langle jk| = (|jk\rangle\rangle)^\dagger = (|j\rangle\langle k|)^\dagger = |k\rangle\langle j| \tag{B.6}$$

Just as in Hilbert space, we define inner products of Liouville space vectors. Their equivalent operations in Hilbert space are defined by a trace operation:

$$\langle\langle B|A\rangle\rangle = \mathrm{Tr}\left[B^\dagger A\right]$$

To take the analogy further, Liouville space vectors obey two very important properties shared by Hilbert space vectors:

1. Orthonormality:

$$\langle\langle jk|mn\rangle\rangle = \mathrm{Tr}\left[|k\rangle\langle j\,|\,m\rangle\langle n|\right] = \delta_{kn}\delta_{jm} \tag{B.7}$$

2. Completeness:

$$\begin{aligned}\langle\langle jk|A\rangle\rangle &= \mathrm{Tr}\left[|k\rangle\langle j|\,A\right] = \langle j\,|\,A\,|\,k\rangle = A_{jk}\\ \rightarrow |A\rangle\rangle &= \sum_{j,k}|jk\rangle\rangle A_{jk} = \sum_{j,k}|jk\rangle\rangle\langle\langle jk|A\rangle\rangle\end{aligned} \tag{B.8}$$

The above equation thus gives the completeness condition:

$$1 = \sum_{j,k}|jk\rangle\rangle\langle\langle jk| \tag{B.9}$$

Lastly, we define operators in Liouville space (which are often referred to as superoperators or tetradic operators). An arbitrary operator $\mathcal{F}$ is defined by:

$$\begin{aligned}\mathcal{F} &= \sum_{j,k,m,n}|jk\rangle\rangle\langle\langle jk|\,\mathcal{F}\,|mn\rangle\rangle\langle\langle mn|\\ &= \sum_{j,k,m,n}\mathcal{F}_{jk,mn}\,|jk\rangle\rangle\langle\langle mn|\end{aligned} \tag{B.10}$$

where its matrix elements are defined by four indices:

$$\mathcal{F}_{jk,mn} = \langle\langle jk| \mathcal{F} |mn\rangle\rangle \tag{B.11}$$

B.1.2 The Liouville Operator

Now that we've defined superoperators, we now add one more layer of abstraction to the Liouville equation:

$$\frac{\partial \rho}{\partial t} = -\frac{i}{\hbar}[H, \rho] = -\frac{i}{\hbar}\mathcal{L}\rho$$

where we've defined the superoperator $\mathcal{L}$, which we call the Liouville operator. In general, it acts on an arbitrary Liouville space vector $|A\rangle\rangle$ (Hilbert space operator A) with the commutator operation involving the Hamiltonian:

$$\mathcal{L}|A\rangle\rangle = \mathcal{L}A = [H, A] \tag{B.12}$$

As good practice, we can calculate its matrix elements:

$$\begin{aligned}
\mathcal{L}_{jk,mn} &= \langle\langle jk|\mathcal{L}|mn\rangle\rangle \\
&= \mathrm{Tr}\left[|k\rangle \langle j| \mathcal{L} |m\rangle \langle n|\right] \\
&= \mathrm{Tr}\left[|k\rangle \langle j \,|\, H \,|\, m\rangle \langle n| - |k\rangle \langle j \,|\, m\rangle \langle n| \, H\right] \\
&= H_{jm}\delta_{kn} - H_{nk}\delta_{jm}
\end{aligned} \tag{B.13}$$

From its role in the Liouville equation, it is no surprise that the Liouville operator will be central to calculating dynamics in Liouville space.

B.1.3 Propagators in Liouville Space

Now recall the propagator for a wavefunction $U(t, t_0)$:

$$|\psi(t)\rangle = U(t, t_0)\,|\psi(t_0)\rangle \tag{B.14}$$

which is defined perturbatively for a time-dependent Hamiltonian:

$$\begin{aligned} U(t, t_0) &= 1 + \sum_{n=1}^{\infty} \left(-\frac{i}{\hbar}\right)^n \int_{t_0}^{t} \int_{t_0}^{\tau_n} \cdots \int_{t_0}^{\tau_2} H(\tau_n) H(\tau_{n-1}) \ldots H(\tau_1) d\tau_1 \ldots d\tau_{n-1} d\tau_n \\ &= \exp_+ \left[-\frac{i}{\hbar} \int_{t_0}^{t} H(\tau) d\tau\right] \end{aligned} \tag{B.15}$$

We may likewise define a Liouville space propagator $\mathcal{U}(t, t_0)$, which like its Hilbert space counterpart evolves the density matrix in time:

$$\rho(t) = \mathcal{U}(t, t_0)\rho(t_0) \tag{B.16}$$

Plugging this expression into the Liouville equation gives its equation of motion:

$$\begin{aligned} &\frac{\partial}{\partial t}\mathcal{U}(t, t_0)\rho(t_0) = -\frac{i}{\hbar}\mathcal{L}(t)\mathcal{U}(t, t_0)\rho(t_0) \\ &\rightarrow \frac{\partial \mathcal{U}(t, t_0)}{\partial t} = -\frac{i}{\hbar}\mathcal{L}(t)\mathcal{U}(t, t_0) \end{aligned} \tag{B.17}$$

By inspection, we can immediately write down the action of $\mathcal{U}(t, t_0)$ as:

$$\mathcal{U}(t, t_0)\rho(t_0) = U(t, t_0)\rho(t_0)U^{\dagger}(t, t_0) \tag{B.18}$$

However, we often require a more abstract form of $\mathcal{U}(t, t_0)$ by itself. To that end, we can write down a formal solution to its equation of motion:

$$\mathcal{U}(t, t_0) = 1 - \frac{i}{\hbar} \int_{t_0}^{t} \mathcal{L}(\tau)\mathcal{U}(\tau, t_0)d\tau \tag{B.19}$$

By the same procedure as for the Hilbert space propagator, we can expand this expression perturbatively as a time-ordered exponential:

$$\mathcal{U}(t, t_0) = 1 + \sum_{n-1}^{\infty} \left(-\frac{i}{\hbar}\right)^n \int_{t_0}^{t} \int_{t_0}^{\tau_n} \cdots \int_{t_0}^{\tau_2} \mathcal{L}(\tau_n)\mathcal{L}(\tau_{n-1}) \ldots \mathcal{L}(\tau_1)d\tau_1 \ldots d\tau_{n-1}d\tau_n \tag{B.20}$$

It's action on $\rho(t_0)$ is given by:

$$\mathcal{U}(t, t_0)\rho(t_0) = \rho(t_0) + \sum_{n-1}^{\infty} \left(-\frac{i}{\hbar}\right)^n \int_{t_0}^{t} \int_{t_0}^{\tau_n} \cdots \int_{t_0}^{\tau_2} \\ [H(\tau_n), \ldots [H(\tau_2), [H(\tau_1), \rho(t_0)]] \ldots] \, d\tau_1 \ldots d\tau_{n-1}d\tau_n \tag{B.21}$$

B.1.4 Interaction Picture

In the context of spectroscopy, the physical problem usually boils down to a system (atom, molecule, crystal etc.) interacting with an incident light field. Usually, the system itself has a well-defined Hamiltonian, while the total Hamiltonian consisting of the system coupled to the incident light is intractable. We therefore often work in the interaction picture, which partitions the Hamiltonian into two parts:

$$H = H_0(t) + H_{int}(t) \tag{B.22}$$

where $H_0(t)$ is some system and $H_{int}(t)$ is its interaction with an external force. It is straightforward to see that the Liouville operator is similarly partitioned:

$$\mathcal{L} = \mathcal{L}_0(t) + \mathcal{L}_{int}(t) \tag{B.23}$$

$$\mathcal{L}_0(t)A = [H_0(t), A] \qquad \mathcal{L}_{int}(t)A = [H_{int}(t), A] \tag{B.24}$$

Certain quantities will be convenient to redefine in the interaction picture:

$$\mathcal{U}_0(t, t_0) = \exp_+ \left[-\frac{i}{\hbar} \int_{t_0}^{t} \mathcal{L}_0(\tau) d\tau \right] \tag{B.25}$$

$$|\psi(t)\rangle\rangle = \mathcal{U}_0(t, t_0) \, |\psi_I(t)\rangle\rangle \tag{B.26}$$

$$|\psi_I(t)\rangle\rangle = \mathcal{U}_I(t, t_0) \, |\psi_I(t_0)\rangle\rangle \tag{B.27}$$

Plugging in the above definition of $|\psi(t)\rangle\rangle$ into the Liouville equation, we can derive an equivalent equation of motion for $|\psi_I(t)\rangle\rangle$:

$$\begin{aligned}
&\frac{\partial \, |\psi(t)\rangle\rangle}{\partial t} = -\frac{i}{\hbar} \left[\mathcal{L}_0(t) + \mathcal{L}_{int}(t) \right] |\psi(t)\rangle\rangle \\
&\rightarrow \frac{\partial \mathcal{U}_0(t, t_0)}{\partial t} \, |\psi_I(t)\rangle\rangle + \mathcal{U}_0(t, t_0) \frac{\partial \, |\psi_I(t)\rangle\rangle}{\partial t} = -\frac{i}{\hbar} \left[\mathcal{L}_0(t) + \mathcal{L}_{int}(t) \right] \mathcal{U}_0(t, t_0) \, |\psi_I(t)\rangle\rangle \\
&\rightarrow \mathcal{U}_0(t, t_0) \frac{\partial \, |\psi_I(t)\rangle\rangle}{\partial t} = -\frac{i}{\hbar} \mathcal{L}_{int}(t) \mathcal{U}_0(t, t_0) \, |\psi_I(t)\rangle\rangle \\
&\rightarrow \frac{\partial \, |\psi_I(t)\rangle\rangle}{\partial t} = -\frac{i}{\hbar} \mathcal{L}^I_{int}(t) \, |\psi_I(t)\rangle\rangle
\end{aligned} \tag{B.28}$$

with the solution:

$$\begin{aligned}
|\psi_I(t)\rangle\rangle &= \exp_+ \left[-\frac{i}{\hbar} \int_{t_0}^{t} \mathcal{L}^I_{int}(\tau) d\tau \right] |\psi_I(t)\rangle\rangle \\
&= \mathcal{U}^I(t, t_0) \, |\psi_I(t)\rangle\rangle
\end{aligned} \tag{B.29}$$

where we've defined the interaction picture Liouville operator:

$$\mathcal{L}_{int}^{I}(\tau) = \mathcal{U}_0^{\dagger}(\tau, t_0)\mathcal{L}_{int}(\tau)\mathcal{U}_0(\tau, t_0) \tag{B.30}$$

Explicitly, the interaction propagator can be calculated as:

$$\begin{aligned}
\mathcal{U}_I(t, t_0) &= \exp_+\left[-\frac{i}{\hbar}\int_{t_0}^{t}\mathcal{L}_{int}^{I}(\tau)d\tau\right] \\
&= 1 + \sum_{n-1}^{\infty}\left(-\frac{i}{\hbar}\right)^n \int_{t_0}^{t}\int_{t_0}^{\tau_n} .. \int_{t_0}^{\tau_2} \mathcal{L}_{int}^{I}(\tau_n)\mathcal{L}_{int}^{I}(\tau_{n-1})..\mathcal{L}_{int}^{I}(\tau_1)d\tau_1..d\tau_{n-1}d\tau_n \\
&= 1 + \sum_{n-1}^{\infty}\left(-\frac{i}{\hbar}\right)^n \int_{t_0}^{t}\int_{t_0}^{\tau_n} .. \int_{t_0}^{\tau_2} \\
&\qquad \mathcal{U}_0^{\dagger}(\tau_n, t_0)\mathcal{L}_{int}(\tau_n)\mathcal{U}_0(\tau_n, t_0)\mathcal{U}_0^{\dagger}(\tau_{n-1}, t_0)\mathcal{L}_{int}(\tau_{n-1})\mathcal{U}_0(\tau_{n-1}, t_0)..\mathcal{L}_{int}^{I}(\tau_1) \\
&\qquad\qquad d\tau_1 \ldots d\tau_{n-1}d\tau_n \\
&= 1 + \sum_{n-1}^{\infty}\left(-\frac{i}{\hbar}\right)^n \int_{t_0}^{t}\int_{t_0}^{\tau_n} .. \int_{t_0}^{\tau_2} \\
&\qquad \mathcal{U}_0^{\dagger}(\tau_n, t_0)\mathcal{L}_{int}(\tau_n)\mathcal{U}_0(\tau_n, \tau_{n-1})\mathcal{L}_{int}(\tau_{n-1})..\mathcal{L}_{int}(\tau_1)\mathcal{U}_0(\tau_1, t_0)d\tau_1..d\tau_{n-1}d\tau_n
\end{aligned}$$

Finally, we combine the propagator expressions of $|\psi(t)\rangle\rangle$ and $|\psi_I(t)\rangle\rangle$ to find:

$$|\psi(t)\rangle\rangle = \mathcal{U}_0(t, t_0)\,|\psi_I(t)\rangle\rangle = \mathcal{U}_0(t, t_0)\mathcal{U}_I(t, t_0)\,|\psi(t_0)\rangle\rangle \tag{B.31}$$

where the total propagator may now be expressed as:

$$\begin{aligned}
\mathcal{U}(t, t_0) &= \mathcal{U}_0(t, t_0)\mathcal{U}_I(t, t_0) \\
&= \mathcal{U}_0(t, t_0) + \sum_{n-1}^{\infty}\left(-\frac{i}{\hbar}\right)^n \int_{t_0}^{t}\int_{t_0}^{\tau_n} .. \int_{t_0}^{\tau_2} \\
&\qquad \mathcal{U}_0(t, \tau_n)\mathcal{L}_{int}(\tau_n)\mathcal{U}_0(\tau_n, \tau_{n-1})\mathcal{L}_{int}(\tau_{n-1})..\mathcal{L}_{int}(\tau_1)\mathcal{U}_0(\tau_1, t_0)d\tau_1..d\tau_{n-1}d\tau_n
\end{aligned} \tag{B.32}$$

If this pattern of alternating propagators and interaction Liouville operators seems familiar, that is because applying this expression for $\mathcal{U}(t,t_0)$ to $\rho(t_0)$ recovers the Schrodinger representation of $\rho(t)$ given by equation (A.14). Each perturbation term thus retains the intuitive interpretation of alternating interaction and free-propagation of the system density matrix described in Chapter III.

B.2 Nonlinear Polarization

Our goal is now to re-derive the nonlinear polarization from a Liouville space approach. The resultant equations are more general, and, most importantly, more amenable to incorporating nuclear degrees of freedom.

B.2.1 Perturbative Expansion of the Polarization

Consider the following Hamiltonian of a system:

$$H_T(t) = H + H_{int}(t) \tag{B.33}$$

where the total Hamiltonian $H_T(t)$ is partitioned into the system Hamiltonian H and a perturbation $H_{int}(t)$ that defines the system's interaction with an incident light field $E(\mathbf{r},t)$:

$$H_{int}(t) = -E(\mathbf{r},t)V \tag{B.34}$$

where V is the dipole operator. Note that because we seldom consider $H_T(t)$, we now denote the system Hamiltonian H (which we called H_0 in the previous section). Hereafter we also assume a time-independent system Hamiltonian, which is why we

drop the time argument of H. We define the Liouville space operators:

$$\mathcal{L}A = [H, A] \tag{B.35}$$

$$\begin{aligned}\mathcal{L}_{int}(t)A &= [H_{int}(t), A] \\ &= -E(\mathbf{r}, t)\mathcal{V}A\end{aligned} \tag{B.36}$$

$$\mathcal{V}A = [V, A] \tag{B.37}$$

The propagators in the equations above are often replaced by Green functions, which differ by a Heaviside step function:

$$\mathcal{G}(\tau) = \theta(\tau) \exp\left(-\frac{i}{\hbar}\mathcal{L}\tau\right) = \theta(\tau)\mathcal{U}(\tau, 0) \tag{B.38}$$

The step function enforces a specific direction of time-propagation, and thus there is also a set of opposite time-propagation Green functions which we need not consider here.

Using the total propagator derived above, we can express the density matrix as the following:

$$\begin{aligned}\rho(t) = \rho(t_0) + \sum_{n-1}^{\infty}\left(-\frac{i}{\hbar}\right)^n \int_{t_0}^{t}\int_{t_0}^{\tau_n}\cdots\int_{t_0}^{\tau_2} \\ \mathcal{G}(t-\tau_n)\mathcal{L}_{int}(\tau_n)\mathcal{G}(\tau_n-\tau_{n-1})\mathcal{L}_{int}(\tau_{n-1})\ldots\mathcal{L}_{int}(\tau_1)\mathcal{G}(\tau_1-t_0)\rho(t_0) \\ d\tau_1\ldots d\tau_{n-1}d\tau_n \\ = \rho(t_0) + \sum_{n-1}^{\infty}\left(\frac{i}{\hbar}\right)^n \int_{t_0}^{t}\int_{t_0}^{\tau_n}\cdots\int_{t_0}^{\tau_2} \\ \mathcal{G}(t-\tau_n)\mathcal{V}\mathcal{G}(\tau_n-\tau_{n-1})\mathcal{V}\ldots\mathcal{G}(\tau_2-\tau_1)\mathcal{V}\rho(t_0)E(\mathbf{r},\tau_n)E(\mathbf{r}),\tau_{n-1})\ldots E(\mathbf{r},\tau_1) \\ d\tau_1\ldots d\tau_{n-1}d\tau_n\end{aligned} \tag{B.39}$$

In going from the first to second line, we have made one assumption about the nature of the initial density matrix that has not yet been mentioned. The assumption is that the initial density matrix is at thermal equilibrium, which corresponds to the equilibrium canonical density matrix:

$$\rho(t_0) = \frac{\exp(-\beta H)}{\mathrm{Tr}\left[\exp(-\beta H)\right]} \tag{B.40}$$

Because this density matrix is a function of the Hamiltonian, it does not change after being acted upon by $\mathcal{G}$. This is simply a consequence of commuting with the propagator, which is also a function of the Hamiltonian.

For time-resolved spectroscopy, it is convenient to make a change in time variables:

$$t_1 = \tau_2 - \tau_1, \quad t_2 = \tau_3 - \tau_2, \ldots t_n = t - \tau_n \tag{B.41}$$

which recasts the density matrix as:

$$\rho(t) = \rho(t_0) + \sum_{i=1}^{\infty} \left(\frac{i}{\hbar}\right)^n \int_0^\infty \int_0^\infty \cdots \int_0^\infty \mathcal{G}(t_n)\mathcal{V}\mathcal{G}(t_{n-1})\mathcal{V} \ldots \mathcal{G}(t_1)\mathcal{V}\rho(\text{-}\infty)$$
$$E(\mathbf{r}, t - t_n)E(\mathbf{r}, t - t_n - t_{n-1}) \ldots E(\mathbf{r}, t - t_n - t_{n-1} \cdots - t_1)dt_1 \ldots dt_{n-1}dt_n \tag{B.42}$$

The system polarization, which is the observable we detect via emitted radiation, is given by the expectation value of the dipole operator:

$$P(\mathbf{r}, t) = \mathrm{Tr}\left[V\rho(t)\right] = \langle\langle V|\rho(t)\rangle\rangle \tag{B.43}$$

By plugging in the above perturbative expansion of the density matrix, we obtain a

similar perturbative expansion of the polarization:

$$\begin{aligned}
P(\mathbf{r},t) &= \langle\langle V|\rho(t)\rangle\rangle \\
&= \langle\langle V|\rho(t_0)\rangle\rangle + \sum_{i=1}^{\infty}\left(\frac{i}{\hbar}\right)^n \int_0^\infty \int_0^\infty .. \int_0^\infty \langle\langle V|\mathcal{G}(t_n)\mathcal{V}\mathcal{G}(t_{n-1})..\mathcal{G}(t_1)\mathcal{V}|\rho(\text{-}\infty)\rangle\rangle \\
&\qquad E(\mathbf{r},t-t_n)E(\mathbf{r},t-t_n-t_{n-1})\ldots E(\mathbf{r},t-t_n-t_{n-1}\cdots-t_1)dt_1..dt_{n-1}dt_n \\
&= \langle\langle V|\rho(t_0)\rangle\rangle + \sum_{i=1}^{\infty}\int_0^\infty \int_0^\infty .. \int_0^\infty S^{(n)}(t_n,t_{n-1},..,t_1) \\
&\qquad E(\mathbf{r},t-t_n)E(\mathbf{r},t-t_n-t_{n-1})\ldots E(\mathbf{r},t-t_n-t_{n-1}\cdots-t_1)dt_1..dt_{n-1}dt_n
\end{aligned} \tag{B.44}$$

To emphasize, we have defined the nth order response function as:

$$S^{(n)}(t_n,t_{n-1},\ldots,t_1) = \left(\frac{i}{\hbar}\right)^n \langle\langle V|\mathcal{G}(t_n)\mathcal{V}\mathcal{G}(t_{n-1})\mathcal{V}\ldots\mathcal{G}(t_1)\mathcal{V}|\rho(\text{-}\infty)\rangle\rangle \tag{B.45}$$

B.2.2 Linear Response

The linear response function is given by:

$$S^{(1)}(t_1) = \frac{i}{\hbar}\langle\langle V|\mathcal{G}(t_1)\mathcal{V}|\rho(\text{-}\infty)\rangle\rangle \tag{B.46}$$

or in Hilbert space:

$$\begin{aligned}
S^{(1)}(t_1) &= \frac{i}{\hbar}\mathrm{Tr}\left[V\mathcal{G}(t_1)\mathcal{V}\rho(\text{-}\infty)\right] \\
&= \frac{i}{\hbar}\theta(t_1)\mathrm{Tr}\left[V\mathcal{U}(t_1)\left(V\rho(\text{-}\infty)-\rho(\text{-}\infty)V\right)\right] \\
&= \frac{i}{\hbar}\theta(t_1)\mathrm{Tr}\left[V\left(U(t_1)V\rho(\text{-}\infty)U^\dagger(t_1)-U(t_1)\rho(\text{-}\infty)VU^\dagger(t_1)\right)\right] \\
&= \frac{i}{\hbar}\theta(t_1)\mathrm{Tr}\left[V(t_1)V(0)\rho(\text{-}\infty)-V(0)V(t_1)\rho(\text{-}\infty)\right] \\
&= \frac{i}{\hbar}\theta(t_1)[J(t_1)-J^*(t_1)]
\end{aligned} \tag{B.47}$$

where we've defined the two quantum pathways:

$$J(t_1) = \mathrm{Tr}\left[V(t_1)V(0)\rho(\text{-}\infty)\right] \tag{B.48a}$$

$$J^*(t_1) = \mathrm{Tr}\left[V(0)V(t_1)\rho(\text{-}\infty)\right] \tag{B.48b}$$

B.2.3 Third-Order Response

The third-order response function is given by:

$$S^{(3)}(t_1,t_2,t_3) = \left(\frac{i}{\hbar}\right)^3 \langle\langle V|\mathcal{G}(t_3)\mathcal{V}\mathcal{G}(t_2)\mathcal{V}\mathcal{G}(t_1)\mathcal{V}|\rho(\text{-}\infty)\rangle\rangle \tag{B.49}$$

or in Hilbert space:

$$\begin{aligned}
S^{(3)}(t_1,t_2,t_3) &= \left(\frac{i}{\hbar}\right)^3 \mathrm{Tr}\left[V\mathcal{G}(t_3)\mathcal{V}\mathcal{G}(t_2)\mathcal{V}\mathcal{G}(t_1)\mathcal{V}\rho(\text{-}\infty)\right] \\
&= \left(\frac{i}{\hbar}\right)^3 \theta(t_1)\theta(t_2)\theta(t_3)\mathrm{Tr}\left[V\mathcal{U}(t_3)\mathcal{V}\mathcal{U}(t_2)\mathcal{V}\mathcal{U}(t_1)\mathcal{V}\rho(\text{-}\infty)\right] \\
&= \left(\frac{i}{\hbar}\right)^3 \theta(t_1)\theta(t_2)\theta(t_3)\mathrm{Tr}\left[V\mathcal{U}(t_3)\mathcal{V}\mathcal{U}(t_2)\mathcal{V}\mathcal{U}(t_1)(V\rho(\text{-}\infty) - \rho(\text{-}\infty)V)\right] \\
&= \left(\frac{i}{\hbar}\right)^3 \theta(t_1)\theta(t_2)\theta(t_3) \\
&\qquad\qquad \mathrm{Tr}\left[[[[V(t_3+t_2+t_1), V(t_2+t_1)], V(t_1)], V(0)]\,\rho(\text{-}\infty)\right] \\
&= \left(\frac{i}{\hbar}\right)^3 \theta(t_1)\theta(t_2)\theta(t_3)\sum_{\alpha=1}^{4}\left[R_\alpha(t_1,t_2,t_3) - R_\alpha^*(t_1,t_2,t_3)\right]
\end{aligned} \tag{B.50}$$

where there are 8 third-order pathways defined by:

$$R_1(t_1,t_2,t_3) = \mathrm{Tr}\left[V(t_1)V(t_1+t_2)V(t_1+t_2)V(t_1+t_2+t_3)V(0)\rho(\text{-}\infty)\right] \tag{B.51}$$

$$R_2(t_1,t_2,t_3) = \mathrm{Tr}\left[V(0)V(t_1+t_2)V(t_1+t_2)V(t_1+t_2+t_3)V(t_1)\rho(\text{-}\infty)\right] \tag{B.52}$$

$$R_3(t_1,t_2,t_3) = \mathrm{Tr}\left[V(0)V(t_1)V(t_1+t_2+t_3)V(t_1+t_2)V(t_1+t_2)\rho(\text{-}\infty)\right] \tag{B.53}$$

$$R_4(t_1,t_2,t_3) = \mathrm{Tr}\left[V(t_1+t_2+t_3)V(t_1+t_2)V(t_1+t_2)V(t_1)V(0)\rho(\text{-}\infty)\right] \tag{B.54}$$

B.3 Incorporating Nuclear Degrees of Freedom

In reality the electronic excitations that we probe often cannot be considered isolated level systems. The nuclei these electrons originate from have dynamics of their own, which often modulate the electronic dynamics in a non-negligible manner.

Consider a system with two electronic states $|g\rangle$ and $|e\rangle$, representing the ground and excited state respectively, which are coupled to nuclear degrees of freedom $\mathbf{q}$. The system Hamiltonian may be written:

$$\begin{aligned} H &= |g\rangle \left[T(\mathbf{q}) + W_g(\mathbf{q})\right] \langle g| + |e\rangle \left[\hbar\omega_{eg}^0 + T(\mathbf{q}) + W_e(\mathbf{q})\right] \langle e| \\ &= |g\rangle H_g(\mathbf{q}) \langle g| + |e\rangle H_e(\mathbf{q}) \langle e| \end{aligned} \tag{B.55}$$

where $T(\mathbf{q})$ is the nuclear kinetic energy, $W_g(\mathbf{q})$ and $W_e(\mathbf{q})$ are the ground and excited state adiabatic potentials for each electronic state (i.e. the dependence of the electronic energy on the nuclear configuration), and $\hbar\omega_{eg}^0$ is the energy gap in the absence of coupling to nuclear motion.

The transition dipole operator is:

$$V = V_{ge}(\mathbf{q}) |g\rangle \langle e| + V_{eg}(\mathbf{q}) |e\rangle \langle g| \tag{B.56}$$

We will make the Condon approximation, which assumes the nuclear dependence of the dipole operator is negligible[2]:

$$V \approx V_{ge} |g\rangle \langle e| + V_{eg} |e\rangle \langle g| \quad \text{(Condon Approximation)} \tag{B.57}$$

[2]This corresponds to expanding $V_{eg}(\mathbf{q})$ and $V_{ge}(\mathbf{q})$ as Taylor series and retaining only the first term.

Recalling the linear response function:

$$S^{(1)}(t_1) = \frac{i}{\hbar}\langle\langle V|\mathcal{G}(t_1)\mathcal{V}|\rho(\text{-}\infty)\rangle\rangle \tag{B.58}$$

We can project the equation into the $\{|g\rangle, |e\rangle\}$ basis:

$$\begin{aligned} S^{(1)}(t_1) &= \frac{i}{\hbar}\sum_{i,j,m,n}\langle\langle V|ij\rangle\rangle\langle\langle ij|\mathcal{G}(t_1)|mn\rangle\rangle\langle\langle mn|\mathcal{V}|\rho(\text{-}\infty)\rangle\rangle \\ &= \frac{i}{\hbar}\sum_{m,n}(\langle\langle V|eg\rangle\rangle\langle\langle eg|\mathcal{G}(t_1)|mn\rangle\rangle + \langle\langle V|ge\rangle\rangle\langle\langle ge|\mathcal{G}(t_1)|mn\rangle\rangle)\langle\langle mn|\mathcal{V}|\rho(\text{-}\infty)\rangle\rangle \end{aligned} \tag{B.59}$$

where to get from the first to second line, we used the fact that $\langle\langle V|ij\rangle\rangle$ is non-zero only if $i \neq j$. We then reach our final result:

$$\begin{aligned} S^{(1)}(t_1) &= \frac{i}{\hbar}\sum_{m,n}\langle\langle V|eg\rangle\rangle\langle\langle eg|\mathcal{G}(t_1)|mn\rangle\rangle\langle\langle mn|\mathcal{V}|\rho(\text{-}\infty)\rangle\rangle\ldots \\ &\qquad + \langle\langle V|ge\rangle\rangle\langle\langle ge|\mathcal{G}(t_1)|mn\rangle\rangle\langle\langle mn|\mathcal{V}|\rho(\text{-}\infty)\rangle\rangle \\ &= \frac{i}{\hbar}\sum_{m}\langle\langle V|eg\rangle\rangle\langle\langle eg|\mathcal{G}(t_1)|mg\rangle\rangle\langle\langle mg|\mathcal{V}|\rho(\text{-}\infty)\rangle\rangle\ldots \\ &\qquad + \langle\langle V|ge\rangle\rangle\langle\langle ge|\mathcal{G}(t_1)|me\rangle\rangle\langle\langle me|\mathcal{V}|\rho(\text{-}\infty)\rangle\rangle \\ &= \frac{i}{\hbar}[\langle\langle V|eg\rangle\rangle\langle\langle eg|\mathcal{G}(t_1)|eg\rangle\rangle\langle\langle eg|\mathcal{V}|\rho(\text{-}\infty)\rangle\rangle\ldots \\ &\qquad + \langle\langle V|ge\rangle\rangle\langle\langle ge|\mathcal{G}(t_1)|ge\rangle\rangle\langle\langle ge|\mathcal{V}|\rho(\text{-}\infty)\rangle\rangle] \\ &= \frac{i}{\hbar}\langle\langle V_{eg}|\mathcal{G}_{eg}(t_1)|V_{eg}\rho_g\rangle\rangle - \frac{i}{\hbar}\langle\langle V_{ge}|\mathcal{G}_{ge}(t_1)|\rho_g V_{ge}\rangle\rangle \end{aligned} \tag{B.60}$$

where we go from the first to second line by using that $\langle\langle ij|\mathcal{G}(t_1)|mn\rangle\rangle$ vanishes for $n \neq j$ and go from the second to third line by using that $\langle\langle ij|\mathcal{V}|\rho(\text{-}\infty)\rangle\rangle$ vanishes for $i = j$ (since $\rho(\text{-}\infty) = |g\rangle\,\rho_g\,\langle g|$). These relations can be verified by explicitly calculating the traces involved in each term. We also note that $\mathcal{G}_{ij}(t)$ is shorthand notation for $\mathcal{G}_{ij,ij}(t)$, which is called the **coherence Green function**.

And now a subtle point. Notice that although we took the matrix elements $\mathcal{G}_{ij}(t)$ by projecting with the electronic Liouville vectors $|ij\rangle\rangle\langle\langle ij|$, at no point did we project out the nuclear degrees of freedom. $\mathcal{G}_{ij}(t)$ is therefore still a superoperator in the nuclear Liouville space. Let us calculate its action on a nuclear operator A:

$$\begin{aligned}
\mathcal{G}_{ij}(t_1)A &= \langle\langle ij|\mathcal{G}(t_1)A|ij\rangle\rangle \\
&= \theta(t_1)\mathrm{Tr}\left[|j\rangle\langle i|\,U(t_1,0)A\,|i\rangle\langle j|\,U^\dagger(t_1,0)\right] \\
&= \theta(t_1)\mathrm{Tr}\left[|j\rangle\langle i|\,e^{-\frac{i}{\hbar}\left(\sum_m |m\rangle H_m\langle m|\right)t_1}\,|i\rangle\,A\,\langle j|\,e^{\frac{i}{\hbar}\left(\sum_m |m\rangle H_m\langle m|\right)t_1}\right] \\
&= \theta(t_1)e^{-\frac{i}{\hbar}H_i t_1}Ae^{\frac{i}{\hbar}H_j t_1}
\end{aligned} \tag{B.61}$$

The linear response terms may thus be recast as:

$$\begin{aligned}
S^{(1)}(t_1) &= \frac{i}{\hbar}\langle\langle V_{eg}|\mathcal{G}_{eg}(t_1)|V_{eg}\rho_g\rangle\rangle - \frac{i}{\hbar}\langle\langle V_{ge}|\mathcal{G}_{ge}(t_1)|\rho_g V_{ge}\rangle\rangle \\
&= \frac{i}{\hbar}\theta(t_1)\mathrm{Tr}\left[V_{ge}e^{-\frac{i}{\hbar}H_e t_1}V_{eg}\rho_g e^{\frac{i}{\hbar}H_g t_1}\right] - \frac{i}{\hbar}\theta(t_1)\mathrm{Tr}\left[V_{eg}e^{-\frac{i}{\hbar}H_g t_1}\rho_g V_{ge}e^{\frac{i}{\hbar}H_e t_1}\right] \\
&= \frac{i}{\hbar}\theta(t_1)\left(\mathrm{Tr}_\mathrm{B}\left[e^{\frac{i}{\hbar}H_g t_1}V_{ge}e^{-\frac{i}{\hbar}H_e t_1}V_{eg}\rho_g\right] - \mathrm{Tr}_\mathrm{B}\left[V_{ge}e^{\frac{i}{\hbar}H_e t_1}V_{eg}e^{-\frac{i}{\hbar}H_g t_1}\rho_g\right]\right)
\end{aligned} \tag{B.62}$$

Note that because everything inside the trace operations are either constants or operators in nuclear space, the trace over electronic states vanishes which leaves a trace over the bath states. They are, here:

$$\begin{aligned}
J(t_1) &= \langle\langle V_{eg}|\mathcal{U}_{eg}(t_1)|V_{eg}\rho(\text{-}\infty)\rangle\rangle \\
&= \mathrm{Tr}_\mathrm{B}\left[e^{\frac{i}{\hbar}H_g t_1}V_{ge}e^{-\frac{i}{\hbar}H_e t_1}V_{eg}\rho_g\right]
\end{aligned} \tag{B.63}$$

B.3.1 Coherence Green Function

Again, the coherence Green function acts upon a nuclear operator A by:

$$\mathcal{G}_{nm}(t)A = \exp\left(-\frac{i}{\hbar}H_n t\right) A \exp\left(\frac{i}{\hbar}H_m t\right) \tag{B.64}$$

Our goal is to factorize this Green function into one of a reference system and a separate part treated perturbatively. We split the Hamiltonian H_n into:

$$H_n = H_j + \overline{W}_j \tag{B.65}$$

Here we adopt the interaction picture, where $\overline{W}_j$ reads in the interaction picture with the associated propagators:

$$\overline{W}_j(\tau) = e^{\frac{i}{\hbar}H_j\tau}\overline{W}_j e^{-\frac{i}{\hbar}H_j\tau} \tag{B.66}$$

$$U_0(t,t_0) = e^{-\frac{i}{\hbar}H_j(t-t_0)} \tag{B.67}$$

$$U_I(t,t_0) = \exp_+\left[-\frac{i}{\hbar}\overline{W}_j(\tau)d\tau\right] \tag{B.68}$$

$$\begin{aligned} U_n(t,t_0) &= e^{-\frac{i}{\hbar}H_n(t-t_0)} \\ &= U_0(t,t_0)U_I(t,t_0) \\ &= e^{-\frac{i}{\hbar}H_j(t-t_0)}\exp_+\left[-\frac{i}{\hbar}\overline{W}_j(\tau)d\tau\right] \end{aligned} \tag{B.69}$$

We split the H_m Hamiltonian in the same way:

$$H_m = H_j + W'_j \tag{B.70}$$

which gives the propagator:

$$U_m^\dagger(t,t_0) = e^{\frac{i}{\hbar}H_m(t-t_0)} = \exp_-\left[\frac{i}{\hbar}\int_{t_0}^{t} W'_j(\tau)d\tau\right] e^{\frac{i}{\hbar}H_j(t-t_0)}$$

The action of the coherence Green function may now be factorized as:

$$\begin{aligned}\mathcal{G}_{nm}(t)A &= \exp\left(-\frac{i}{\hbar}H_n t\right) A \exp\left(\frac{i}{\hbar}H_m t\right) \\ &= e^{-\frac{i}{\hbar}H_j(t-t_0)} \exp_+\left[-\frac{i}{\hbar}\overline{W}_j(\tau)d\tau\right] A \exp_-\left[\frac{i}{\hbar}\int_{t_0}^{t} W'_j(\tau)d\tau\right] e^{\frac{i}{\hbar}H_j(t-t_0)} \\ &= \mathcal{G}_{jj}(t) \exp_+\left[-\frac{i}{\hbar}\overline{W}_j(\tau)d\tau\right] A \exp_-\left[\frac{i}{\hbar}\int_{t_0}^{t} W'_j(\tau)d\tau\right] \end{aligned} \tag{B.71}$$

Practically, we choose a reference Hamiltonian H_j that is convenient and makes physical sense. We give here two examples:

1. $\underline{H_j = H_m}$:

$$\mathcal{G}_{nm}(t)A = \mathcal{G}_{mm}(t) \exp_+\left[-\frac{i}{\hbar}\int_0^t \overline{W}_m(\tau)d\tau\right] A$$

where $\overline{W}_m = H_n - H_m$.

2. $\underline{H_j = H_n}$:

$$\mathcal{G}_{nm}(t)A = \mathcal{G}_{nn}(t)A \exp_-\left[\frac{i}{\hbar}\int_0^t W'_n(\tau)d\tau\right]$$

where $W'_n = H_m - H_n$.

B.3.2 Factorizing the Two-Level Coherence Green Function

We now return to two electronic levels $|g\rangle$ and $|e\rangle$ coupled to a bath of nuclear vibrations. We choose H_g as the reference Hamiltonian, which gives:

$$\begin{aligned}\mathcal{G}_{eg}(t)A &= \mathcal{G}_{gg}(t) \exp_+\left[-\frac{i}{\hbar}(H_e(\tau) - H_g(\tau))d\tau\right] A \\ &= e^{-i\omega_{eg}t}\mathcal{G}_{gg}(t) \exp_+\left[-\frac{i}{\hbar}(H_e(\tau) - H_g(\tau) - \hbar\omega_{eg})d\tau\right] A \\ &= e^{-i\omega_{eg}t}\mathcal{G}_{gg}(t) \exp_+\left[-\frac{i}{\hbar}U(\tau)d\tau\right] A \end{aligned} \tag{B.72}$$

where we've introduced the important quantity U:

$$U = H_e - H_g - \hbar\omega_{eg} \tag{B.73}$$

$$U(t) = e^{\frac{i}{\hbar}H_g t} U e^{-\frac{i}{\hbar}H_g t} \tag{B.74}$$

which represents the electronic energy gap. $\hbar\omega_{eg}$ may be chosen arbitrarily, but as the notation suggests we usually choose it to be the thermally averaged energy gap so that U represents the fluctuations from average. The linear pathways become:

$$\begin{aligned}
J(t_1) &= \langle\langle V_{eg}|\mathcal{U}_{eg}(t_1)|V_{eg}\rho_g\rangle\rangle \\
&= e^{-i\omega_{eg}t_1}\langle\langle V_{eg}|\mathcal{U}_{gg}(t_1)\exp_+\left[-\frac{i}{\hbar}\int_0^{t_1}U(\tau)d\tau\right]|V_{eg}\rho_g\rangle\rangle \\
&= e^{-i\omega_{eg}t_1}\mathrm{Tr}\left[V_{ge}e^{-\frac{i}{\hbar}H_g t_1}\exp_+\left[-\frac{i}{\hbar}\int_0^{t_1}U(\tau)d\tau\right]V_{eg}\rho_g e^{\frac{i}{\hbar}H_g t_1}\right] \\
&= e^{-i\omega_{eg}t_1}\mathrm{Tr}_{\mathrm{B}}\left[V_{ge}(t_1)\exp_+\left[-\frac{i}{\hbar}\int_0^{t_1}U(\tau)d\tau\right]V_{eg}\rho_g\right]
\end{aligned} \tag{B.75}$$

B.3.3 Cumulant Expansion of the Linear Response

We now explicitly write the factorized linear response pathway:

$$\begin{aligned}
J(t_1) &= e^{-i\omega_{eg}t_1}\mathrm{Tr}_{\mathrm{B}}\left[V_{ge}(t_1)\exp_+\left[-\frac{i}{\hbar}\int_0^{t_1}U(\tau)d\tau\right]V_{eg}\rho_g\right] \\
&= e^{-i\omega_{eg}t_1}\left[1 - \frac{i}{\hbar}\int_0^{t_1}\mathrm{Tr}_{\mathrm{B}}\left[U(\tau)\rho_g\right]d\tau\ldots\right. \\
&\qquad\left. + \left(-\frac{i}{\hbar}\right)^2\int_0^{t_1}\int_0^{t_2}\mathrm{Tr}_{\mathrm{B}}\left[U(\tau_2)U(\tau_1)\rho_g\right]d\tau_1 d\tau_2 + \ldots\right]
\end{aligned} \tag{B.76}$$

We note here that the term linear in $U = H_e - H_g - \hbar\omega_{eg}$ is not only time-independent, but also vanishes upon correct choice of $\hbar\omega_{eg}$. We can see this by calculating:

$$\mathrm{Tr}_{\mathrm{B}}\left[U(\tau)\rho_g\right] = \mathrm{Tr}_{\mathrm{B}}\left[Ue^{-\frac{i}{\hbar}H_g\tau}\rho_g e^{\frac{i}{\hbar}H_g\tau}\right] = \mathrm{Tr}_{\mathrm{B}}\left[U\rho_g\right] = \mathrm{Tr}_{\mathrm{B}}\left[(H_e - H_g)\rho_g\right] - \hbar\omega_{eg}$$

where the ground state propagators $e^{\pm\frac{i}{\hbar}H_g\tau}$ vanish since they commute with $\rho_g = \frac{e^{-\beta H_g}}{\mathrm{Tr}\left[e^{-\beta H_g}\right]}$. It is now clear that the linear term vanishes if we choose:

$$\hbar\omega_{eg} = \mathrm{Tr}_\mathrm{B}\left[(H_e - H_g)\rho_g\right] \tag{B.77}$$

which corresponds to the thermally averaged electronic energy gap, as we mentioned previously. We will make this choice for all calculations hereafter.

Now we apply the cumulant expansion technique to the linear response pathway. Postulating a solution for $J(t_1)$ of the form:

$$J(t_1) = J_0 e^{-F(t_1)} \tag{B.78}$$

We expand both $J(t_1)$ and $F(t_1)$ as power series in powers of $U(t)$, which we call λ here for clarity:

$$J(t_1) = J_0(1 + \lambda J_1(t_1) + \lambda^2 J_2(t_1) + \dots) \tag{B.79}$$

$$F(t_1) = \lambda F_1(t_1) + \lambda^2 F_2(t_1) + \dots \tag{B.80}$$

Plugging this expression for $F(t_1)$ into the Ansatz, we find:

$$\begin{aligned} J(t_1) = J_0 e^{-F(t_1)} &= J_0\left[1 - F(t_1) + \frac{1}{2!}F(t_1)^2 + \dots\right] \\ &= J_0\left[1 - \lambda F_1(t_1) - \lambda^2 F_2(t_1) + \frac{1}{2!}\left(\lambda^2 F_1(t_1)^2 + \dots\right) + \dots\right] \\ &= J_0\left[1 - \lambda F_1(t_1) + \lambda^2\left(-F_2(t_1) + \frac{1}{2!}F_1(t_1)^2\right) + \dots\right] \end{aligned} \tag{B.81}$$

Comparing this expression with the Taylor expansion of $J(t_1)$, we find:

$$F_1(t_1) = -J_1(t_1) \qquad F_2(t_1) = \frac{1}{2}J_1(t_1)^2 - J_2(t_1) \tag{B.82}$$

The explicit expression (B.76) for $J(t_1)$ directly gives $J_2(t_1)$ (since the linear term vanishes as we showed above):

$$J_2(t_1) = e^{-i\omega_{eg}t_1}\frac{1}{\hbar^2}\int_0^{t_1}\int_0^{t_2}\mathrm{Tr_B}\left[U(\tau_2)U(\tau_1)\rho_g\right]d\tau_1 d\tau_2 \tag{B.83}$$

Because $F_2(t_1) = -J_2(t_1)$ (again, because the linear term $J_1(t_1)$ vanishes), the linear pathway truncated at second order via the cumulant expansion is:

$$\begin{aligned} J(t_1) &= e^{-F(t_1)} \\ &= e^{-i\omega_{eg}t_1}\exp\left[-\frac{1}{\hbar^2}\int_0^{t_1}\int_0^{t_2}\mathrm{Tr_B}\left[U(\tau_2)U(\tau_1)\rho_g\right]d\tau_1 d\tau_2\right] \\ &= e^{-i\omega_{eg}t_1 - g(t_1)} \end{aligned} \tag{B.84}$$

where the lineshape function $g(t)$ and the two-point correlation function $C(t)$ are defined:

$$g(t) = \int_0^t\int_0^{\tau_2} C(\tau_1)d\tau_1 d\tau_2 \tag{B.85}$$

$$C(t) = \frac{1}{\hbar^2}\mathrm{Tr_B}\left[U(t)U(0)\rho_g\right] \tag{B.86}$$

We have accomplished something very useful. The linear response is now separated into two parts - a factor $e^{-i\omega_{eg}t_1}$ that oscillates at the thermally averaged energy gap and another factor $e^{-g(t_1)}$ that is simply the correlation between two different times of fluctuations in the energy gap.

B.3.4 Cumulant Expansion of the Third-Order Response

The third-order response function is given by:

$$S^{(3)}(t_1,t_2,t_3) = \left(\frac{i}{\hbar}\right)^3\langle\langle V|\mathcal{G}(t_3)\mathcal{V}\mathcal{G}(t_2)\mathcal{V}\mathcal{G}(t_1)\mathcal{V}|\rho(\text{-}\infty)\rangle\rangle \tag{B.87}$$

Again, projecting into the electronic basis $\{|g\rangle, |e\rangle\}$:

$$
\begin{aligned}
S^{(3)}(t_1,t_2,t_3) = &\sum_{\substack{i,j,m,n,o,p\\q,r,s,t,u,v}} \left(\frac{i}{\hbar}\right)^3 \langle\langle V|ij\rangle\rangle\langle\langle ij|\mathcal{G}(t_3)|mn\rangle\rangle\langle\langle mn|\mathcal{V}|op\rangle\rangle\langle\langle op|\mathcal{G}(t_2)|qr\rangle\rangle \\
&\qquad \langle\langle qr|\mathcal{V}|st\rangle\rangle\langle\langle st|\mathcal{G}(t_1)|uv\rangle\rangle\langle\langle uv|\mathcal{V}|\rho(\text{-}\infty)\rangle\rangle \\
= &\sum_{\substack{o,p,q,r\\s,t,u,v}} \left(\frac{i}{\hbar}\right)^3 [V_{ge}\mathcal{G}_{eg}(t_3)\langle\langle eg|\mathcal{V}|op\rangle\rangle\langle\langle op|\mathcal{G}(t_2)|qr\rangle\rangle \\
&\qquad \langle\langle qr|\mathcal{V}|st\rangle\rangle\langle\langle st|\mathcal{G}(t_1)|uv\rangle\rangle\langle\langle uv|\mathcal{V}|\rho(\text{-}\infty)\rangle\rangle \\
&\quad + V_{eg}\mathcal{G}_{ge}(t_3)\langle\langle ge|\mathcal{V}|op\rangle\rangle\langle\langle op|\mathcal{G}(t_2)|qr\rangle\rangle \\
&\qquad \langle\langle qr|\mathcal{V}|st\rangle\rangle\langle\langle st|\mathcal{G}(t_1)|uv\rangle\rangle\langle\langle uv|\mathcal{V}|\rho(\text{-}\infty)\rangle\rangle] \\
= &\sum_{s,t,u,v} \left(\frac{i}{\hbar}\right)^3 \\
&\quad [V_{ge}\mathcal{G}_{eg}(t_3)V_{eg}\mathcal{G}_{gg}(t_2)\langle\langle gg|\mathcal{V}|st\rangle\rangle\langle\langle st|\mathcal{G}(t_1)|uv\rangle\rangle\langle\langle uv|\mathcal{V}|\rho(\text{-}\infty)\rangle\rangle \\
&\qquad - V_{ge}\mathcal{G}_{eg}(t_3)V_{eg}\mathcal{G}_{ee}(t_2)\langle\langle ee|\mathcal{V}|st\rangle\rangle\langle\langle st|\mathcal{G}(t_1)|uv\rangle\rangle\langle\langle uv|\mathcal{V}|\rho(\text{-}\infty)\rangle\rangle \\
&\qquad + V_{eg}\mathcal{G}_{ge}(t_3)V_{ge}\mathcal{G}_{ee}(t_2)\langle\langle ee|\mathcal{V}|st\rangle\rangle\langle\langle st|\mathcal{G}(t_1)|uv\rangle\rangle\langle\langle uv|\mathcal{V}|\rho(\text{-}\infty)\rangle\rangle \\
&\qquad - V_{eg}\mathcal{G}_{ge}(t_3)V_{ge}\mathcal{G}_{gg}(t_2)\langle\langle gg|\mathcal{V}|st\rangle\rangle\langle\langle st|\mathcal{G}(t_1)|uv\rangle\rangle\langle\langle uv|\mathcal{V}|\rho(\text{-}\infty)\rangle\rangle] \\
= &\left(\frac{i}{\hbar}\right)^3 [V_{ge}\mathcal{G}_{eg}(t_3)V_{eg}\mathcal{G}_{gg}(t_2)V_{ge}\mathcal{G}_{eg}(t_1)\langle\langle eg|\mathcal{V}|\rho(\text{-}\infty)\rangle\rangle \\
&\qquad - V_{ge}\mathcal{G}_{eg}(t_3)V_{eg}\mathcal{G}_{gg}(t_2)V_{eg}\mathcal{G}_{ge}(t_1)\langle\langle ge|\mathcal{V}|\rho(\text{-}\infty)\rangle\rangle \\
&\qquad - V_{ge}\mathcal{G}_{eg}(t_3)V_{eg}\mathcal{G}_{ee}(t_2)V_{eg}\mathcal{G}_{ge}(t_1)\langle\langle ge|\mathcal{V}|\rho(\text{-}\infty)\rangle\rangle \\
&\qquad + V_{ge}\mathcal{G}_{eg}(t_3)V_{eg}\mathcal{G}_{ee}(t_2)V_{ge}\mathcal{G}_{eg}(t_1)\langle\langle eg|\mathcal{V}|\rho(\text{-}\infty)\rangle\rangle \\
&\qquad + V_{eg}\mathcal{G}_{ge}(t_3)V_{ge}\mathcal{G}_{ee}(t_2)V_{eg}\mathcal{G}_{ge}(t_1)\langle\langle ge|\mathcal{V}|\rho(\text{-}\infty)\rangle\rangle \\
&\qquad - V_{eg}\mathcal{G}_{ge}(t_3)V_{ge}\mathcal{G}_{ee}(t_2)V_{ge}\mathcal{G}_{eg}(t_1)\langle\langle eg|\mathcal{V}|\rho(\text{-}\infty)\rangle\rangle \\
&\qquad - V_{eg}\mathcal{G}_{ge}(t_3)V_{ge}\mathcal{G}_{gg}(t_2)V_{ge}\mathcal{G}_{eg}(t_1)\langle\langle eg|\mathcal{V}|\rho(\text{-}\infty)\rangle\rangle \\
&\qquad + V_{eg}\mathcal{G}_{ge}(t_3)V_{ge}\mathcal{G}_{gg}(t_2)V_{eg}\mathcal{G}_{ge}(t_1)\langle\langle ge|\mathcal{V}|\rho(\text{-}\infty)\rangle\rangle]
\end{aligned}
$$

We can rewrite the above terms as inner products:

$$\begin{aligned}
S^{(3)}(t_1,t_2,t_3) = \left(\frac{i}{\hbar}\right)^3 [&\langle\langle V_{eg}|\mathcal{G}_{eg}(t_3)V_{eg}\mathcal{G}_{gg}(t_2)V_{ge}\mathcal{G}_{eg}(t_1)|V_{eg}\rho_g\rangle\rangle \\
&- \langle\langle V_{eg}|\mathcal{G}_{eg}(t_3)V_{eg}\mathcal{G}_{gg}(t_2)V_{eg}\mathcal{G}_{ge}(t_1)|\rho_g V_{ge}\rangle\rangle \\
&- \langle\langle V_{eg}|\mathcal{G}_{eg}(t_3)V_{eg}\mathcal{G}_{ee}(t_2)V_{eg}\mathcal{G}_{ge}(t_1)|\rho_g V_{ge}\rangle\rangle \\
&+ \langle\langle V_{eg}|\mathcal{G}_{eg}(t_3)V_{eg}\mathcal{G}_{ee}(t_2)V_{ge}\mathcal{G}_{eg}(t_1)|V_{eg}\rho_g\rangle\rangle \\
&+ \langle\langle V_{ge}|\mathcal{G}_{ge}(t_3)V_{ge}\mathcal{G}_{ee}(t_2)V_{eg}\mathcal{G}_{ge}(t_1)|\rho_g V_{ge}\rangle\rangle \\
&- \langle\langle V_{ge}|\mathcal{G}_{ge}(t_3)V_{ge}\mathcal{G}_{ee}(t_2)V_{ge}\mathcal{G}_{eg}(t_1)|V_{eg}\rho_g\rangle\rangle \\
&- \langle\langle V_{ge}|\mathcal{G}_{ge}(t_3)V_{ge}\mathcal{G}_{gg}(t_2)V_{ge}\mathcal{G}_{eg}(t_1)|V_{eg}\rho_g\rangle\rangle \\
&+ \langle\langle V_{ge}|\mathcal{G}_{ge}(t_3)V_{ge}\mathcal{G}_{gg}(t_2)V_{eg}\mathcal{G}_{ge}(t_1)|\rho_g V_{ge}\rangle\rangle] \\
= \left(\frac{i}{\hbar}\right)^3 &\sum_{\alpha=1}^{4}[R_\alpha(t_1,t_2,t_3) - R_\alpha^*(t_1,t_2,t_3)]
\end{aligned} \tag{B.88}$$

where the 8 third-order pathways are defined:

$$\begin{aligned}
R_1(t_1,t_2,t_3) &= \langle\langle V_{eg}|\mathcal{G}_{eg}(t_3)V_{eg}\mathcal{G}_{ee}(t_2)V_{ge}\mathcal{G}_{eg}(t_1)|V_{eg}\rho_g\rangle\rangle \\
R_2(t_1,t_2,t_3) &= \langle\langle V_{ge}|\mathcal{G}_{ge}(t_3)V_{ge}\mathcal{G}_{ee}(t_2)V_{eg}\mathcal{G}_{ge}(t_1)|\rho_g V_{ge}\rangle\rangle \\
R_3(t_1,t_2,t_3) &= \langle\langle V_{ge}|\mathcal{G}_{ge}(t_3)V_{ge}\mathcal{G}_{gg}(t_2)V_{eg}\mathcal{G}_{ge}(t_1)|\rho_g V_{ge}\rangle\rangle \\
R_4(t_1,t_2,t_3) &= \langle\langle V_{eg}|\mathcal{G}_{eg}(t_3)V_{eg}\mathcal{G}_{gg}(t_2)V_{ge}\mathcal{G}_{eg}(t_1)|V_{eg}\rho_g\rangle\rangle
\end{aligned} \tag{B.89}$$

All of the algebraic steps above were performed by using:

$$\begin{aligned}
\langle\langle ij|\mathcal{V}|mn\rangle\rangle &= \mathrm{Tr}\left[|j\rangle\langle i|\,V\,|m\rangle\langle n|\right] - \mathrm{Tr}\left[|j\rangle\langle i\,|\,m\rangle\langle n|\,V\right] \\
&= V_{im}\delta_{jn} - V_{nj}\delta_{im}
\end{aligned} \tag{B.90}$$

and that $\langle\langle ij|\mathcal{G}(t)|mn\rangle\rangle$ is nonzero only if $i = m$ and $j = n$.

We can apply the cumulant expansion to the third-order pathways via the same

procedure shown above. Here we state only the final result:

$$\begin{aligned}
R_1(t_1,t_2,t_3) &= e^{-i\omega_{eg}t_1 - i\omega_{eg}t_3} e^{-g^*(t_3)-g(t_1)-g^*(t_2)+g^*(t_2+t_3)+g(t_1+t_2)-g(t_1+t_2+t_3)} \\
R_2(t_1,t_2,t_3) &= e^{i\omega_{eg}t_1 - i\omega_{eg}t_3} e^{-g^*(t_3)-g^*(t_1)+g^*(t_2)-g^*(t_2+t_3)-g(t_1+t_2)+g(t_1+t_2+t_3)} \\
R_3(t_1,t_2,t_3) &= e^{i\omega_{eg}t_1 - i\omega_{eg}t_3} e^{-g(t_3)-g^*(t_1)+g(t_2)-g(t_2+t_3)-g(t_1+t_2)+g(t_1+t_2+t_3)} \\
R_4(t_1,t_2,t_3) &= e^{-i\omega_{eg}t_1 - i\omega_{eg}t_3} e^{-g(t_3)-g(t_1)-g(t_2)+g(t_2+t_3)+g(t_1+t_2)-g(t_1+t_2+t_3)}
\end{aligned} \tag{B.91}$$

where as defined above, the lineshape function $g(t)$ and the two-point correlation function $C(t)$ are given by:

$$g(t) = \int_0^t \int_0^{\tau_2} C(\tau_1) d\tau_1 d\tau_2 \qquad C(t) = \frac{1}{\hbar^2} \mathrm{Tr_B}\left[U(t)U(0)\rho_g\right]$$

B.3.5 The Spectral Density

In general, the correlation function $C(t)$ is complex:

$$\begin{aligned}
C(t) &= \mathrm{Re}\left[C(t)\right] + i\mathrm{Im}\left[C(t)\right] \\
&= C'(t) + iC''(t)
\end{aligned} \tag{B.92}$$

where the real and imaginary parts can easily be shown to be:

$$C'(t) = \frac{1}{2\hbar^2}\left(\mathrm{Tr_B}\left[U(t)U(0)\rho_g\right] + \mathrm{Tr_B}\left[U(0)U(t)\rho_g\right]\right) \tag{B.93}$$

$$C''(t) = -\frac{i}{2\hbar^2}\left(\mathrm{Tr_B}\left[U(t)U(0)\rho_g\right] - \mathrm{Tr_B}\left[U(0)U(t)\rho_g\right]\right) \tag{B.94}$$

Often it is more convenient to work in the frequency domain. To this end, the frequency domain correlation function is given by the Fourier transform of $C(t)$:

$$C(\omega) = \int_{-\infty}^{\infty} C(t) e^{i\omega t} dt \tag{B.95}$$

Separating the real and imaginary parts of $C(t)$:

$$\begin{aligned} C(\omega) &= \int_{-\infty}^{\infty} [C'(t) + iC''(t)] e^{i\omega t} dt \\ &= C'(\omega) + C''(\omega) \end{aligned} \tag{B.96}$$

where we've defined:

$$C'(\omega) = \int_{-\infty}^{\infty} C'(t) e^{i\omega t} dt \tag{B.97}$$

$$C''(\omega) = i \int_{-\infty}^{\infty} C''(t) e^{i\omega t} dt \tag{B.98}$$

B.3.5.1 Detailed Balance

We now project the correlation function via the eigenstates of H_g:

$$\begin{aligned} C(t) &= \frac{1}{\hbar^2} \mathrm{Tr_B} \left[U(t) U(0) \rho_g \right] \\ &= \frac{1}{\hbar^2} \sum_{i,j,k} \mathrm{Tr_B} \left[|i\rangle \langle i| \, U(t) \, |j\rangle \langle j| \, U(0) \, |k\rangle \langle k| \, \rho_g \right] \\ &= \frac{1}{\hbar^2} \sum_{i,j,k} \langle i \,|\, U(t) \,|\, j \rangle \langle j \,|\, U(0) \,|\, k \rangle \langle k \,|\, \rho_g \,|\, i \rangle \\ &= \frac{1}{\hbar^2} \sum_{i,j,k} \langle i \,|\, U(t) \,|\, j \rangle \langle j \,|\, U(0) \,|\, k \rangle \, \delta_{ki} \frac{e^{-\beta E_k}}{\sum\limits_{\ell} e^{-\beta E_\ell}} \\ &= \frac{1}{\hbar^2} \sum_{i,j} \langle i \,|\, U(t) \,|\, j \rangle \langle j \,|\, U(0) \,|\, i \rangle \, \frac{e^{-\beta E_i}}{\sum\limits_{\ell} e^{-\beta E_\ell}} \\ &= \frac{1}{\hbar^2} \sum_{i,j} e^{-\frac{i}{\hbar}(E_j - E_i)t} \langle i \,|\, U \,|\, j \rangle \langle j \,|\, U \,|\, i \rangle \, P(i) \\ &= \frac{1}{\hbar^2} \sum_{i,j} e^{-i\omega_{ji} t} |U_{ij}|^2 P(i) \end{aligned} \tag{B.99}$$

Its real and imaginary parts are then:

$$C'(t) = \frac{1}{2}\left[C(t) + C^*(t)\right] = \sum_{i,j} \frac{P(j) + P(i)}{2\hbar^2} |U_{ij}|^2 \cos(\omega_{ji} t) \tag{B.100}$$

$$C''(t) = -\frac{i}{2}\left[C(t) - C^*(t)\right] = \sum_{i,j} \frac{P(j) - P(i)}{2\hbar^2} |U_{ij}|^2 \sin(\omega_{ji} t) \tag{B.101}$$

which gives the even and odd symmetry frequency domain components:

$$C'(\omega) = \int_{-\infty}^{\infty} C'(t) e^{i\omega t} dt = \pi \sum_{i,j} \frac{P(j) + P(i)}{2\hbar^2} |U_{ij}|^2 \left[\delta(\omega - \omega_{ji}) + \delta(\omega + \omega_{ji})\right] \tag{B.102}$$

$$C''(\omega) = \int_{-\infty}^{\infty} C''(t) e^{i\omega t} dt = \pi \sum_{i,j} \frac{P(i) - P(j)}{2\hbar^2} |U_{ij}|^2 \left[\delta(\omega - \omega_{ji}) - \delta(\omega + \omega_{ji})\right] \tag{B.103}$$

Integrating $C'(\omega)$ in frequency:

$$\begin{aligned}
\int_0^{\infty} C'(\omega) d\omega &= \pi \sum_{i,j} \frac{P(j) + P(i)}{2\hbar^2} |U_{ij}|^2 \\
&= \pi \sum_{i,j} \frac{P(j) + P(i)}{P(i) - P(j)} \frac{P(i) - P(j)}{2\hbar^2} |U_{ij}|^2 \\
&= \pi \sum_{i,j} \frac{e^{-\beta\hbar\omega_j} + e^{-\beta\hbar\omega_i}}{e^{-\beta\hbar\omega_i} - e^{-\beta\hbar\omega_j}} \frac{P(i) - P(j)}{2\hbar^2} |U_{ij}|^2 \\
&= \pi \sum_{i,j} \frac{e^{\beta\hbar\omega_{ji}} + 1}{e^{\beta\hbar\omega_{ji}} - 1} \frac{P(i) - P(j)}{2\hbar^2} |U_{ij}|^2 \\
&= \pi \sum_{i,j} \coth(\beta\hbar\omega_{ji}/2) \frac{P(i) - P(j)}{2\hbar^2} |U_{ij}|^2 \\
&= \int_0^{\infty} \coth(\beta\hbar\omega/2) C''(\omega) d\omega
\end{aligned}$$

and by a similar procedure:

$$\int_{-\infty}^{0} C'(\omega)d\omega = \int_{-\infty}^{0} \coth(\beta\hbar\omega/2)C''(\omega)d\omega$$

Comparing the kernels of each integral, we thus derive the detailed balance relation between $C'(\omega)$ and $C''(\omega)$:

$$C'(\omega) = \coth(\beta\hbar\omega/2)C''(\omega) \tag{B.104}$$

Now is a good time to finally name $C''(\omega)$ as the **spectral density**. It can be shown that for a harmonic bath, the spectral density is independent of temperature. For this reason, the spectral density is the simplest quantity to characterize system-bath coupling, so we can use the detailed balance relation to write:

$$C(\omega) = C'(\omega) + C''(\omega) = \left[\coth(\beta\hbar\omega/2) + 1\right] C''(\omega) \tag{B.105}$$

B.3.5.2 Recasting the Lineshape Function

We now recast the lineshape function as a frequency domain integral:

$$\begin{aligned}
g(t) &= \int_0^t \int_0^{\tau_2} C(\tau_1)d\tau_1 d\tau_2 \\
&= \frac{1}{2\pi}\int_{-\infty}^{\infty} C(\omega) \int_0^t \int_0^{\tau_2} e^{-i\omega\tau_1} d\tau_1 d\tau_2 d\omega \\
&= \frac{1}{2\pi}\int_{-\infty}^{\infty} C(\omega) \int_0^t \frac{i}{\omega}\left(e^{-i\omega\tau_2} - 1\right) d\tau_2 d\omega \\
&= \frac{1}{2\pi}\int_{-\infty}^{\infty} C(\omega)\frac{i}{\omega}\left[\frac{i}{\omega}e^{-i\omega\tau_2} - \tau_2\Big|_0^t\right] d\omega \\
&= \frac{1}{2\pi}\int_{-\infty}^{\infty} \frac{C(\omega)}{\omega^2}\left(1 - e^{-i\omega t} - i\omega t\right) d\omega \\
&= \frac{1}{2\pi}\int_{-\infty}^{\infty} \frac{C(\omega)}{\omega^2}\left[(1 - \cos(\omega t)) + i\left(\sin(\omega t) - \omega t\right)\right] d\omega
\end{aligned} \tag{B.106}$$

and via the detailed balance relation, we find:

$$\begin{aligned} g(t) &= \frac{1}{2\pi}\int_{-\infty}^{\infty} C''(\omega)\frac{\coth(\beta\hbar\omega/2)+1}{\omega^2}\left[(1-\cos(\omega t))+i\left(\sin(\omega t)-\omega t\right)\right]d\omega \\ &= \frac{1}{2\pi}\int_{-\infty}^{\infty}\frac{1-\cos(\omega t)}{\omega^2}\coth(\beta\hbar\omega/2)C''(\omega)d\omega + \frac{i}{2\pi}\int_{-\infty}^{\infty}\frac{\sin(\omega t)-\omega t}{\omega^2}C''(\omega)d\omega \end{aligned} \tag{B.107}$$

where some terms vanish by inspection due to even/odd symmetry.

We have now derived a representation of the dephasing lineshape function $g(t)$ in terms of the spectral density $C''(\omega)$, which has the benefit of separating temperature dependence in a single $\coth(\beta\hbar\omega/2)$ factor. Strictly speaking, the spectral density characterizes the system-bath coupling and not the bath degrees of freedom alone. For an identical system different transitions may have different corresponding spectral densities due to different frequency-dependent coupling strengths. In the literature, spectral densities have been derived for different model systems, but these calculations are out of the scope of our discussion.

B.3.5.3 The Spectral Density and the Spectral Density

A point of caution: some references define the spectral density as $J(\omega)$:

$$J(\omega) = \frac{\pi D(\omega)c^2(\omega)}{2\omega} \tag{B.108}$$

where $D(\omega)$ is the density of states of the harmonic reservoir and $c^2(\omega)$ represents the system-reservoir coupling strength. Others define it as $C''(\omega)$, which is the anti-symmetric component of $\mathcal{F}\{C(t)\}$. The two are related by:

$$C''(\omega) = \omega^2 J(\omega) \tag{B.109}$$

Care must be taken to distinguish between $C''(\omega)$ (which has units of frequency) and $J(\omega)$ (which has units of inverse frequency). The spectral density used in this thesis, that of a spherical quantum dot, is derived as $J(\omega)$.

References

(1) Mukamel, S., *Principles of Nonlinear Optical Spectroscopy*, 1st ed.; Oxford University Press: 1999.

APPENDIX C

Sideband Lineshapes in Multi-Dimensional Spectra

In this Appendix we show straightforward extensions of the procedure outlined by Siemens et al. [1] to fit lineshapes of sidebands in one-quantum and zero-quantum spectra.

C.1 One-Quantum Spectra

Time-Domain Signal

We consider the case of a rephasing signal resulting from excitation and emission frequencies ω_1 and ω_2 respectively (ignoring dynamics during T), and assume perfectly correlated inhomogeneous broadening between the two transitions with dephasing rates γ_1 and γ_2:

$$\begin{aligned} s(t,\tau) &= \Theta(t)\Theta(\tau)e^{-\gamma_1\tau}e^{-\gamma_2 t}\int e^{-i[(\omega_1+\Delta\omega)\tau-(\omega_2+\Delta\omega)t]}e^{-\frac{\Delta\omega^2}{2\sigma^2}}d\Delta\omega \\ &= \Theta(t)\Theta(\tau)e^{-\gamma_1\tau}e^{-\gamma_2 t}e^{-i\omega_1\tau}e^{+i\omega_2 t}\ \mathcal{F}\left\{e^{-\frac{\Delta\omega^2}{2\sigma^2}}\right\}\Bigg|_{t-\tau} \\ &\propto \Theta(t)\Theta(\tau)e^{-\gamma_1\tau}e^{-\gamma_2 t}e^{-i\omega_1\tau}e^{+i\omega_2 t}e^{-\frac{\sigma^2}{2}(t-\tau)^2} \end{aligned} \tag{C.1}$$

Defining the new time variables:

$$t' = \frac{1}{2}(t+\tau) \qquad \tau' = \frac{1}{2}(t-\tau) \tag{C.2}$$

We recast the time-domain signal:

$$s(t',\tau') = \Theta(t'+\tau')\Theta(t'-\tau')e^{-\gamma_1(t'-\tau')}e^{-\gamma_2(t'+\tau')}e^{-i\omega_1(t'-\tau')}e^{+i\omega_2(t'+\tau')}e^{-2\sigma^2\tau'^2} \tag{C.3}$$

New Transform Axes

It is important to determine the specific axes that the new time-variables result in after Fourier transform. Writing out the original transform:

$$f(t,\tau) = \iint e^{-i(\omega_t t+\omega_\tau \tau)} f(\omega_t,\omega_\tau)d\omega_\tau d\omega_t \tag{C.4}$$

In terms of the new time variables:

$$\begin{aligned} f(t',\tau') &= \iint e^{-i[\omega_t(t'+\tau')+\omega_\tau(t'-\tau')]} f(\omega_t,\omega_\tau)d\omega_\tau d\omega_t \\ &= \iint e^{-i[(\omega_t+\omega_\tau)t'+(\omega_t-\omega_\tau)\tau']} f(\omega_t,\omega_\tau)d\omega_\tau d\omega_t \end{aligned}$$

We see that the natural conjugate variables for t' and τ' are:

$$\omega_{t'} = \omega_t + \omega_\tau \qquad \omega_{\tau'} = \omega_t - \omega_\tau \tag{C.5}$$

or equivalently:

$$\omega_t = \omega_{t'} + \omega_{\tau'} \qquad \omega_\tau = \omega_{t'} - \omega_{\tau'} \tag{C.6}$$

NOTE: In the rephasing pulse sequence, ω_τ is negative.

Using the Jacobian of our variable transformation:

$$J = \begin{vmatrix} \frac{d\omega_t}{d\omega_{t'}} & \frac{d\omega_t}{d\omega_{\tau'}} \\ \frac{d\omega_\tau}{d\omega_{t'}} & \frac{d\omega_\tau}{d\omega_{\tau'}} \end{vmatrix} = -1 - 1 = -2 \tag{C.7}$$

We change the variables of integration:

$$f(t', \tau') = 2 \iint e^{-i(\omega_{t'} t' + \omega_{\tau'} \tau')} f(\omega_{t'}, \omega_{\tau'}) d\omega_{\tau'} d\omega_{t'} \tag{C.8}$$

Shift and Projection

We now shift the signal to the origin in our τ' and t' coordinates via multiplication by $e^{+i\omega_1(t'-\tau')\tau'} e^{-i\omega_2(t'+\tau')}$:

$$s_{origin}(t', \tau') = \Theta(t' + \tau')\Theta(t' - \tau') e^{-\gamma_1(t'-\tau')} e^{-\gamma_2(t'+\tau')} e^{-2\sigma^2\tau'^2} \tag{C.9}$$

The projections along t' and τ' are then:

$$s_{proj,t'} = \int_{-\infty}^{\infty} s_{origin}(t', \tau') d\tau' = e^{-(\gamma_1+\gamma_2)t'} \int_{-t'}^{t'} e^{(\gamma_1-\gamma_2)\tau'} e^{-2\sigma^2\tau'^2} d\tau' \tag{C.10}$$

$$s_{proj,\tau'} = \int_{-\infty}^{\infty} s_{origin}(t', \tau') dt' = e^{(\gamma_1-\gamma_2)\tau'} e^{-2\sigma^2\tau'^2} \int_{|\tau'|}^{\infty} e^{-(\gamma_1+\gamma_2)t'} dt' \tag{C.11}$$

where the Heaviside functions are accounted for by change of integration limits.

Inhomogeneous Limit

In the inhomogeneous limit ($\sigma \gg \gamma_1, \gamma_2$) the signal decays along τ' much faster than along t'. In the integral along τ' we can approximate the Gaussian portion of the kernel as a delta function. In the integral along t', we can approximate the lower

limit as 0. These two limits give:

$$s_{proj,t'} = e^{-(\gamma_1+\gamma_2)t'} \int_{-t'}^{t'} e^{(\gamma_1-\gamma_2)\tau'} \delta(\tau') d\tau' = e^{-(\gamma_1+\gamma_2)t'} \Theta(t') \tag{C.12}$$

$$s_{proj,\tau'} = e^{(\gamma_1-\gamma_2)\tau'} e^{-2\sigma^2\tau'^2} \int_0^{\infty} e^{-(\gamma_1-\gamma_2)t'} dt' = e^{(\gamma_1-\gamma_2)\tau'} e^{-2\sigma^2\tau'^2} \tag{C.13}$$

which then give the frequency domain lineshapes in the inhomogeneous limit:

$$S_{slice}(\omega_{t'}) \propto \frac{1}{(\gamma_1+\gamma_2) + i\omega_{t'}} \qquad \text{(Cross-Diagonal)} \tag{C.14}$$

$$S_{slice}(\omega_{\tau'}) \propto e^{-\frac{\omega_{\tau'}^2}{8\sigma^2}} \qquad \text{(Diagonal)} \tag{C.15}$$

where we've assumed $\gamma_1 - \gamma_2 \ll \sigma$.

C.2 Zero-Quantum Lineshapes

The lineshapes of zero-quantum spectra can be derived by the same method, with inclusion of an intermediate zero-quantum coherence with a dephasing rate of γ_T:

$$\begin{aligned}
s(t,T,\tau) &= \Theta(t)\Theta(T)\Theta(\tau) e^{-\gamma_1\tau} e^{-\gamma_2 t} e^{-\gamma_T T} \int e^{-i[(\omega_1+\Delta\omega)\tau - (\omega_2+\Delta\omega)t]} e^{i(\omega_2-\omega_1)T} e^{-\frac{\Delta\omega^2}{2\sigma^2}} d\Delta\omega \\
&= \Theta(t)\Theta(T)\Theta(\tau) e^{-\gamma_1\tau} e^{-\gamma_2 t} e^{-\gamma_T T} e^{i(\omega_2-\omega_1)T} e^{-i\omega_1\tau} e^{+i\omega_2 t} \int e^{i\Delta\omega(t-\tau)} e^{-\frac{\Delta\omega^2}{2\sigma^2}} d\Delta\omega \\
&= \Theta(t)\Theta(T)\Theta(\tau) e^{-\gamma_1\tau} e^{-\gamma_2 t} e^{-\gamma_T T} e^{i(\omega_2-\omega_1)T} e^{-i\omega_1\tau} e^{i\omega_2 t} \mathcal{F}\left\{ e^{-\frac{\Delta\omega^2}{2\sigma^2}} \right\}\Big|_{t-\tau} \\
&= \Theta(t)\Theta(T)\Theta(\tau) e^{-\gamma_1\tau} e^{-\gamma_2 t} e^{-\gamma_T T} e^{i(\omega_2-\omega_1)T} e^{-i\omega_1\tau} e^{i\omega_2 t} \left[e^{-\frac{\sigma^2}{2}t'^2} \right]_{t'=t-\tau} \\
&= \Theta(t)\Theta(T)\Theta(\tau) e^{-\gamma_1\tau} e^{-\gamma_2 t} e^{-\gamma_T T} e^{i(\omega_2-\omega_1)T} e^{-i\omega_1\tau} e^{i\omega_2 t} e^{-\frac{\sigma^2}{2}(t-\tau)^2}
\end{aligned} \tag{C.16}$$

Shift frequency domain peak to origin:

$$\begin{aligned} s_{origin}(t,T,\tau) &= s(t,T,\tau)e^{-i(\omega_2-\omega_1)T}e^{-i\omega_2 t} \\ &= \Theta(t)\Theta(T)\Theta(\tau)e^{-\gamma_1\tau}e^{-\gamma_2 t}e^{-\gamma_T T}e^{-i\omega_1\tau}e^{-\frac{\sigma^2}{2}(t-\tau)^2} \end{aligned} \tag{C.17}$$

Project onto T axis:

$$\begin{aligned} s_{proj}(T) &= \int_{-\infty}^{\infty} s_{origin}(t,T,\tau)dt \\ &= \Theta(t)\Theta(T)\Theta(\tau)e^{-\gamma_1\tau}e^{-\gamma_T T}e^{-i\omega_1\tau}\int_0^{\infty} e^{-\gamma_2 t}e^{-\frac{\sigma^2}{2}(t-\tau)^2}dt \\ &= \Theta(t)\Theta(T)\Theta(\tau)e^{-(\gamma_1+\gamma_2)\tau}e^{-\gamma_T T}e^{-i\omega_1\tau}\int_{-\tau}^{\infty} e^{-\gamma_2 t'}e^{-\frac{\sigma^2}{2}t'^2}dt' \end{aligned} \tag{C.18}$$

In the inhomogeneous limit:

$$s_{proj}(T) = \Theta(t)\Theta(T)\Theta(\tau)e^{-(\gamma_1+\gamma_2)\tau}e^{-\gamma_T T}e^{-i\omega_1\tau} \tag{C.19}$$

which gives the lineshape:

$$\begin{aligned} S_{slice}(\omega_T) &= \Theta(t)\Theta(\tau)e^{-(\gamma_1+\gamma_2)\tau}e^{-i\omega_1\tau}\mathcal{F}\left\{e^{-\gamma_T T}\Theta(T)\right\} \\ &\propto \Theta(t)\Theta(\tau)e^{-(\gamma_1+\gamma_2)\tau}e^{-i\omega_1\tau}\frac{1}{\gamma_T - i\omega_T} \end{aligned} \tag{C.20}$$

References

(1) Siemens, M. E.; Moody, G.; Li, H.; Bristow, A. D.; Cundiff, S. T. *Optics Express* **2010**, *18*, 17699–17708.

APPENDIX D

Absorption Characteristics of Perovskite Nanocrystals

Reproduced in part with permission from:

A. Liu, L. G. Bonato, F. Sessa, D. B. Almeida, E. Isele, G. Nagamine, L. F. Zagonel, A. F. Nogueira, L. A. Padilha, and S. T. Cundiff. "Communication: Effect of Dimensionality on the Optical Absorption Properties of $CsPbI_3$ Perovskite Nanocrystals". *J. Chem. Phys.* **151**, 19 (2019).

In this Appendix, we present the absorption characteristics of $CsPbI_3$ perovskite nanocrystals discussed in Chapters VI and VII.

D.1 $CsPbI_3$ Nanocube Absorption

$CsPbI_3$ nanocube absorption spectra normalized to the lowest-energy 1S exciton absorption peak at temperatures ranging from 4 K to 140 K are plotted in Fig. D.1.

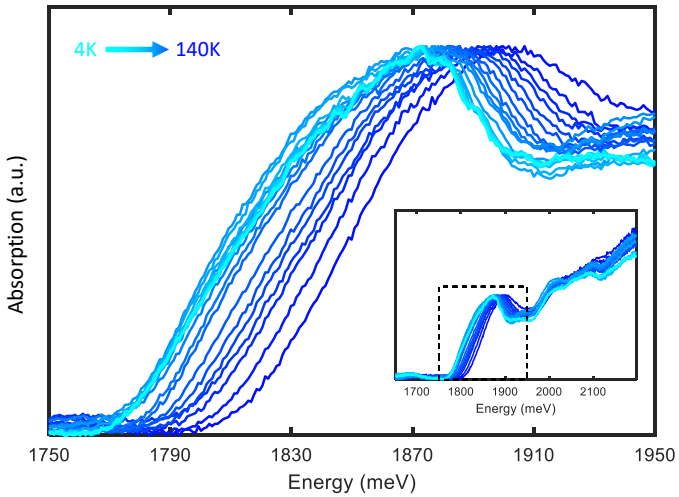

Figure D.1: Absorption spectra of $CsPbI_3$ nanocrystals at temperatures ranging from 4 K to 140 K as indicated. The full-range spectra are plotted inset, while the 1S exciton peak outlined by the dashed box is shown in the main plot. The specific temperatures plotted are indicated by the data in Fig. D.2(b).

Although multiple peaks are observed that correspond to distinct exciton transitions, here we focus on the 1S exciton absorption peak that reflects the fundamental electronic band-gap (energy-gap) of the nanocrystals. As temperature increases the band-gap exhibits a pronounced blue-shift to higher energies, which is contrary to the red-shift observed in most solids. In the literature, this phenomenon has been referred to as an anomalous band-gap shift [1–4].

To quantify the band-gap shift, we fit the peaks with Gaussian lineshapes that reflect the size distribution of the nanocrystals. As shown in Fig. D.2(a), we fit only the top of each peak due to absorption tails present at lower temperatures. The widths σ of each Gaussian fit, allowed to vary freely, do not change significantly with temperature (mean width 41.81 meV and standard deviation 3.37 meV). The fitted Gaussian center energies (which agree closely with center energies found from a fourth-order polynomial fit) are plotted in Fig. D.2(b), which reveals interesting behavior at temperatures below 50 K. Specifically, two clear inflection points at 20 and 30 K are observed that reveal more complicated band-gap behavior than previously reported for photoluminescence measurements of similar perovskite nanocubes [4].

D.1.1 Vibrational Band-Gap Renormalization

The dependence of the electronic band-gap on temperature T may be expressed as [3, 5]:

$$E_g(T) = E_0 + AT + \sum_n B_n \left(\frac{1}{e^{\hbar\omega_n / k_B T} - 1} + \frac{1}{2} \right). \tag{D.1}$$

The first term E_0 is the intrinsic material band-gap at $T = 0$, and the coefficient A in the second term characterizes the change in band-gap due to lattice unit cell expansion/contraction (in the so-called quasi-harmonic approximation [5]). Here the change in quantum confinement energy due to expansion/contraction of nanocrystal volume, which we expect to be negligible at low temperatures [6], is ignored. The third term then represents renormalization of the band-gap due to electron-phonon interactions, where n is summed over all phonon branches and all wave-vectors within the Brillouin zone for each branch. B_n and $\hbar\omega_n$ are the electron-phonon coupling strength and vibrational energy respectively for mode n. Whether B_n is positive or negative, resulting in an increase or decrease of the band-gap respectively, arises from a complex interplay of microscopic dynamics and cannot be predicted easily from the properties of a given phonon branch [1, 7]. However, accounting for all possible phonon branches throughout the Brillouin zone is often unnecessary in modeling the behavior of real systems. Instead, one [8] or two [1] vibrational modes are usually assumed dominant (referred to as one-oscillator and two-oscillator models) which reduces the summation to either one or two terms respectively.

Here, we find both the one-oscillator and two-oscillator models to be insufficient in modeling the band-gap temperature dependence observed for $CsPbI_3$ nanocubes. As mentioned above, two inflection points are observed that necessitate at least three dominant vibrational modes that independently renormalize the band-gap. A least-squares fit of the band-gap temperature dependence to this three-oscillator model

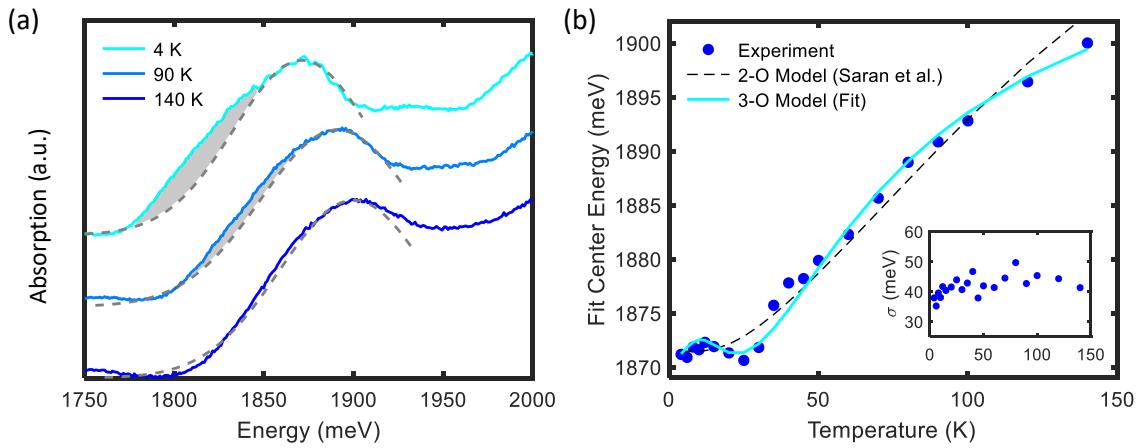

Figure D.2: (a) Gaussian peak fits of $CsPbI_3$ absorption spectra at three representative temperatures 4, 90, and 140 K. A low-energy absorption tail, indicated by the shaded gray region, forms at low temperature. (b) Dark-blue dots show fitted Gaussian center energy as a function of temperature, which reflects the material band-gap. A two-oscillator (2-O) model using the fitted parameters from Saran et al. [4] and a fit to the three-oscillator (3-O) model described in the text are then plotted as the dashed black curve and solid light-blue curve respectively. The fitted Gaussian widths σ are plotted inset.

is plotted in Fig. D.2(b), where good agreement is observed at both high and low temperatures. The fitted parameters are $E_0 = 1916.9$ meV, $A = 0.3$ meV/K, $\hbar\omega_1 = 5.38$ meV, $\hbar\omega_2 = 5.91$ meV, $\hbar\omega_3 = 17.02$ meV, $B_1 = -698.01$ meV, $B_2 = 821.67$ meV, and $B_3 = -217.39$ meV. Instead of the acoustic and optical phonon categories that are usually invoked for two-oscillator models [3, 4], a three-oscillator model in perovskite materials align more naturally to the bending, stretching, and rocking perovskite vibrational modes that possess distinct ranges of vibrational energies [9].

We note that although the two-oscillator model was recently invoked by Saran et al. to model the temperature dependence of photoluminescence center energy in perovskite nanocrystals [4], the data points taken at low temperatures (below 50 K) were too sparse to resolve the two inflection points we observe. Their resultant fitted band-gap dependence is plotted in Fig. D.2b for comparison. In contrast to features in absorption spectra, which are simply proportional to the oscillator strength of each optical transition, features in photoluminescence spectra depend on many

other temperature-dependent factors such as the equilibrium fine-structure carrier distribution [10, 11] and emission Stokes shifts [12]. It is therefore unclear whether the apparent two-oscillator behavior of their measurements on $CsPbI_3$ nanocubes was due to coarse-graining effects or the above confounding factors in temperature-dependent photoluminescence.

D.1.2 Band-Tailing in Absorption Spectra

Lower-energy absorption tails are observed. For ideal nanocubes, the exciton density of states are comprised of delta functions that result in roughly Gaussian absorption peaks (reflecting the nanocrystal size distribution). Absorption tails at lower-energy are therefore indicative of corresponding tails of the electronic density of states, often attributed to impurities [13] or surface states [14]. As shown in Fig. D.2(a), the absorption peak is Gaussian at 140 K and develops a lower-energy tail with decreasing temperature. We attribute this tail to shallow defect states surrounding the valence band-edge that have been shown to arise from lattice point defects [15]. At high temperatures valence band electrons populate the band-edge in a thermal equilibrium distribution. At low temperatures those electrons then fill the defect states from lowest energy upwards, which comprise a Halperin-Lax type distribution [16] with a $\exp(\sqrt{E})$ dependence [17, 18]. The disappearance of the tail at 140 K thus suggests a few-meV (comparable to the 140 K Boltzmann energy of 12 meV) defect state energy distribution. Although in principle such defect state absorption should manifest in photoluminescence spectra as well, no clear band-tailing was observed in low-temperature photoluminescence measurements [4]. This is unsurprising, since above-gap excitation results in competing band-edge and defect state relaxation pathways and emission Stokes shifts (on the order of tens of meV in perovskite nanocrystals [4, 19]) likely differ for defect transitions. For additional comparison, absorption measurements were also performed on $CsPbBr_3$ nanocubes

[20]. Although a large anomalous band-gap shift was observed (approximately 40 meV from 6 to 140 K), no absorption tail forms at low temperatures.

D.2 $CsPbI_3$ Nanoplatelet Absorption

Electron-phonon coupling that renormalizes the $CsPbI_3$ bandgap should depend strongly on dimensionality in nanocrystals. In particular, lowering dimensionality should reduce electron-phonon coupling by restricting certain vibrational modes. To investigate the effect of lattice dimensionality on electron-phonon coupling, we repeat the same temperature-dependent absorption measurements on $CsPbI_3$ nanoplatelets. At room-temperature, a single nanoplatelet absorption peak is observed that is blue-shifted relative to the nanocube band-gap due to strong quantum confinement in the out-of-plane direction. At cryogenic temperatures, shown in Fig. D.3, the absorption spectrum changes in two surprising ways. First, the nanoplatelet absorption peak continues narrowing below 140 K (with no absorption tail), in contrast to the nanocube absorption peak width that remains constant at low temperatures. Second, an additional lower-energy peak also appears with decreasing temperature (see Fig. D.3a) which, due to its center energy, we attribute to co-synthesized $CsPbI_3$ nanocubes.

Again fitting the nanoplatelet absorption peaks to Gaussian lineshapes, the fitted center energies are plotted in Fig. D.3b. The nearly-linear anomalous band-gap shift indicates weakened electron-phonon interactions and greater importance of band-gap renormalization due to unit cell expansion/contraction with temperature. To quantify these changes, we perform a linear fit of the center energy temperature-dependence. The fitted parameters are $E_0 = 2055.4$ meV and $A = 0.2$ meV/K, where A is comparable to its corresponding nanocube value. Therefore, decreasing dimensionality greatly reduces vibrational band-gap renormalization without strongly affecting that due to changes in unit cell size.

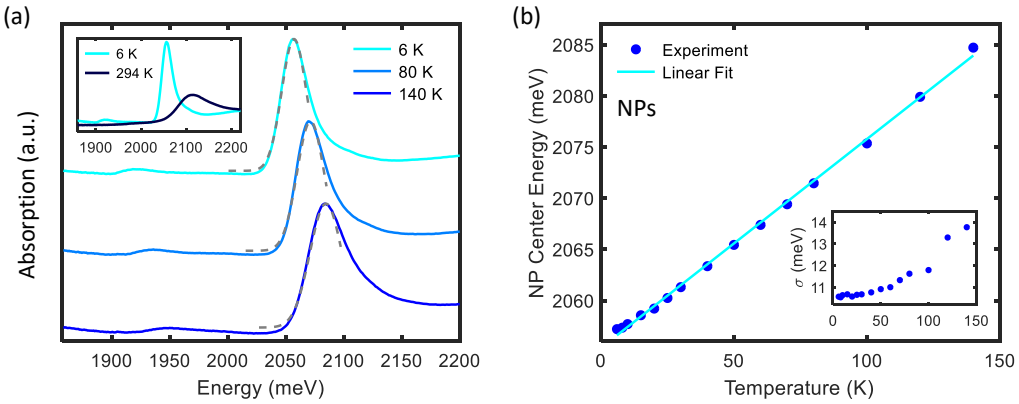

Figure D.3: (a) Absorption spectra of $CsPbI_3$ nanoplatelets at three representative temperatures 6, 80, and 140 K. In addition to the main nanoplatelet absorption peak, a weak nanocube absorption peak at lower energy appears at low temperatures. Inset shows comparison between 6 K and room-temperature absorption spectra. (b) Nanoplatelet center energies obtained from the absorption peak fits as a function of temperature, which reflects the material band-gap. A linear fit is plotted as the solid blue curve. The fitted Gaussian widths are plotted inset, which monotonically decrease with decreasing temperature.

References

(1) Göbel, A.; Ruf, T.; Cardona, M.; Lin, C. T.; Wrzesinski, J.; Steube, M.; Reimann, K.; Merle, J.-C.; Joucla, M. *Physical Review B* **1998**, *57*, 15183–15190.

(2) Choi, I.-H.; Yu, P. Y. *Physical Review B* **2001**, *63*, 235210.

(3) Yu, C.; Chen, Z.; J. Wang, J.; Pfenninger, W.; Vockic, N.; Kenney, J. T.; Shum, K. *Journal of Applied Physics* **2011**, *110*, 063526.

(4) Saran, R.; Heuer-Jungemann, A.; Kanaras, A. G.; Curry, R. J. *Advanced Optical Materials* **2017**, *5*, 1700231.

(5) Cardona, M. *Solid State Communications* **2005**, *133*, 3–18.

(6) Moses Badlyan, N.; Biermann, A.; Aubert, T.; Hens, Z.; Maultzsch, J. *Physical Review B* **2019**, *99*, 195425.

(7) Garro, N.; Cantarero, A.; Cardona, M.; Göbel, A.; Ruf, T.; Eberl, K. *Physical Review B* **1996**, *54*, 4732–4740.

(8) Choi, I.-H.; Eom, S.-H.; Yu, P. Y. *physica status solidi (b)* **1999**, *215*, 99–104.

(9) Pérez-Osorio, M. A.; Milot, R. L.; Filip, M. R.; Patel, J. B.; Herz, L. M.; Johnston, M. B.; Giustino, F. *The Journal of Physical Chemistry C* **2015**, *119*, 25703–25718.

(10) Yin, C.; Chen, L.; Song, N.; Lv, Y.; Hu, F.; Sun, C.; Yu, W. W.; Zhang, C.; Wang, X.; Zhang, Y.; Xiao, M. *Physical Review Letters* **2017**, *119*, 026401.

(11) Raino, G.; Nedelcu, G.; Protesescu, L.; Bodnarchuk, M. I.; Kovalenko, M. V.; Mahrt, R. F.; Stoferle, T. *ACS Nano* **2016**, *10*, 2485–2490.

(12) Qiao, H.; Abel, K. A.; van Veggel, F. C. J. M.; Young, J. F. *Physical Review B* **2010**, *82*, 165435.

(13) Studenyak, I.; Kranjec, M.; Kurik, M. *International Journal of Optics and Applications* **2014**, *4*, 76–83.

(14) Guyot-Sionnest, P.; Lhuillier, E.; Liu, H. *The Journal of Chemical Physics* **2012**, *137*, 154704.

(15) Kang, J.; Wang, L.-W. *The Journal of Physical Chemistry Letters* **2017**, *8*, 489–493.

(16) Halperin, B. I.; Lax, M. *Physical Review* **1966**, *148*, 722–740.

(17) Yan, R.; Zhang, W.; Wu, W.; Dong, X.; Wang, Q.; Fan, J. *APL Materials* **2016**, *4*, 126101.

(18) Jean, J.; Mahony, T. S.; Bozyigit, D.; Sponseller, M.; Holovský, J.; Bawendi, M. G.; Bulovic, V. *ACS Energy Letters* **2017**, *2*, 2616–2624.

(19) Protesescu, L.; Yakunin, S.; Bodnarchuk, M. I.; Krieg, F.; Caputo, R.; Hendon, C. H.; Yang, R. X.; Walsh, A.; Kovalenko, M. V. *Nano Letters* **2015**, *15*, 3692–3696.

(20) Liu, A.; Bonato, L. G.; Sessa, F.; Almeida, D. B.; Isele, E.; Nagamine, G.; Zagonel, L. F.; Nogueira, A. F.; Padilha, L. A.; Cundiff, S. T. *arXiv e-prints* **2019**, arXiv:1908.04881, arXiv:1908.04881.

APPENDIX E

Nitrogen-Vacancy Centers in Diamond

In this Appendix, we present results on nitrogen-vacancy centers in diamond. Vacancy centers in diamond [1, 2] have attracted sustained interest due to their exceptional optical properties. In particular, nitrogen-vacancy (NV) centers [3], the most well-studied of all defects in diamond, has found a variety of potential applications such as nanoscale sensors [4], solid-state qubits [5], and single-photon emitters [6].

However, an obstacle to practical implementation of NV centers in devices is their non-zero electric dipole moment that leads to spectral instability and linewidth broadening [7]. Other defects with inversion symmetry, most notably silicon-vacancy (SiV) centers, have proven less sensitive to their environment but possess their own disadvantages such as low internal quantum efficiencies (i.e. up to around 10% for SiV centers [8] compared to over 70% for NV centers [9]). There has thus been much recent effort towards engineering environmentally insensitive NV centers [10, 11], but doing so systematically and rationally will require a greater understanding of the fundamental interactions between NV centers and their environment.

Specifically, the dynamics of NV centers at both ultrafast timescales ($\leq$ ps) and low temperatures remains largely unexplored. In this regime, the physical processes

that lead to environmental perturbations of NV centers may be characterized by observing broadening of their optical transition linewidth. We further desire their *ensemble-averaged* properties, which inform us about the underlying physics without being biased by single exceptional centers. Unfortunately, the homogeneous properties of NV centers are obscured in ensemble measurements by inhomogeneous broadening that arises from locally varying electric field and strain.

E.1 Sample

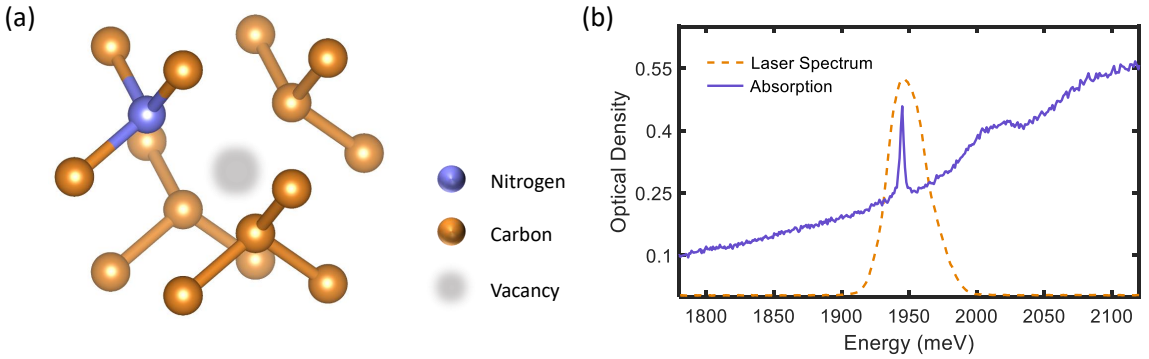

Figure E.1: (a) Diagram of a nitrogen vacancy center in diamond. (b) Absorption spectrum of the studied sample at 20 K. A narrow zero-phonon line is observed at 1946 meV (637 nm) on top of a broad phonon sideband that extends to higher energies. The spectrum of our MDCS excitation pulses is shown by the dashed orange line.

The sample studied is type Ib bulk diamond with a high density of single-substitutional nitrogen defects. Vacancy centers were introduced by irradiation with 1 MeV electrons and subsequent annealing, resulting in an ambient charged vacancy center (NV^-) density of 1-2 ppm. The atomic structure of such a center is shown in Fig. E.1a, which consists of a vacancy point-defect and an adjacent nitrogen substitution. This gives rise to a cryogenic absorption spectrum as shown in Fig. E.1b, consisting of a narrow zero-phonon line (ZPL) and an adjacent phonon sideband. We center our excitation laser spectrum on the ZPL as shown, and our narrow pulse bandwidth (compared to the known discrete vibrational modes [12, 13]) means that we predominantly mea-

sure the ZPL resonance of NV^- without other phonon-assisted transitions. The ZPL center energy is known to shift with temperature [14, 15] due to lattice interactions [16], but is relatively stationary in our measurements performed below 150 K. NV centers in their neutral charge state (NV^0) have a higher energy transition energy of 2156 meV (575 nm) and are not excited in our experiment.

E.2 Thermal Dephasing

One-quantum spectra at temperatures 15 K and 120 K are shown in Fig. E.2a and E.2b. The vertical $\hbar\omega_\tau$ is opposite in sign to the horizontal $\hbar\omega_t$ axis due to inverse phase-evolution during delays τ and t. Strong inhomogeneous broadening of the ZPL transition manifests as peak elongation along the diagonal ($|\hbar\omega_\tau| = |\hbar\omega_t|$) direction [17], while lineshapes in the orthogonal cross-diagonal direction reflect homogeneous broadening. However, homogeneous ($\gamma = 1/T_2$) and inhomogeneous (standard deviation σ of a Gaussian transition frequency distribution) broadening are completely separated in each direction only for systems dominated by inhomogeneous broadening ($\sigma \gg \gamma$). To extract γ and σ in the presence of moderate inhomogeneous broadening, as in NV centers, lineshapes in the diagonal and cross-diagonal directions must be simultaneously fit [17]. The experimental and fitted cross-diagonal lineshapes for each temperature are shown in Fig. E.2c and E.2d, with the resultant fitted one-quantum spectra plotted inset.

The temperature dependence of γ is plotted in Fig. E.2e, where the observed exponential increase in dephasing rate γ with temperature is characteristic of pure dephasing due to elastic interactions with discrete phonons. The thermal dephasing may be modeled by a linear dependence on the phonon mode occupation [18]:

$$\gamma(T_s) = \gamma_0 + \frac{\gamma^*}{e^{E_{ph}/k_B T_s} - 1} \tag{E.1}$$

where γ_0 is the intrinsic zero-temperature dephasing rate, γ^* is the thermal dephasing amplitude, T_s is the sample temperature, and E_{ph} is the phonon energy of the optical phonon responsible. A least-squares fit to the data is plotted as a solid line in Fig. E.2e, with fitted parameters $\gamma_0 = 5.94$ GHz, $\gamma^* = 1255$ GHz, and $E_{ph} = 34.4$ meV.

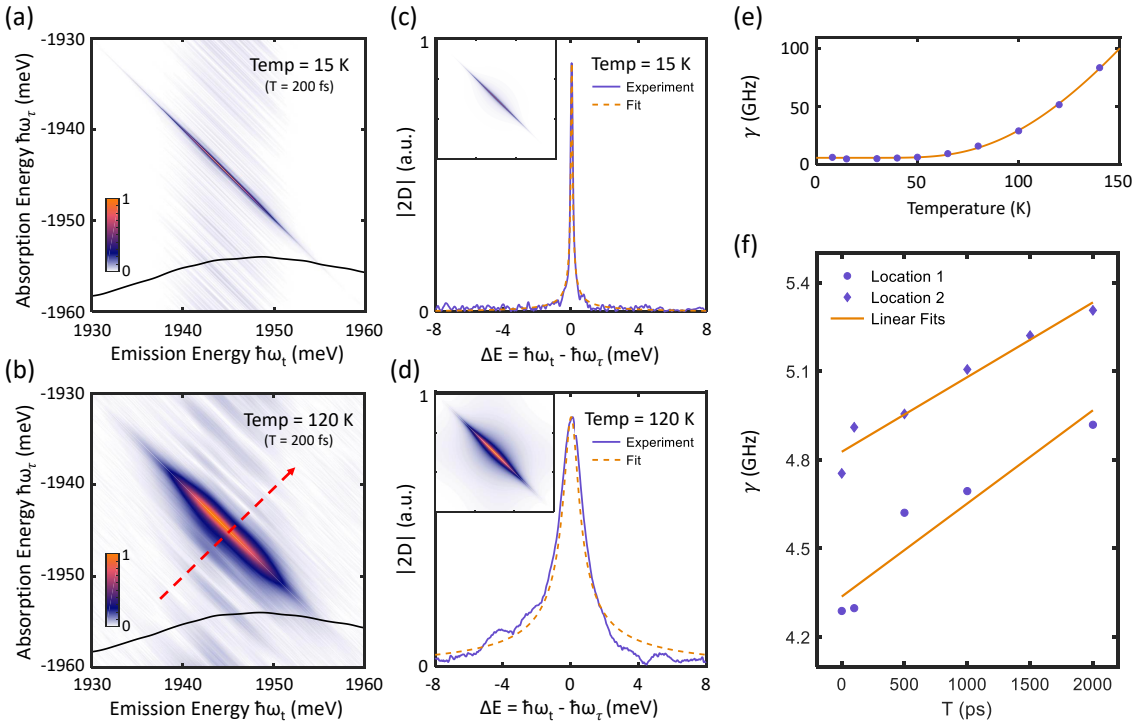

Figure E.2: One-quantum spectra taken at $T = 200$ fs and temperatures (a) 15 K and (b) 120 K. The solid black line indicates the respective excitation laser spectrum at each temperature. Elongation along the diagonal direction reflects inhomogeneous broadening of the ZPL transition. (c-d) Experimental and fitted cross-diagonal lineshapes are plotted at each temperature, with the resultant fitted one-quantum spectra inset. The slice positions at $|\hbar\omega_\tau| = |\hbar\omega_t| = 1945$ meV are indicated by the dashed red arrow in (b). (e) Fitted values of γ at temperatures increasing from 6 K to 140 K. The exponential increase in γ is fitted to a localized phonon dephasing model and plotted as the solid orange curve. (f) Fitted values of γ, taken at two different sample locations and 10 K, as a function of waiting time T. A monotonic increase in linewidth is observed as T increases from 1 ps to 2 ns, which is fitted as shown to linear spectral diffusion rates of 0.32 MHz/ps and 0.25 MHz/ps at each location.

It is known that the presence of an NV center modifies the vibrational spectrum of bulk diamond by introducing localized vibrational modes [19], whose vibrational amplitude decreases exponentially away from the center. In addition, these localized

modes may hybridize with various vibrational modes of the bulk diamond lattice and give rise to so-called quasi-localized vibrations [20] that are known to modify electronic dynamics [12]. The vibrational mode that matches the activation energy 34.4 meV most closely is a quasi-localized mode of (calculated) measured energy (31.62) 32.11 meV [12, 20–22], which involves vibrations of carbon atoms almost exclusively.

E.3 Ultrafast Spectral Diffusion

MDCS also enables the powerful capability to probe ultrafast spectral diffusion. While pulses A and C probe absorption and emission dynamics of the sample, the second pulse may be thought to induce a population state whose energy will vary in time. As the waiting time T between pulses B and C increases, absorption and emission energies of a resonance become less correlated and broadening in the cross-diagonal direction occurs. For systems with strong spectral diffusion, simultaneous broadening and distortion of the cross-diagonal lineshape occurs which allows extraction of the frequency-frequency correlation function [23] that quantifies the resonance energy fluctuations. However, we find that broadening of NV center lineshapes is too weak (within our experimental T delay limit) to perform such an analysis. We therefore plot a dependence of γ on waiting time T in Fig. E.2f, which provides an effective measure of spectral diffusion at ultrafast timescales. From measurements taken at two different locations on our sample, as T is increased from 1 ps to 2 ns the fitted effective dephasing rate γ increases at 0.32 MHz/ps and 0.25 MHz/ps. In a previous photon correlation study of NV centers in nanodiamonds [24] ultrafast spectral diffusion was found to occur only with simultaneous 532 nm excitation, which implicated impurity photo-ionization and subsequent charge trapping as the underlying mechanism. Our measurements of spectral diffusion, which involve only resonant excitation of the ZPL, indicate that spectral diffusion of NV centers in bulk diamond may occur

due to other mechanisms such as reorganization of the surrounding diamond lattice following optical excitation.

E.4 Picosecond-Timescale Population Relaxation

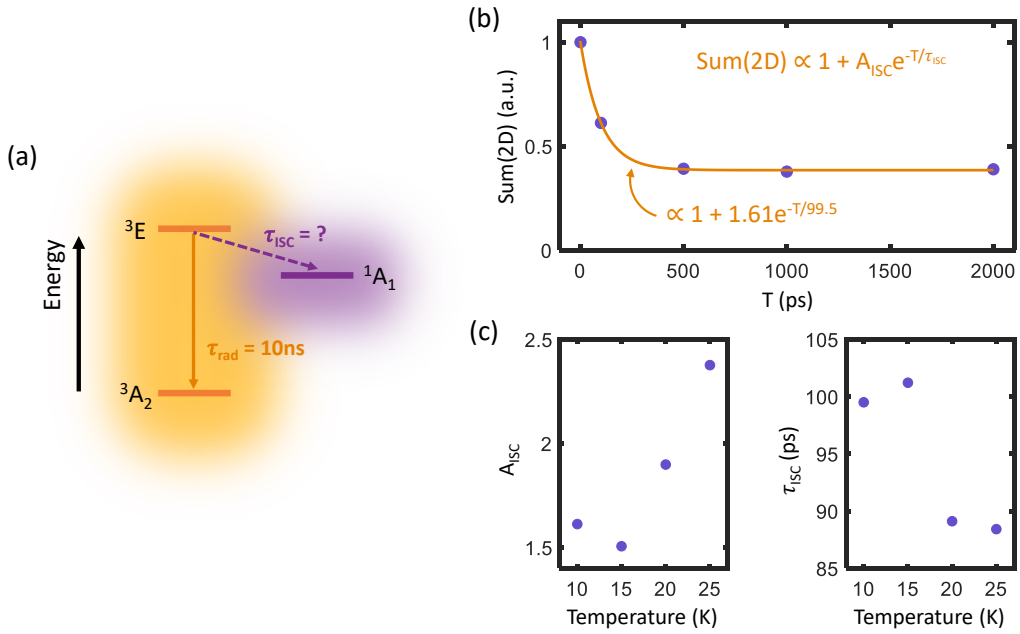

Figure E.3: (a) Simplified electronic level diagram consisting of the ground and excited states spin triplet manifolds ^{3}A$_2$ and ^{3}E respectively as well as the spin singlet shelving state ^{1}A$_1$. (b) Dependence of the integrated FWM signal on population time T at 10 K, which exhibits a fast exponential decrease due to the intersystem crossing. (c) Dependences of the branching ratio A_{ISC} and intersystem crossing time τ_{ISC} as a function of temperature.

We now examine the waiting time dependence of the total integrated FWM signal, which measures ultrafast population relaxation dynamics. A simplified electronic level diagram of NV centers is shown in Fig. E.3a, consisting of the ground and excited spin triplet manifolds ^{3}A$_2$ and ^{3}E respectively and the spin singlet shelving state ^{1}A$_1$. Upon optical excitation into ^{3}E, an electron may relax either radiatively into ^{3}A$_2$ by emitting 637 nm luminescence or non-radiatively via intersystem crossing (ISC) into ^{1}A$_1$. While the radiative recombination time of the optical ^{3}E to ^{3}A$_2$ transition is known to be 10 ns [25, 26], the timescale of the ISC has been known to

involve sub-nanosecond dynamics [27]. However, the ISC has only been investigated via time-resolved fluorescence measurements that are only sensitive to dynamics on the nanosecond timescale [28] and the branching ratio between the two relaxation pathways, crucial information for the spin-polarization cycle, has remained unknown. To measure the population relaxation dynamics on the sub-nanosecond timescale, the T dependence of the integrated FWM signal at 10 K is plotted in Fig. E.3b, which reveals a fast exponential decay that directly reflects the ISC relaxation time. We thus fit the measured T dependence to a decaying exponential and include an offset that corresponds to the 10 ns radiative relaxation timescale that is beyond our experimental T delay limit (equation shown in Fig. E.3b). For the T dependence at 10 K, the fitted branching ratio and ISC relaxation time are $A_{\mathrm{ISC}} = 1.61$ and $\tau_{\mathrm{ISC}} = 99.5$ ps respectively. We then repeated the same measurements at temperatures up to 25 K, and plot the fitted values of A_{ISC} and τ_{ISC} in Fig. E.3c. A marked increase in branching ratio with temperature is apparent which indicates, from the low Boltzmann energies in this temperature range, that the intersystem crossing arises from coupling to low-energy acoustic vibrational modes.

E.5 Temperature-Dependent Level Shifts

Curiously, as shown in Fig. E.4a the fitted inhomogeneous linewidth σ shrinks as temperature increases to 50 K before increasing monotonically afterwards. To examine this behavior more closely the diagonal slices are plotted in Fig. E.4b as a function of temperature. As indicated by the dashed arrows, increasing temperature results in the formation of two distinct lobes in the diagonal slice lineshape due to two families of NV centers that possess different temperature-shifts of the optical resonance. We tentatively propose that these two families physically originate from the four different orientations NV centers adopt in their diamond host lattice. Temperature-dependent anisotropic strain would shift the energy levels of different orientations in different

directions, which has recently been demonstrated in SiV centers [29]. We modeled this system as two independent Gaussian distributions with temperature-dependent parameters, which reproduced the data well (shown inset in Fig. E.4b). An absence of sidebands in the one-quantum spectra also indicates that the two families observed are not coherently coupled in any significant way.

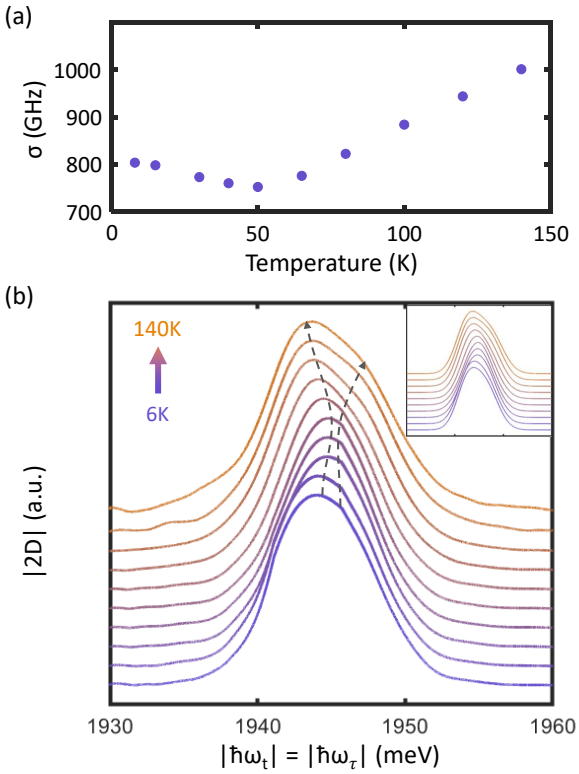

Figure E.4: (a) Fitted values of σ at temperatures increasing from 6 K to 140 K. (b) Respective diagonal slices at the temperatures in (a). Fits to a two-Gaussian model are shown inset. The energy shifts of the two fitted Gaussians are indicated by the dashed arrows in the main plot. The fitted two-Gaussian lineshapes are plotted inset.

We note that this energy splitting between two families has not been measured in single NV center studies due to spectral diffusion and would also be obscured in ensemble absorption and luminescence measurements, since the homogeneous linewidth is similar to the splitting energy. However, because homogeneous and inhomogeneous broadening are largely decoupled in a one-quantum spectrum along their respective orthogonal directions, the diagonal lineshape directly reflects the resonance frequency

distribution and reveals the temperature-dependent splitting.

References

(1) Aharonovich, I.; Neu, E. *Advanced Optical Materials* **2014**, *2*, 911–928.

(2) Schröder, T.; Mouradian, S. L.; Zheng, J.; Trusheim, M. E.; Walsh, M.; Chen, E. H.; Li, L.; Bayn, I.; Englund, D. *Journal of the Optical Society of America B* **2016**, *33*, B65–B83.

(3) Doherty, M. W.; Manson, N. B.; Delaney, P.; Jelezko, F.; Wrachtrup, J.; Hollenberg, L. C. L. *Physics Reports* **2013**, *528*, 1–45.

(4) Schirhagl, R.; Chang, K.; Loretz, M.; Degen, C. L. *Annual Review of Physical Chemistry* **2014**, *65*, 83–105.

(5) Dobrovitski, V. V.; Fuchs, G. D.; Falk, A. L.; Santori, C.; Awschalom, D. D. *Annual Review of Condensed Matter Physics* **2013**, *4*, 23–50.

(6) Aharonovich, I.; Englund, D.; Toth, M. *Nature Photonics* **2016**, *10*, Review Article.

(7) Acosta, V. M.; Santori, C.; Faraon, A.; Huang, Z.; Fu, K.-M. C.; Stacey, A.; Simpson, D. A.; Ganesan, K.; Tomljenovic-Hanic, S.; Greentree, A. D.; Prawer, S.; Beausoleil, R. G. *Physical Review Letters* **2012**, *108*, 206401.

(8) Neu, E.; Agio, M.; Becher, C. *Optics Express* **2012**, *20*, 19956–19971.

(9) Radko, I. P.; Boll, M.; Israelsen, N. M.; Raatz, N.; Meijer, J.; Jelezko, F.; Andersen, U. L.; Huck, A. *Optics Express* **2016**, *24*, 27715–27725.

(10) Chu, Y. et al. *Nano Letters* **2014**, *14*, 1982–1986.

(11) Van Dam, S. B.; Walsh, M.; Degen, M. J.; Bersin, E.; Mouradian, S. L.; Galiullin, A.; Ruf, M.; IJspeert, M.; Taminiau, T. H.; Hanson, R.; Englund, D. R. *Physical Review B* **2019**, *99*, 161203.

(12) Huxter, V. M.; Oliver, T. A. A.; Budker, D.; Fleming, G. R. *Nature Physics* **2013**, *9*, Article.

(13) Ulbricht, R.; Dong, S.; Gali, A.; Meng, S.; Loh, Z.-H. *Physical Review B* **2018**, *97*, 220302.

(14) Davies, G. **1974**, *7*, 3797–3809.

(15) Doherty, M. W.; Acosta, V. M.; Jarmola, A.; Barson, M. S. J.; Manson, N. B.; Budker, D.; Hollenberg, L. C. L. *Physical Review B* **2014**, *90*, 041201.

(16) Liu, A.; Bonato, L. G.; Sessa, F.; Almeida, D. B.; Isele, E.; Nagamine, G.; Zagonel, L. F.; Nogueira, A. F.; Padilha, L. A.; Cundiff, S. T. *arXiv e-prints* **2019**, arXiv:1908.04881, arXiv:1908.04881.

(17) Siemens, M. E.; Moody, G.; Li, H.; Bristow, A. D.; Cundiff, S. T. *Optics Express* **2010**, *18*, 17699–17708.

(18) Singh, R.; Autry, T. M.; Nardin, G.; Moody, G.; Li, H.; Pierz, K.; Bieler, M.; Cundiff, S. T. *Physical Review B* **2013**, *88*, 045304.

(19) Gali, A.; Simon, T.; Lowther, J. E. **2011**, *13*, 025016.

(20) Zhang, J.; Wang, C.-Z.; Zhu, Z. Z.; Dobrovitski, V. V. *Physical Review B* **2011**, *84*, 035211.

(21) Abtew, T. A.; Sun, Y. Y.; Shih, B.-C.; Dev, P.; Zhang, S. B.; Zhang, P. *Physical Review Letters* **2011**, *107*, 146403.

(22) Ulbricht, R.; Dong, S.; Chang, I.-Y.; Mariserla, B. M. K.; Dani, K. M.; Hyeon-Deuk, K.; Loh, Z.-H. *Nature Communications* **2016**, *7*, Article.

(23) Singh, R.; Moody, G.; Siemens, M. E.; Li, H.; Cundiff, S. T. *Journal of the Optical Society of America B* **2016**, *33*, C137–C143.

(24) Wolters, J.; Sadzak, N.; Schell, A. W.; Schröder, T.; Benson, O. *Physical Review Letters* **2013**, *110*, 027401.

(25) Collins, A. T.; Thomaz, M. F.; Jorge, M. I. B. **1983**, *16*, 2177–2181.

(26) Ulbricht, R.; Loh, Z.-H. *Physical Review B* **2018**, *98*, 094309.

(27) Acosta, V. M.; Jarmola, A.; Bauch, E.; Budker, D. *Physical Review B* **2010**, *82*, 201202.

(28) Goldman, M. L.; Sipahigil, A.; Doherty, M. W.; Yao, N. Y.; Bennett, S. D.; Markham, M.; Twitchen, D. J.; Manson, N. B.; Kubanek, A.; Lukin, M. D. *Physical Review Letters* **2015**, *114*, 145502.

(29) Meesala, S. et al. *Physical Review B* **2018**, *97*, 205444.

APPENDIX F

Sample Preparation

F.1 Resuspension of Nanocrystals

We receive samples of nanocrystals suspended in various solvents such as toluene or hexane. However, for low-temperature measurements we resuspend the nanocrystals in heptamethylnonane (Sigma Aldrich 128511), a branched alkane that forms a transparent glass at cryogenic temperatures.

1. Measure mass of separate vial. Pipette 1-2 mL of the sample into vial.
2. Blow nitrogen gas over sample to evaporate original solvent.
3. Measure vial mass again to calculate mass of nanocrystals.
4. Pipette appropriate volume of heptamethylnonane into vial to reach desired optical density (typically 0.3 at 1S exciton peak).

F.2 Sample Holder

To study colloidal nanocrystals at cryogenic temperatures, we hold each colloidal suspension in a custom copper sample holder that is mounted to a cold-finger cryostat

(Janis ST-100). The sample holder is composed of an inner and outer component.

A schematic of the inner component is shown in Fig. F.1, which is composed of two outer copper rings that clamp together two wedged sapphire discs (Meller Optics SCD2506-01B) spaced 0.5 mm apart.

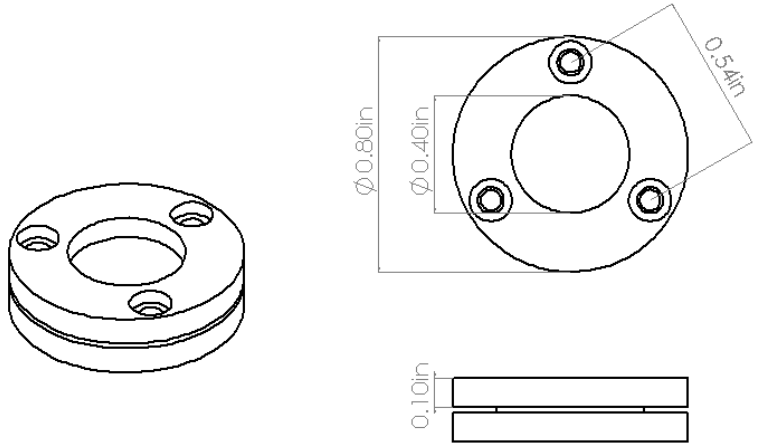

Figure F.1: Isometric (left) and projection (right) views of the inner component.

A schematic of the outer component is shown in Fig. F.2, which clamps the inner component in a cryostat mount.

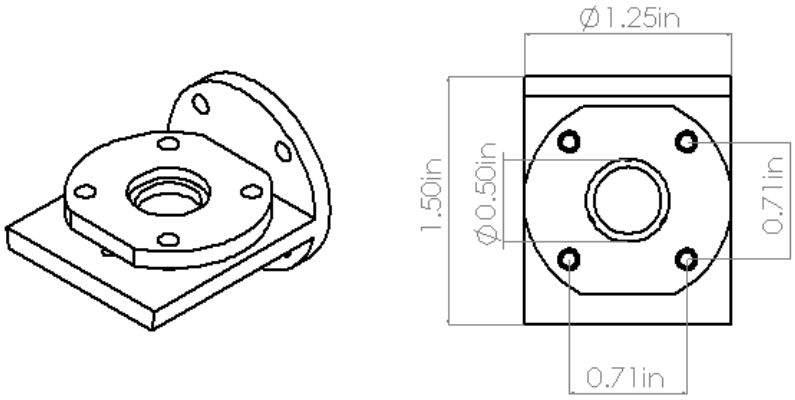

Figure F.2: Isometric (left) and front (right) views of the outer component.

F.3 Inner Component Loading Procedure

1. Agitate nanocrystals in vial by stirring in vortex mixer or sonicator.

2. If unloading sample: Unscrew inner component on kimwipes to absorb excess nanocrystals. Use polymer tweezers to remove kevlar ring and push on sides of sapphire disks to remove from copper. Clean copper with methanol and kimwipes. Remove indium rings from sapphire disks. To clean sapphire disks, add 2 drops of methanol on one side of disk. Put that side face down on lens tissue. Add 2 more drops on other side. Fold tissue on top and drag over with finger to clean both sides. If too dirty, use toluene.

3. Push indium rings (0.1" thickness) into copper holders.

4. Locate thick side of each sapphire disk. Align each disk to opposite sides of the marked holes on each copper ring such that when the sample is screwed together, the thick side of each sapphire disk aligns to each other. After aligning, push sapphire disks into copper.

5. Using tweezers, close them and dip into cement. Put cement on edge of copper and sapphire. Do at 3 points opposite each hole.

6. Apply rubber cement to kevlar ring with foam q-tip until shiny. Put ring in the middle of the sapphire disk of the bottom half.

7. Pipette 45 μL of nanocrystals into kevlar ring. With other half ready with screws inside, attach sandwich using alignment tool.

F.4 Outer Component Mounting Procedure

1. Apply N-grease to inner sides of the cryostat mount until shiny.

2. Push indium rings (0.11-0.12" thickness) into inner sides.

3. Clamp the inner component by tightening screws gradually in succession.

4. Apply N-grease to temperature sensor until shiny and clamp onto long screw.